Theses and Dissertations

August 2015

Integrated Li-Ion Ultracapacitor with Lead Acid Battery for Vehicular Start-Stop

Emad Manla

University of Wisconsin-Milwaukee

INTEGRATED LI-ION ULTRACAPACITOR WITH LEAD ACID BATTERY
FOR VEHICULAR START-STOP

by

Emad Manla

A Dissertation Submitted in

Partial Fulfillment of the

Requirements for the degree of

Doctor of Philosophy

in Engineering

at

The University of Wisconsin-Milwaukee

August 2015

ABSTRACT
INTEGRATED LI-ION ULTRACAPACITOR WITH LEAD ACID BATTERY FOR
VEHICULAR START-STOP

by

Emad Manla

The University of Wisconsin-Milwaukee, 2015
Under the Supervision of Professor Dr. Adel Nasiri

Advancements in automobile manufacturing aim at improving the driving experience at

every level possible. One improvement aspect is increasing gas efficiency via

hybridization, which can be achieved by introducing a feature called start-stop. This

feature automatically switches the internal combustion engine off when it idles and

switches it back on when it is time to resume driving. This application has been proven to

reduce the amount of gas consumption and emission of greenhouse effect gases in the

atmosphere. However, the repeated cranking of the engine puts a large amount of stress

on the lead acid battery required to perform the cranking, which effectively reduces its

life span. This dissertation presents a hybrid energy storage system assembled from a lead

acid battery and an ultracapacitor module connected in parallel. The Li-ion ultracapacitor

was tested and modeled to predict its behavior when connected in a system requiring

pulsed power such as the one proposed. Both test and simulation results show that the

proposed hybrid design significantly reduces the cranking loading and stress on the

battery. The ultracapacitor module can take the majority of the cranking current,

effectively reducing the stress on the battery. The amount of cranking current provided by

the ultracapacitor can be easily controlled via controlling the resistance of the cable

connected directly between the ultracapacitor module and the car circuitry.

TABLE OF CONTENTS

LIST OF FIGURES

LIST OF TABLES

ACKNOWLEDGEMENTS

I would like to thank my doctoral thesis supervisor Professor Dr. Adel Nasiri for the endless support, guidance, advising, and understanding without which this dissertation would not have seen the light. I would like to offer my gratefulness to my dissertation committee members: Dr. David Yu, Dr. Chiu Tai Law, Dr. Dan Ionel, and Dr. Sam Helwany for all the guidance and support with which they have provided me during the years I spent as a graduate student at the University of Wisconsin- Milwaukee. Their advice and guidance made my unforgettable journey as a graduate student such a smooth and rich experience. I appreciate the companionship of my friends as well as colleagues at the Laboratory of Power Electronics and Electric Drives at the University of Wisconsin Milwaukee. I thank Jeff Myron from JSR Micro for providing samples of the latest Li-ion ultracapacitors used in my experimental setup and answers to my questions about their operation and modeling. I much appreciate the funds provided by JCI, which allowed this research to happen. I am grateful to Bill Patterson's efforts to provide the necessary space inside the USR building where the research took place. I also thank Betty Warras for her extreme friendliness and for trying her best to facilitate any paper work or administrative steps needed for me to complete my degree. Finally, I want to offer my most sincere thanks to my parents for everything they did for me throughout their lives, for all the time I spent away from them to get my degree completed, and for their endless love and understanding.

Chapter 1. Introduction and Literature review

1.1 Problem statement

Due to the ever rising worldwide demand for oil and the growing concerns about polluting the environment caused by burning fossil fuels to harvest power, new trends have surfaced to reduce the reliance on oil derivatives. Renewable energy sources such as solar and wind power are among the hottest areas of research nowadays. In fact, the US department of Energy (DOE) released a report in 2008 examining some of the impacts, challenges, and costs of large-scale national wind power harvesting for the production of electricity from wind and anticipating 20% electrical power production by 2030 [1].

While renewable energy sources offer a significant portion of power, one should not overlook the benefits of marginal gains in power efficiency obtained from conventional systems running on fossil fuels. Such systems include internal combustion engines found in the majority of vehicles nowadays. One simple way to improve the efficiency of combustion engines would be switching it off when idling for a relatively long periods of time while waiting for a red traffic light or in severe traffic jams, and then switching it back on when it is time to move forward. This idea is not new. It, in fact, saw light back in the mid 1970's. A study published in 1974 by Toyota found that one can improve fuel economy by 10% in Tokyo traffic [2].

The start-stop technology was fully implemented in Fiat Regata cars in the early 1980's [11]. The start stop version of Regata 70 showed improvement in fuel economy compared with the regular Regata 70 version. The start stop version consumes 5.2 liters/100 km at 90km/hr, 7 liters/100 km at 120 km/hr, 7.4 liters/100 km for the urban

cycle and 6.7 liters/100 km for the combined cycle. Fiat's start-stop technology came out in its full production on the car of the year award winning Fiat 500 back in 2008 saving up to 5 liters of gas per 100km during in-city driving [11].

In September 1999, Honda Motors introduced the compact INSIGHT personal hybrid car "combining superior driving pleasure with world-leading environment-friendliness, this new model offers the world's lowest fuel consumption for a gasoline-powered vehicle attaining gas mileage of 35 km/liter [13]." This model was equipped with an automatic idle stop system, that switches the engine off whenever the car come to a complete halt reducing gas consumption and exhaust emissions [13]. Figure 1.1 shows the Honda hybrid car released in the Japanese Market in 1999.

Figure 1.1. INSIGHT hybrid car in 1999 [13].

Italian car manufacturer Alfa Romeo fitted its Alfa Romeo MiTo car series with the start-stop technology starting September 2009 [12]. Around the same time many European car manufacturers were integrating their cars with this technology. For instance, Volvo introduced it in 2009 on its DRIVe models [14], Citroën introduced it in 2006, BMW started to include it in many of its cars and MINI line in 2008, and Renault introduced it in its European models in 2010. Asian car manufacturers such as Kia,

Hyundai, Mazda, Mahindra & Mahindra, and Tata Motors also integrated their products with the start-stop technology starting mid 2000's.

While this engine start-stop idea sounds costless and simple enough to apply, it has two main problems: first, it has a hard time being applied manually in that drivers often find it tedious to keep their fingers on the car switch especially when driving for a long time in jammed areas. Also, people tend to forget about the gas savings attained from this technique shortly after being convinced of its benefits. Another issue raised when frequently switching the engine off and then back on is that it puts an enormous amount of pressure on the car battery especially when the switching is done repetitively within a short period of time without giving the battery enough time to relax and recharge to the nominal value of its terminal voltage. Other problems may arise from this technique and will be addressed later in this study.

Luckily, the first problem has a reliable solution, drivers do not have to apply the start-stop technique manually because a control system can be and has been designed to sense engine idling times and switch the engine off. The same control system can sense when it is time to move and then switch the engine back on. The early systems designed to automatically apply the start-stop technology were not as smooth as one would hope; often, disconcerting motion was experienced leading to the manual shutting off of the start-stop control system and driving without it. Research and development in control systems have led to much reliable and smoother systems designed by many car manufacturers.

What seems to be the major problem in start-stop technology is the stress experienced by the car battery. The car starter, normally a compound DC motor, draws a huge amount of current during the cranking up of the combustion engine. The current drawn from the car battery can reach a value of 500 A in smaller cars and a 1000 A in larger vehicles like trucks and city buses. Although this value of current is drawn during a few milliseconds, the battery voltage plummets to a dangerous value that can lead to structural corrosion when done repetitively leading to the shortening of the battery life span. Figure 1.2 shows a combustion engine piston cross sectional view along with the starter motor [3].
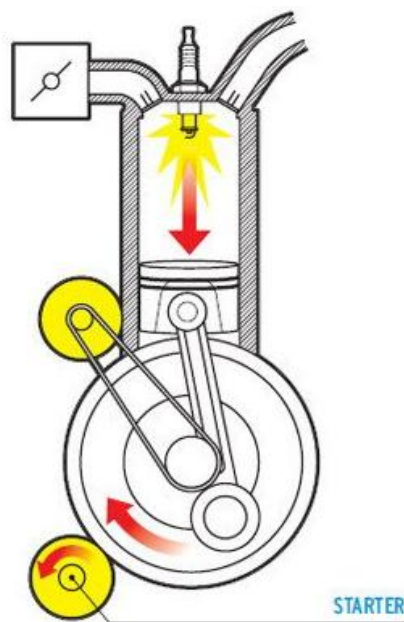
Figure 1.2. Combustion engine starter motor [3].

Car batteries experience this severe voltage sag mainly due to their modest power density compared with some other types of energy storage devices. One way to improve the power capabilities of batteries is to oversize them. Reference 7 presents a study done in year 2000 in which a super-capacitor is combined with a battery pack to improve response to power peaks. It states that this hybrid ESS "increases power peak level by

above 40%" overcoming the need for oversized battery pack to be able to handle power peak demands [7]. Super-capacitors, also known as ultracapacitors, happen to have a much larger power density than lead acid batteries. However, they have a much lower energy density. That explains their ability to handle high amounts of electric current but not for a long period of time as they will run out of energy. Batteries, on the other hand, provide a steady amount of electric current for a longer period of time but won't be able to handle spikes of electric current without inflicting physical damage to their composition. Therefore, the solution to this start-stop problem would be replacing the car battery, which is normally lead acid, by another electrochemical energy storage device type that combines high energy density with high power density. Unfortunately, no such device exists in the market; and hence, one feasible solution would be combining an ultracapacitor with a lead acid battery in a module in order to handle both modes of operation, i.e. cranking and steady state.

Ultracapacitors differ from conventional capacitors mainly in terms of the value of capacitance. The Farad is a huge unit as it is, and it is impossible to make a reasonably sized double-plate conventional capacitor having a capacitance of one Farad, or even a fraction of a Farad, that can be used in a realistic circuit. This makes conventional capacitors inferior to batteries as mass energy storage devices. Ultracapacitors nowadays are undergoing continuous manufacturing improvements to increase their capacitance leading to Energy storage devices that can compete with batteries in both power density and energy density. The structure of an ultracapacitor is similar to a conventional one. Namely, it is made up of two metallic or Carbon plates having opposite polarity charges and separated by a very thin dielectric material. What makes ultracapacitor large in

capacitance is the porosity of the plates holding the electric charges. Figure 1.3 explains the structure of ultracapacitors [17].
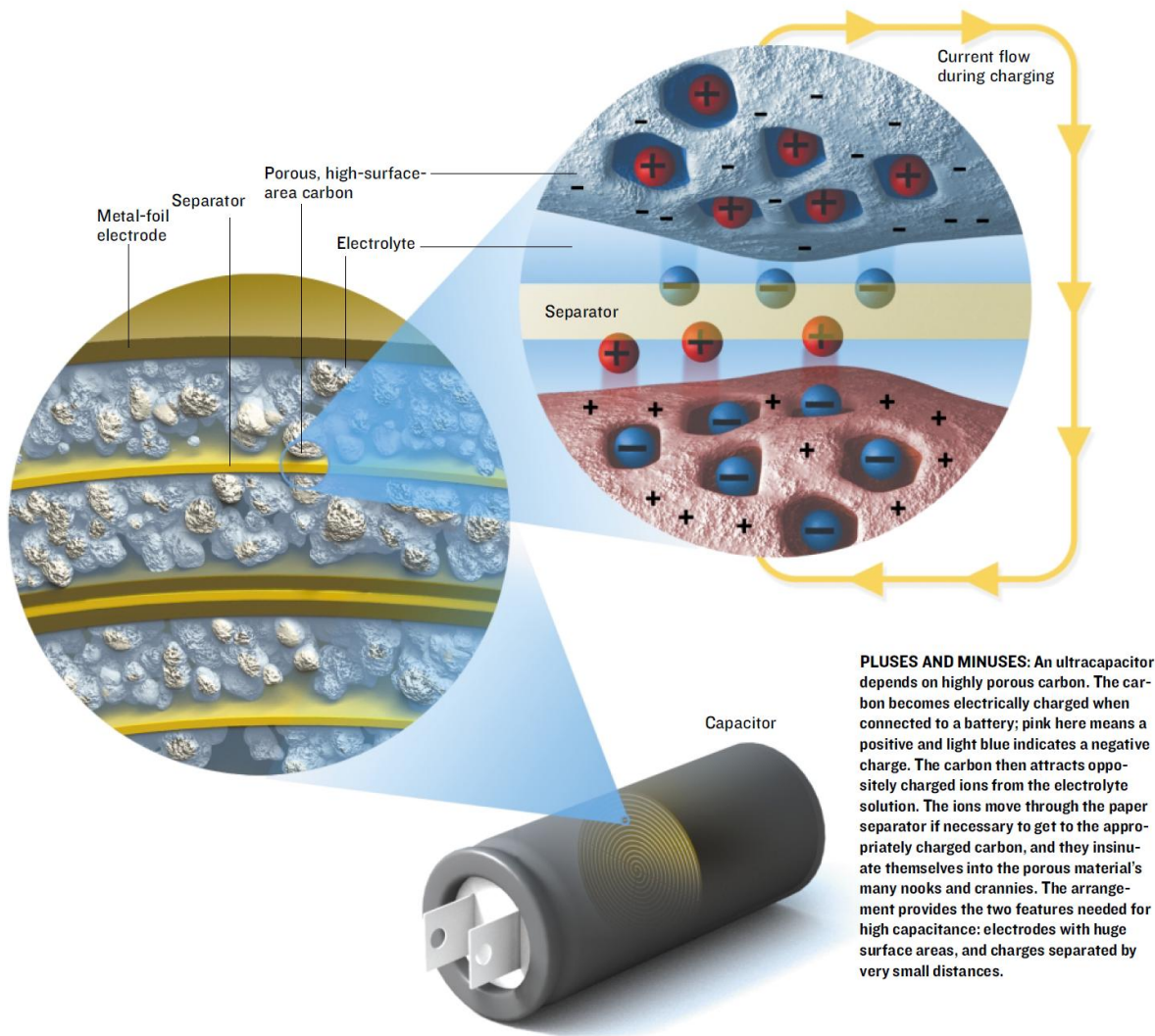
Figure 1.3. Structure of ultracapacitors [17].

Ultracapacitors come in various types, dimensions, chemical composition, and electrical properties. The newest type of ultracapacitors available today is manufactured based on lithium-ion technology. In addition to the high power density required for the start-stop application in automobiles, this type has proven to have higher energy density than conventional super-capacitors, low internal resistance, high energy and Columbic efficiencies, and long cycle life. Combining an ultracapacitor of this type with a lead acid

battery would be an excellent solution for the start-stop technology. The ultracapacitor can have a major contribution to the brief spike in demanded power while cranking, whereas the lead acid battery can otherwise provide the steady state power demanded in normal mode of operation and recharge the ultracapacitor.

1.2 Previous work

1.2.1 Combining an ultracapacitor with a battery in a hybrid ESS

The work found in literature about an ESS combining an ultracapacitor with a battery is very interesting. The idea of combining an ultracapacitor with a vehicle battery to improve its lifetime goes back to the late 1980's and early 1990's. A paper published in 1990 states that "load leveling the main storage battery is a promising approach for reducing the design power requirements for the battery and increasing battery life. Significantly increased vehicle range should also result for batteries, which have been optimized for energy density at the lower peak power requirements made possible by load leveling. Consideration of the characteristics of ultracapacitors and bipolar lead-acid pulse batteries for the pulse power device indicates the device could be used, but the efficiency of the system would be greater by about 10% using the ultracapacitors [5]." This dissertation shows simulation results with power consumption improvement by 8.5% due to avoiding high impulse currents through the battery having a large internal resistance [5].

The next set of papers discussing the advantages of a hybrid ultracapacitor/battery ESS are published in the early 2000's after a break of over a decade. It seems that this topic regained some interest by scientists and researchers after the global increase in oil

prices resulting in people looking for alternatives to fossil fuels and encouraging techniques to increase fuel efficiency. An extensive study done in 2002 shows that adding a 23-F ultracapacitor bank in parallel with a typical Li-ion battery of 7.2 V and 1.35 A hr capacity can boost the peak power capacity by 5 times and reduce the power loss by 74%, while minimally impacting system volume and weight [8]. The authors of this paper derive all the necessary equations that back up their findings. They could analytically reach the conclusion that a "battery/ultracapacitor hybrid power source can supply a pulsed load with higher peak power, smaller internal losses, and greater discharge life of the battery than can the battery-powered system alone [8]."

Some studies also investigated the idea of incorporating ultracapacitors in EV's not only to supply high peak power demands at take-offs, but also to absorb high currents obtained from regenerative breaking. A paper published in 2002 discusses that idea and shows, using both simulation results and experimental results, that a better more efficient design can be achieved when combining batteries with ultracapacitors [9]. However, back in the early 2000's, the prices of ultracapacitors were too high for applications like this. Nowadays, prices of ultracapacitors have gone down while Energy density and capacitance have gone considerably up.

A paper published in 2003 discusses the combination of a battery bank with an ultracapacitor bank [6]. The combination of these two ESS banks was simulated and also built and partially tested. The battery bank is rated 336 V at 150 Ah while the ultracapacitor bank is rated 375 V with energy storage capability of 1.2 MJ. The combination of these two energy storage banks was done in direct shunt connection and through a DC/DC converter. The paper mentions that the DC/DC connection shows much

better results where the full power capability of the ultracapacitor bank was exploited reducing stress on the battery bank and reducing power loss across the battery relatively large internal resistance. Figure 1.4 shows both the capacitor and battery energy storage modules [6].

(a)   (b)
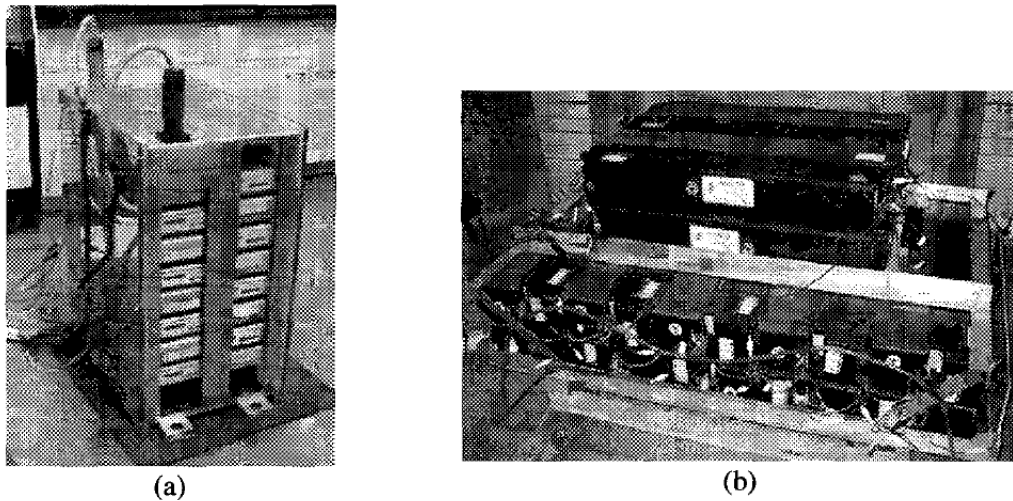
Figure 1.4. (a) Capacitor bank. (b) Battery bank [6].

In the direct shunt connection case, the simulation results show some improvement to the battery power profile having an ultracapacitor module that absorbs some of the load current. The load current is an exponentially increasing curve that saturates at 300 A. When looking at figure 1.5 that shows the current and voltage profiles of the hybrid ESS, one sees that the battery takes care of most of the current drawn by the load. The ultracapacitor module takes care of a portion of the load current, which does not exceed one third of the drawn current on average. This is definitely an improvement, but it does not utilize the full capability of the ultracapacitor module.
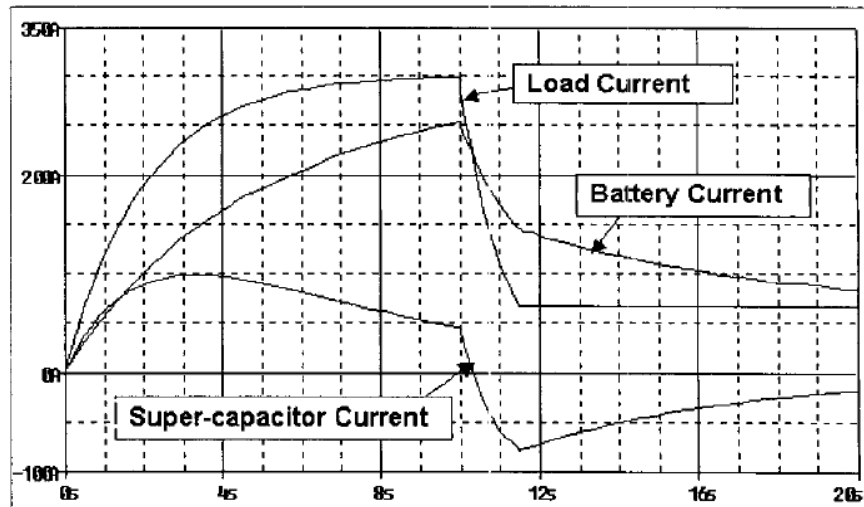
(a)
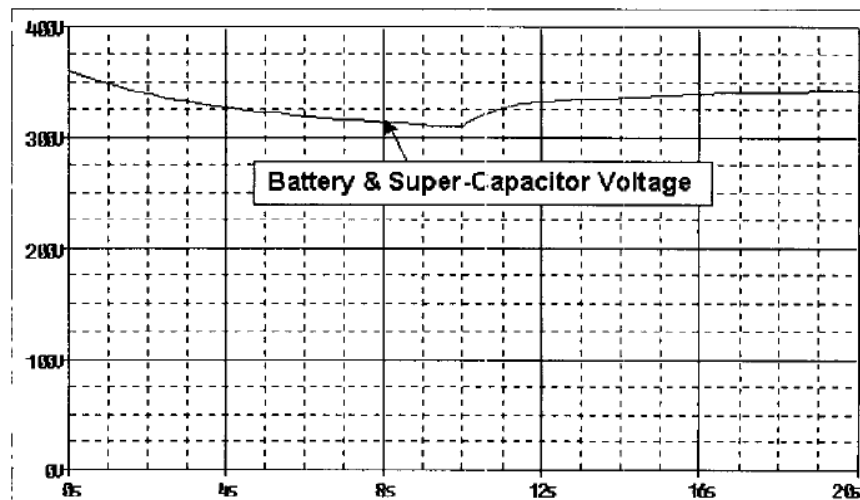
(b)

Figure 1.5. Simulation results for the direct shunt connection: (a) Load, battery, and ultracapacitor currents. (b) Module voltage [6].

When connecting the ultracapacitor module to the battery module through a buck/boost converter controlling the amount of current that the ultracapacitor module is responsible for, the simulation results shown in figure 1.6 clearly demonstrate a significant decrease in battery current and a drastic increase in ultracapacitor current. The load profile used here is the same as the one used in the direct shunt connection.

(a)

(b)
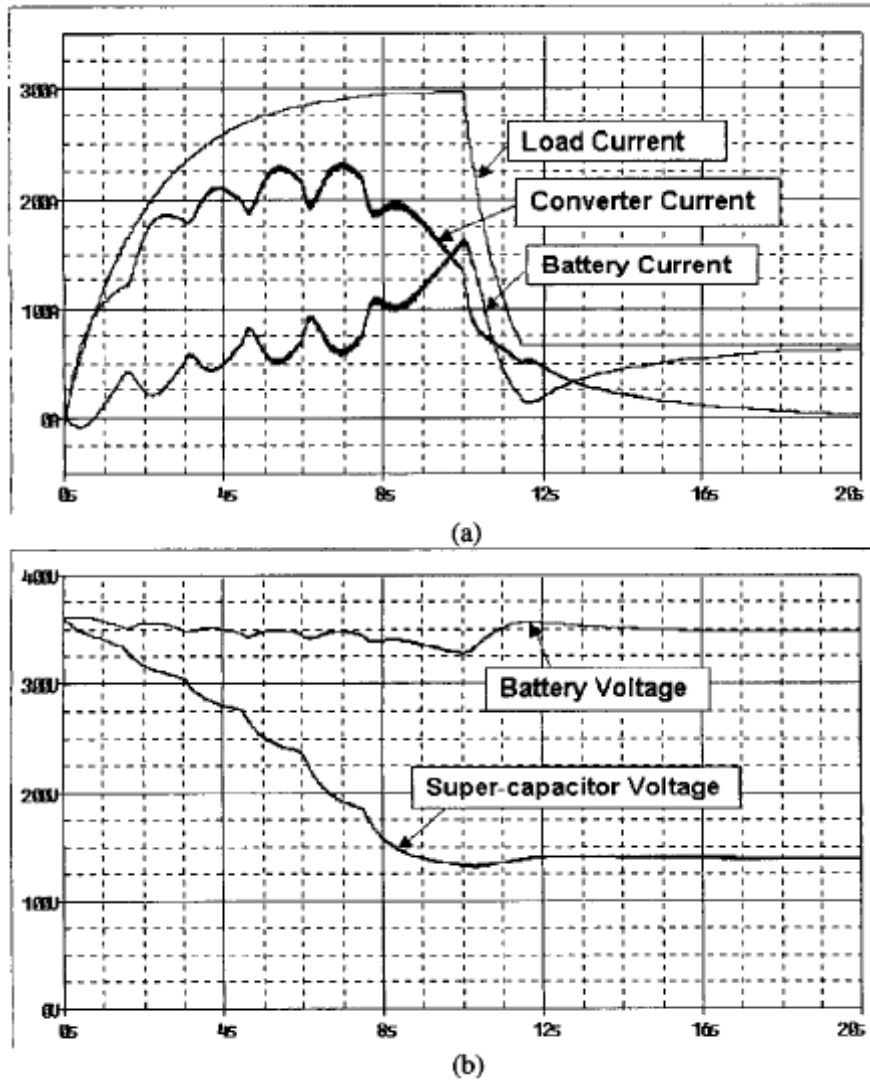
Figure 1.6. Simulation results for the connection through a DC/DC converter: (a) Load, battery, and ultracapacitor currents. (b) Ultracapacitor and Battery module voltage [6].

One can see the reduction in the amount of current drawn from the battery compared to the ultracapacitor module. It is also clear that the ultracapacitor module experiences much lower terminal voltage compared to the battery. This of course does not inflict any damage to the module designed to withstand low voltage values by nature. Battery terminal voltage stays considerably high effectively increasing its life span, which gets shorter when its terminal voltage plummets.

1.2.2 Control Systems for a hybrid battery/ultracapacitor ESS

Now that the idea of replacing a car battery by a hybrid ESS combining the battery with an ultracapacitor has been proven to offer a reliable, efficient solution to high peaks in power demand, the next set of papers show research done to investigate the possibilities and effectiveness of the control systems that manage the power profile shared by the battery and the ultracapacitor.

In a paper published in 2003, the extent to which the performance of a battery/ultracapacitor hybrid ESS was studied. "Two cells of Sony US18650 lithium-ion battery and two cells of Maxwell PC 100 super-capacitors are used" to construct the module. A DC/DC converter in series with the battery was simulated and then the module was built. Higher mass and power densities were achieved without drawing excessive battery current [10]. Simulation results perfectly matched experimental results [10]. Figure 1.7 shows the block diagram of the design.
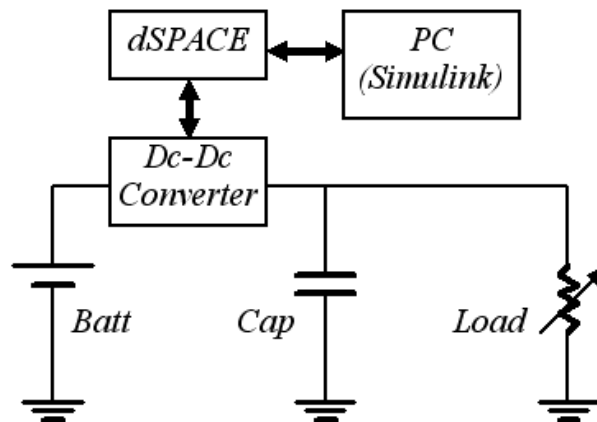
Figure 1.7. Block diagram for the hybrid ESS in the experimental setup [10].

As a continuation to a project conducted in the early 2000's and published in 2003 at the Pennsylvania Transportation Institute at Pennsylvania State University where

ultracapacitors were utilized along with batteries to make a hybrid ESS for mass-transit vehicles [15], a study was conducted on the controls of this hybrid ESS around the same time and it got published in 2004 in the Proceeding of the 2004 American Control Conference in Boston, Massachusetts. A system involving a boost converter connected to the ultracapacitor is mathematically studied. Also, tests were conducted to investigate the benefits of such a hybrid ESS. The control methods under consideration were also studied in the frequency domain. This paper also shows the distribution of the number of occurrences of current values demanded from the battery in the battery-alone system and in the hybrid ESS.
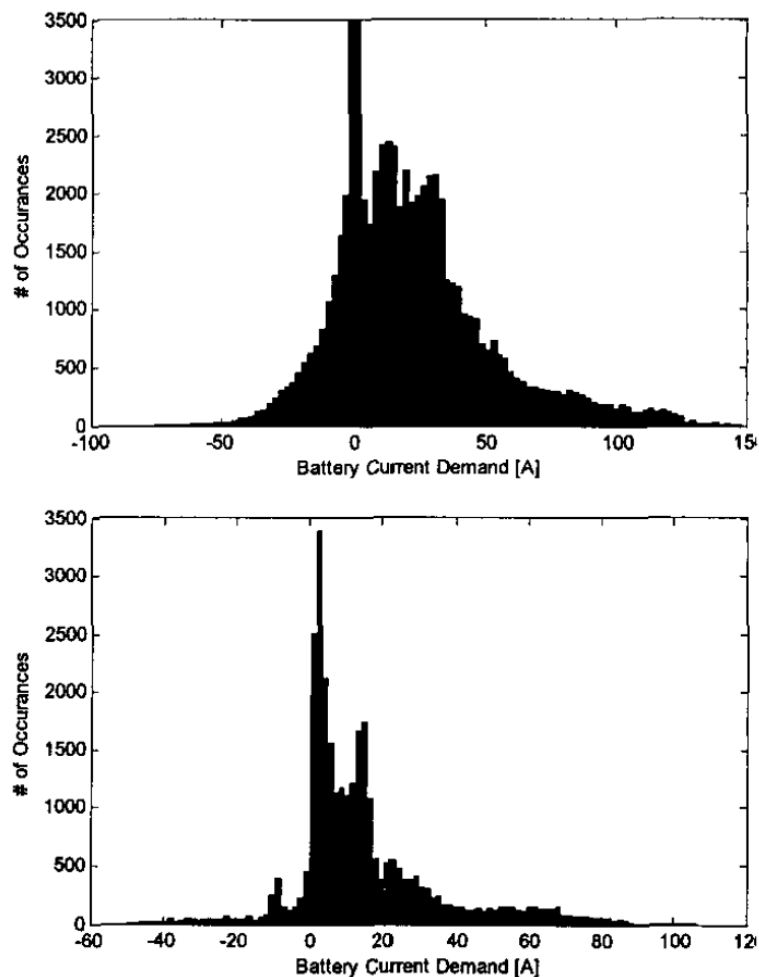
Figure 1.8. Battery current demand. Battery alone (upper). Hybrid ESS (lower) [15].

Figure 1.8 represents the histograms of the demanded battery currents for a hybrid vehicle in EV mode during the urban driving cycle in Manhattan. "The benefit of the peaking controller is evident by examining the histograms of the battery current demand both with and without the ultracapacitors in use, for the same driving cycle. It is evident that the ultracapacitors reduced the extremes in current demand in both acceleration and in regenerative braking. In acceleration, the peak current demanded from the battery changed from 140 amps without the ultracapacitors to 90 amps with the ultracapacitors. In regenerative braking, the activation of the ultracapacitors lowered peak battery charging current from 60 amps to 45 amps. More importantly, the volume of current (i.e. power transients) moved through the battery is seen to be greatly reduced over nearly all current levels. This is primarily due to the ultracapacitors ability to store regenerative energy and release it during acceleration. This benefit is most evident in stop-start driving such as the Manhattan cycle [16]."

A quantitative analysis of the power enhancement obtained from a DC/DC converter-based hybrid battery/ultracapacitor ESS is presented in [18] where a "hybrid built from two size 18650 lithium-ion cells and two 100-F ultracapacitors achieved a peak power of 32Wwhich is a three-times improvement in peak power compared to the passive hybrid power source (hybrid without a converter), and a seven times improvement as compared to the lithium-ion cells alone [18]." A block diagram showing the Hybrid system along with the control system is shown in figure 1.9.

Figure 1.9. Block diagram of hybrid ESS with controls [18].

The control system deployed for this prototype was built in Simulink using DSpace data acquisition and interface card. The control system built in Simulink is shown in figure 1.10. In this diagram "the controller has two input ports (In1 and In2) connected to two current sensors monitoring the load current and the power converter output current, respectively [18]." The monitored current signals are then fed to the PI controller, and the new calculated converter duty ratio from the PI controller is sent back to the power converter model through the output port [18].

Figure 1.10. PI control system for the hybrid ESS [18].

The advantage of this control system comes from the fact that "the operation of an active hybrid results in a much lower battery current with very small ripples, and

therefore a lower battery temperature, which are preferred by many applications for a longer battery lifetime. The discharge cycle time is reduced for the active hybrid due to an added converter loss and increased ultracapacitor loss. A compromise should be made between the power enhancement and the discharge cycle time in order to achieve optimized results depending upon applications. The design can be scaled to larger or smaller power capacities for various applications [18]."

Later papers discuss ways to improve the efficiency of control systems that govern the distribution of peak current demand between battery and ultracapacitor.

Recent conference and journal papers discuss the battery/ultracapacitor hybrid ESS mainly using simulations of such a system. For instance, a conference paper published in 2010 in the International Conference on Optoelectronics and Image Processing shows that whether a lead acid battery is connected with an ultracapacitor directly in a parallel configuration or through a DC/DC converter, the power in a hybrid city bus developed in China can be enhanced by a factor β [4]. This paper shows simulation results of both systems. The power-train is comprised of a diesel engine (with a rated power of 155 kW, a rated speed of 2500 rpm, and a maximum torque of 800 Nm at a speed range between 1200 and 1700 rpm) and an asynchronous AC motor with a rated output power of 55 kW and maximum power of 110 kW [4]. The maximum output power of the Integrated Starter Generator (ISG) connected with Internal Combustion Engine (ICE) is 30 kW with a maximum output torque of 290 Nm [4]. "This bus is designed with a maximum speed as 70 km/h, and the bus should accelerate from 0 km/h to 50 km/h in 23 s [4]." Figure 1.11 shows the power-train structure of the entire system.
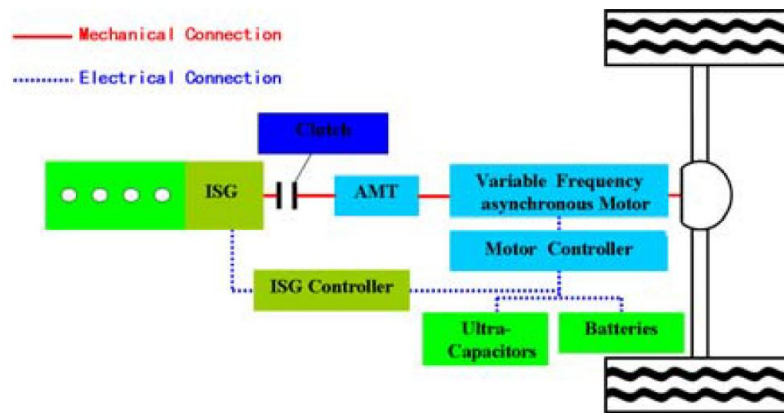
Figure 1.11. Power-train structure of a hybrid city bus [4].

As mentioned earlier, this paper shows simulation results for two battery/ultracapacitor systems: one with a direct parallel connection, and one with a DC/DC converter, which is in turn connected in series with the ultracapacitor. Figure 1.12 shows the first system. As can be seen in figure 1.12, the ultracapacitor and battery have been represented by their equivalent circuit models, and a simple circuit was chosen to represent the ultracapacitor. In this circuit, the ultracapacitor shares the same terminal voltage with the battery. The input current will be divided into two portions based on the circuit parameters.
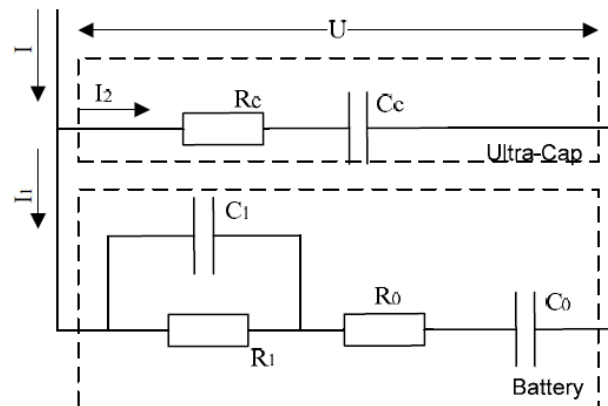
Figure 1.12. Battery in direct connection with an ultracapacitor [4].

Simulation results show that the battery experiences much smaller stress when connected with the ultracapacitor in this simple control-free manner. Figure 1.13 shows a test current applied to the circuit. The test current is a train of multi-valued rectangular waveform with variable widths showing a charging period followed by a discharging period in an alternating fashion. The red curve is the current drawn or injected in the battery while the dashed green curve is the ultracapacitor current. One notices that the battery experiences slightly less than half of the system current.
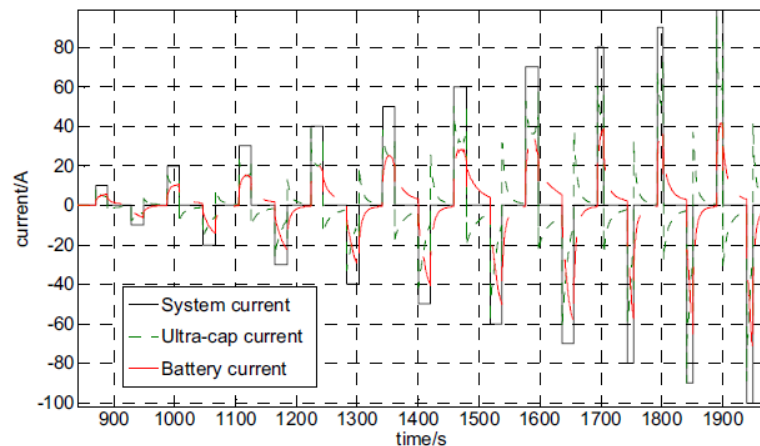
Figure 1.13. Battery in direct connection with an ultracapacitor [4].

Figure 1.14 shows a zoomed in version of the previous one to make it clear which device is responsible for which portion of the total system current in the parallel connection ESS. The ultracapacitor clearly takes care of the majority of the current as expected and desired.
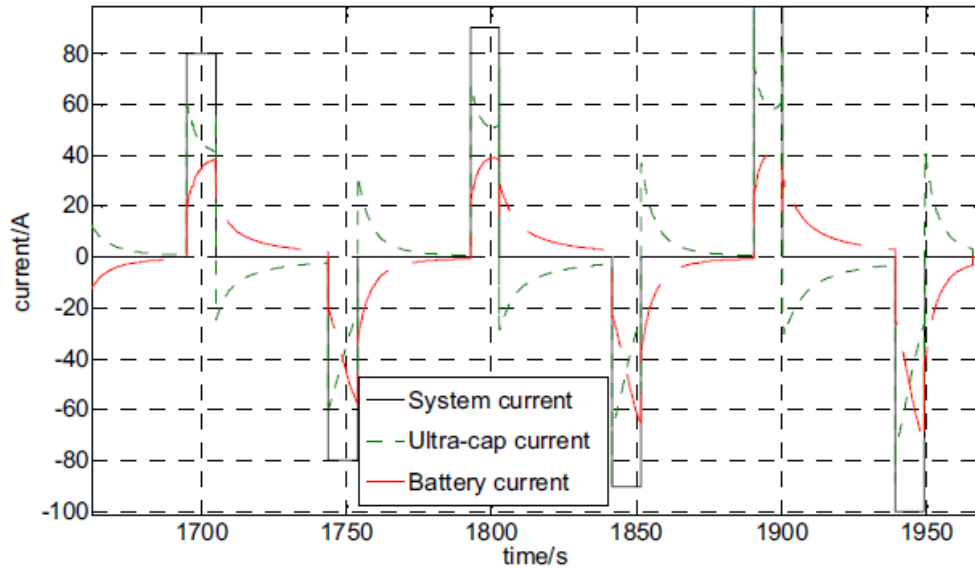
Figure 1.14. Battery in direct connection with an ultracapacitor [4].

In the second circuit, shown in figure 1.15, the ultracapacitor does not share the same terminal voltage with the battery. The DC/DC converter is the step separating the two energy storage devices, and it is what controls the amount of current the ultracapacitor experiences versus the amount of current the battery is responsible for. The input current hence will not be divided into the ultracapacitor and the battery solely based on the circuit parameters as the control system will govern the current drawn from or injected into the ultracapacitor.
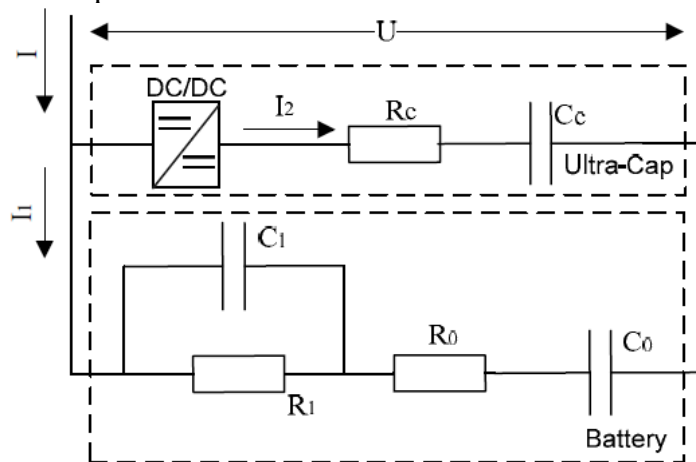
Figure 1.15. Battery in connection with an ultracapacitor through a DC/DC convertor [4].

In figure 1.16, a train of an alternating rectangular current waveform similar to the one applied in the first circuit has also been applied to the second circuit involving the DC/DC converter. Obviously, this circuit shows a larger ultracapacitor current share compared with the uncontrolled case. The battery therefore has a responsibility for about one third of the drawn or injected current leading a battery lifetime enhancement. The dashed red curve is for the battery while the continuous green one shows the ultracapacitor current.
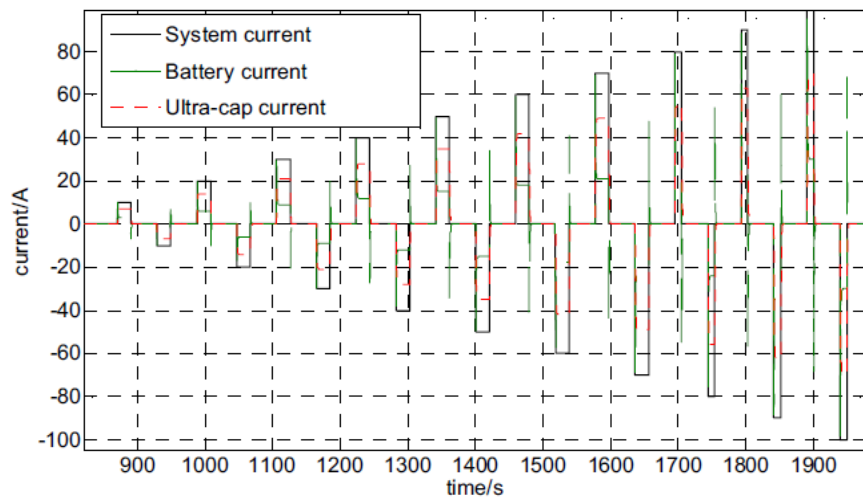
Figure 1.16. Battery in direct connection with an ultracapacitor [4].

Figure 1.17 shows a zoomed in version of figure1.16 to make it clear which device is responsible for which portion of the total system current in the parallel connection ESS with a DC/DC converter.
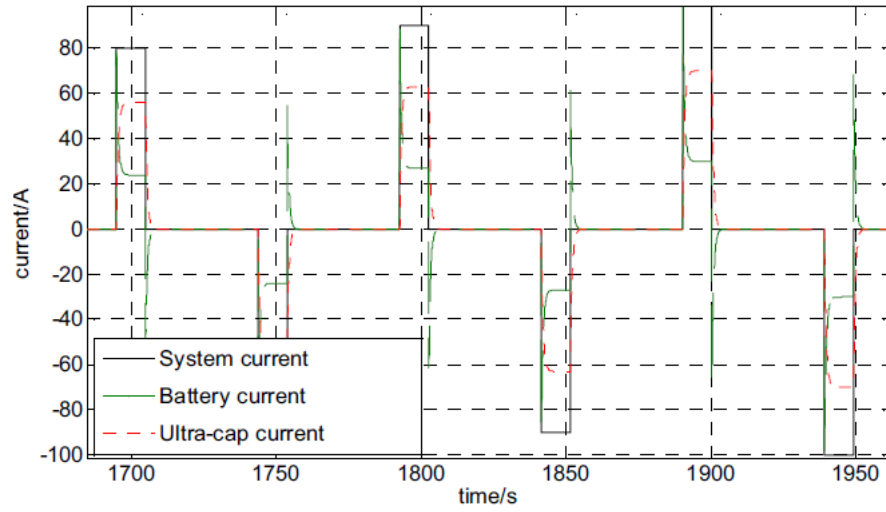
Figure 1.17. Battery in direct connection with an ultracapacitor [4].

Chapter 2. Engine cranking requirements

This chapter discusses the electrical requirements imposed on the hybrid system under consideration. In order to have a complete understanding of the requirements imposed on the system, it is important to understand the chemical reactions that take place in a lead acid battery. However, the design of the hybrid ESS only took into consideration the requirements from an electrical point of view. These requirements are battery terminal voltage, current, capacity, power, and energy. A typical automobile circuitry is provided by figure 5.1 in chapter 5.

When searching the literature trying to find precise details about the electrical requirements for internal combustion engine (ICE) cranking, ambiguous and often incomplete information was found. Hence, a number of tests were conducted on a few automobiles having different engine sizes and different lead acid battery capacities. In each of these tests battery voltage and current waveforms were acquired at a rate of 5000 samples per second. From these two waveforms, instantaneous power and energy curves can be obtained. These four waveforms, i.e. voltage, current, power, and energy, can provide us with the necessary design requirements for the hybrid ESS to be utilized for ICE start-stop.

The instantaneous power curve is produced by obtaining the instantaneous product between the voltage and current waveforms. The energy waveform is obtained by running a Riemann sum on the power curve, which is the digitized form of integrating the power curve over time. The cranking test results for a number of automobiles by various car manufacturers are shown in figures 2.1-2.6

Toyota Solara 2002:
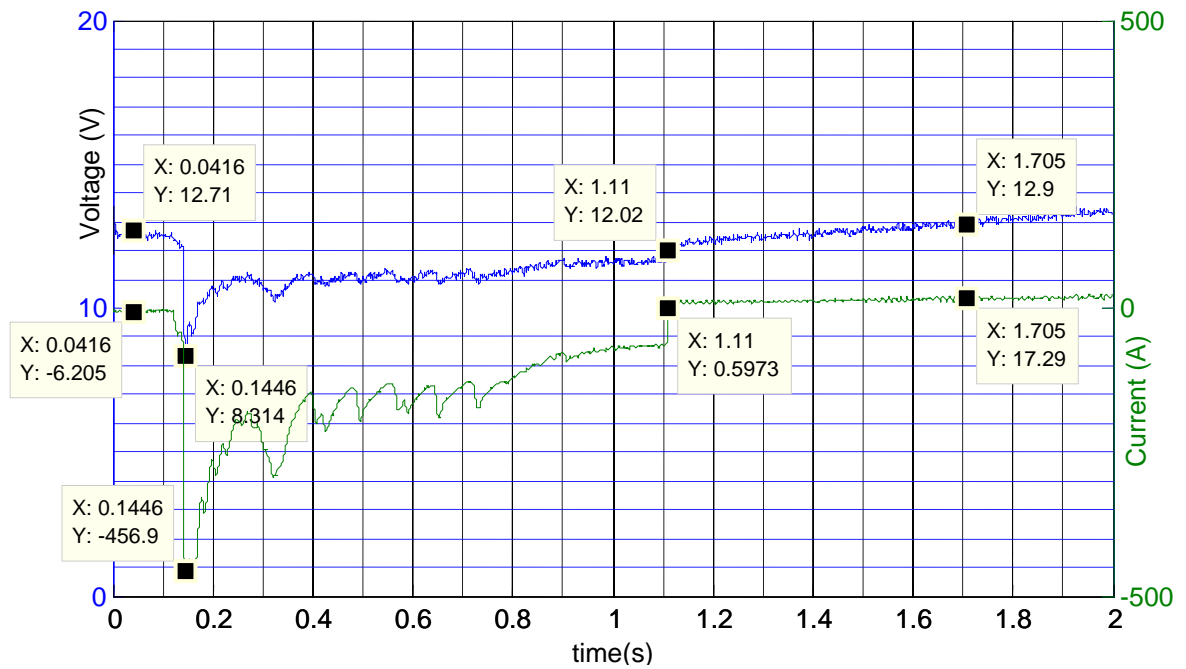
Figure 2.1 a. Voltage and current waveforms during cranking for a Toyota Solara 2002.
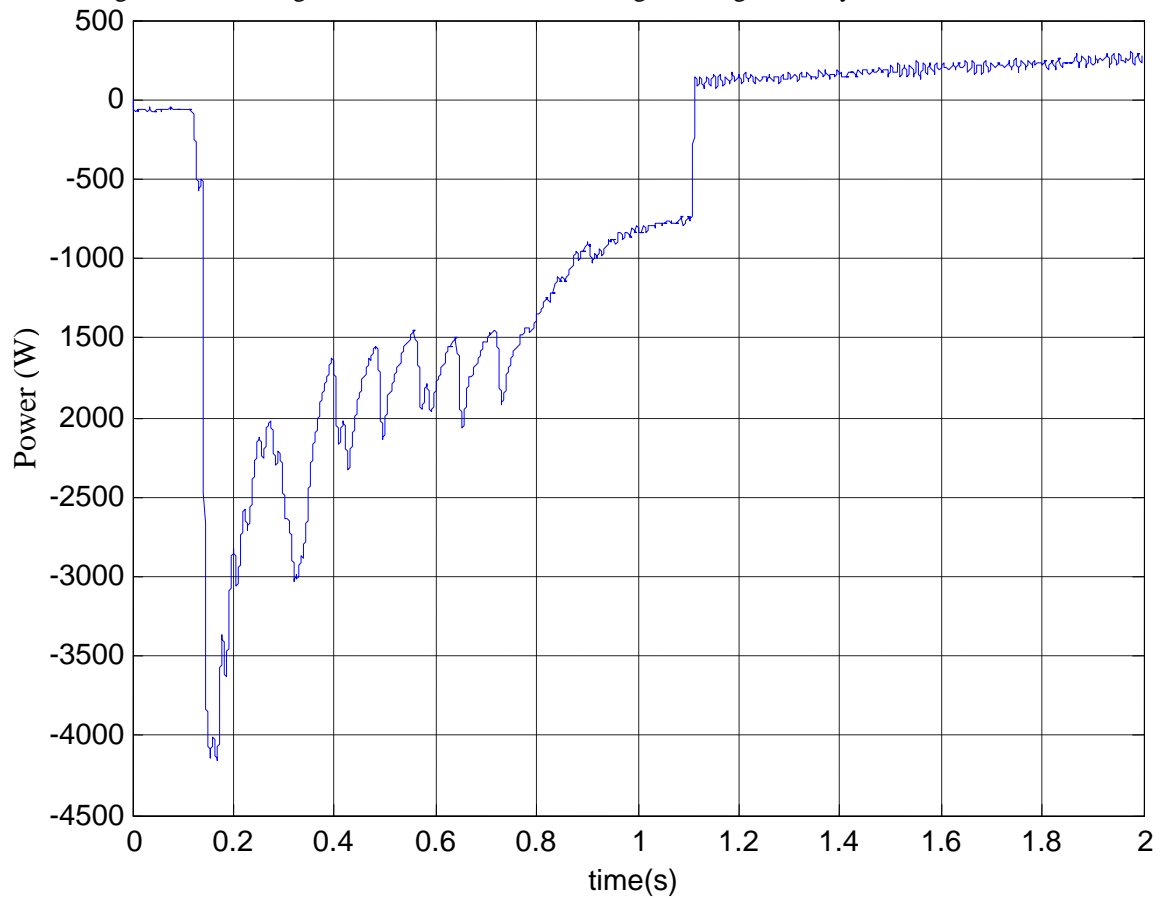
Figure 2.1 b. Instantaneous power curve during cranking for a Toyota Solara 2002.
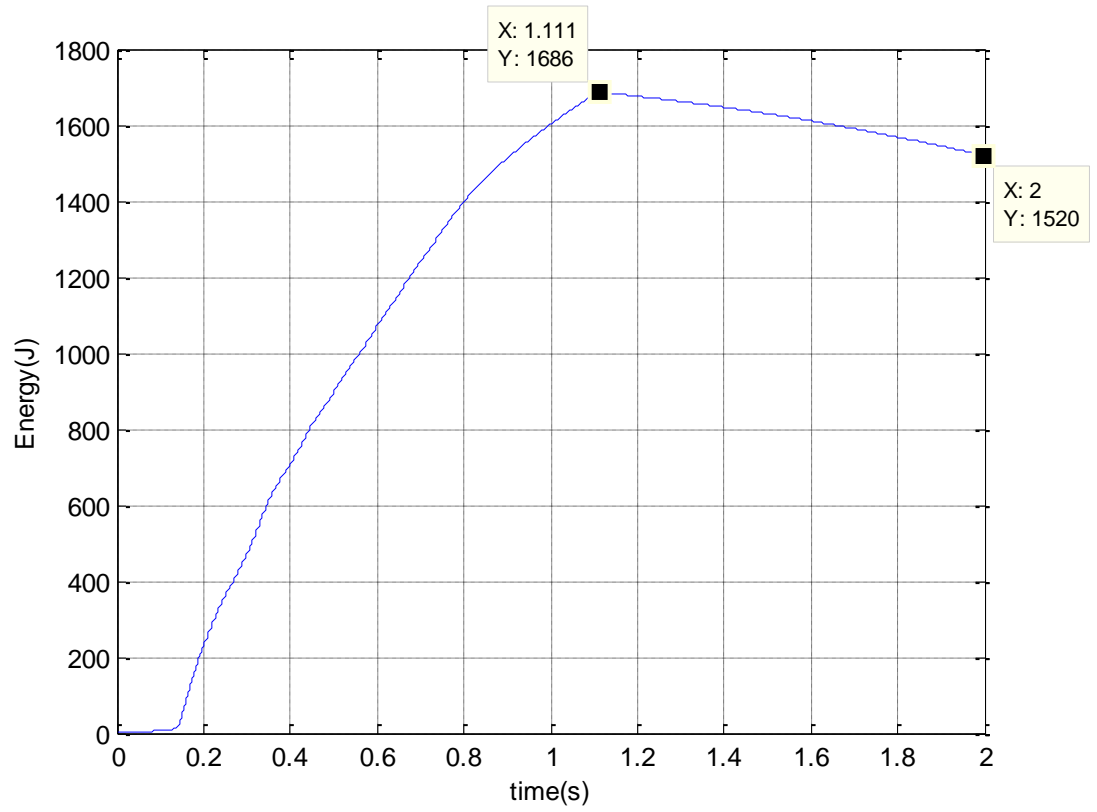
Figure 2.1 c. Energy waveform during cranking for a Toyota Solara 2002.

Buick 1998
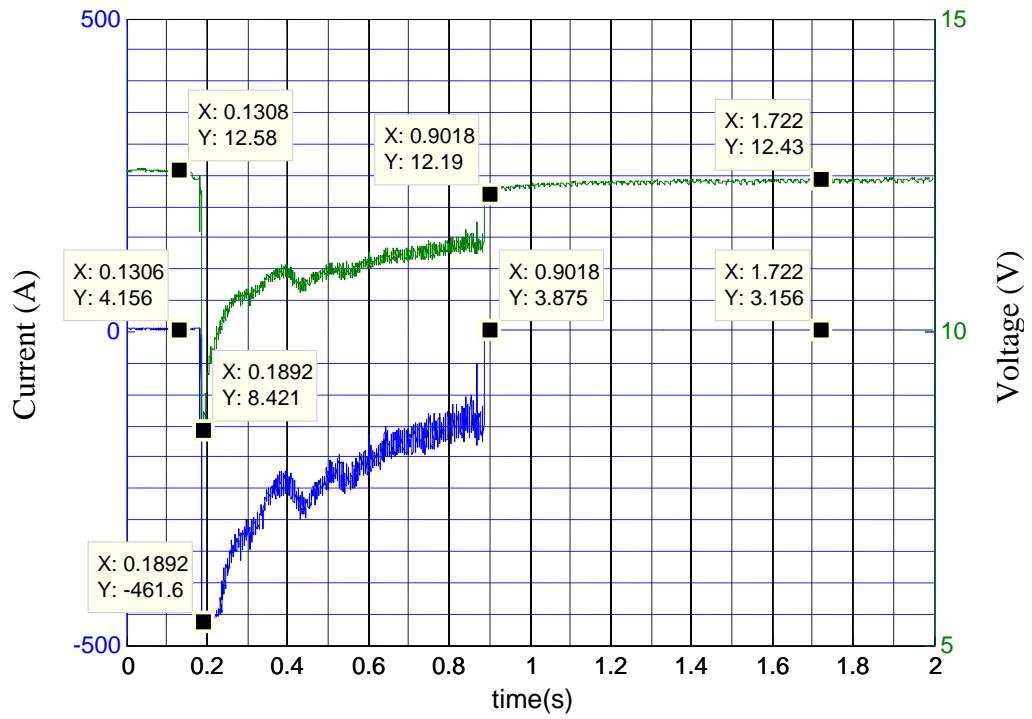
Figure 2.2 a. Voltage and current waveforms during cranking for a Buick 1998.
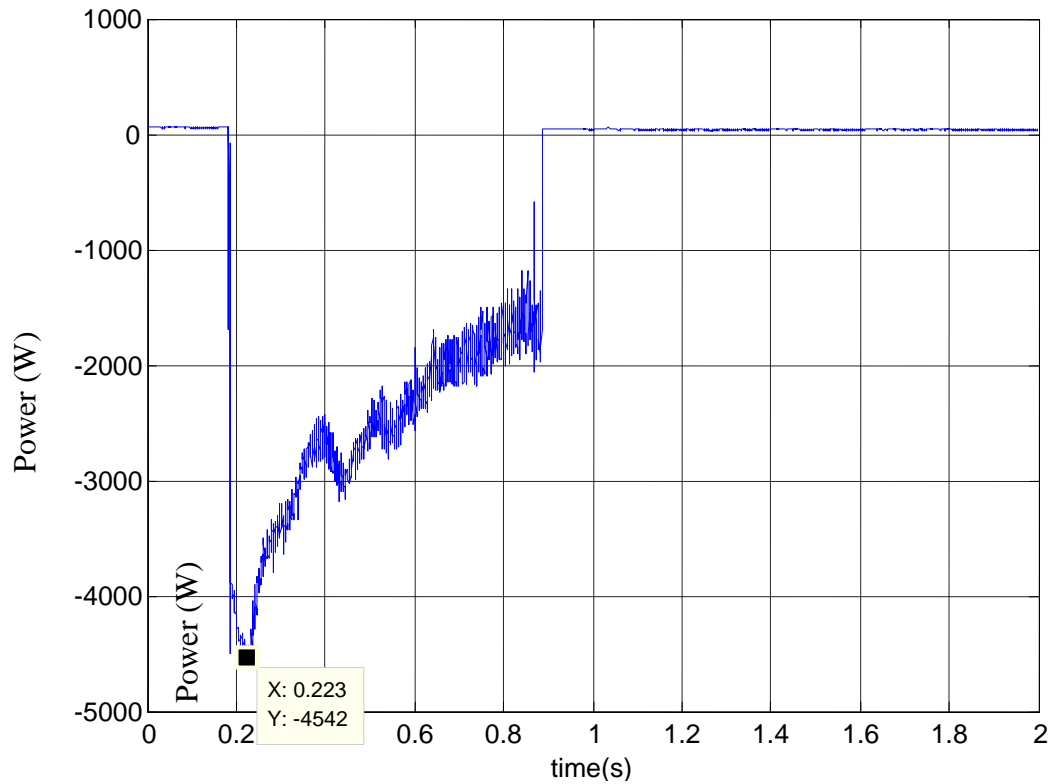
Figure 2.2 b. Instantaneous power curve during cranking for a Buick 1998.
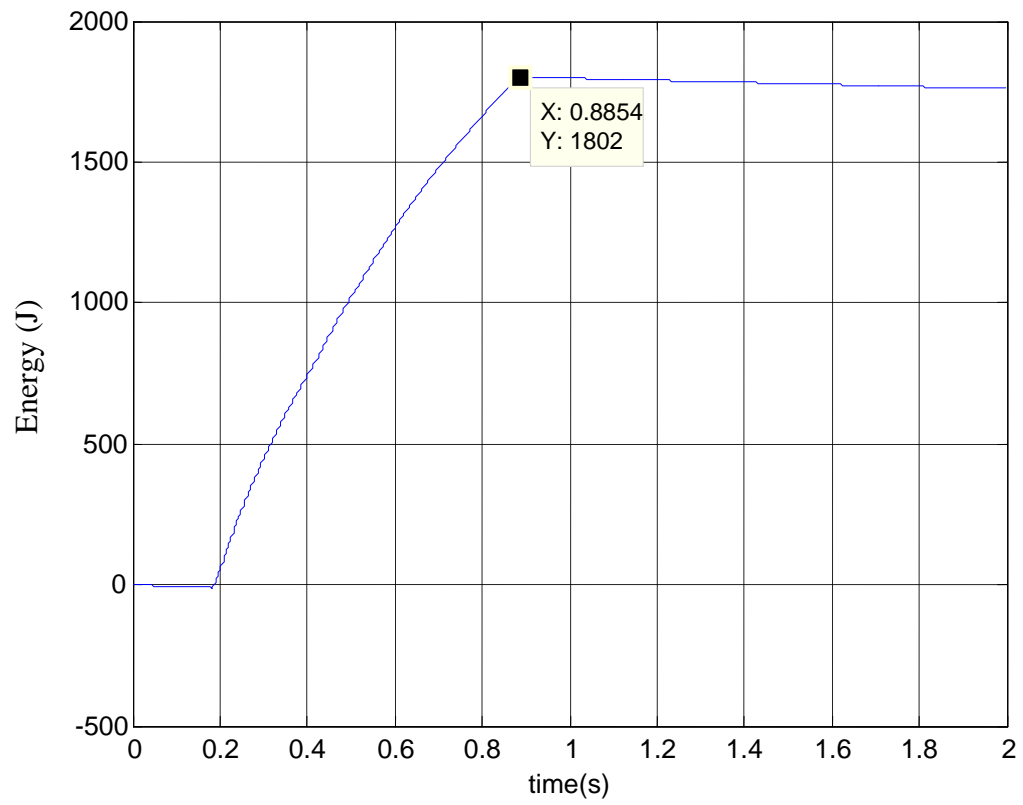
Figure 2.2 c. Energy curve during cranking for a Buick 1998.

Ford Focus
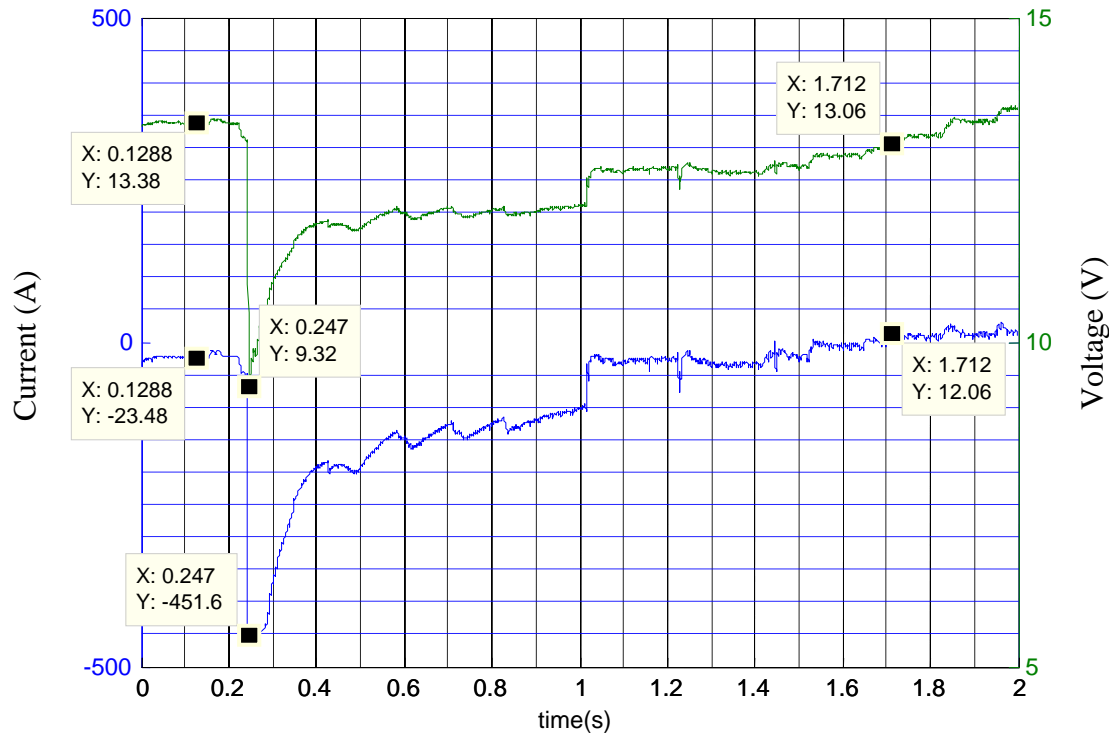
Figure 2.3 a. Voltage and current waveforms during cranking for a Ford focus.
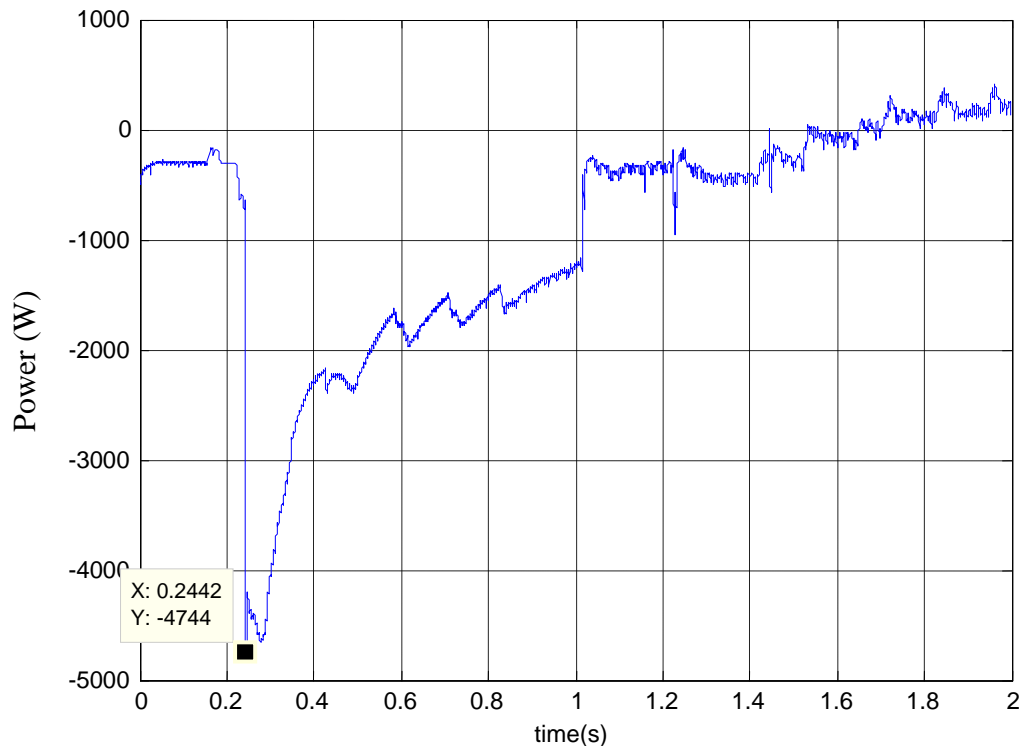
Figure 2.3 b. Instantaneous power curve during cranking for a Ford focus.
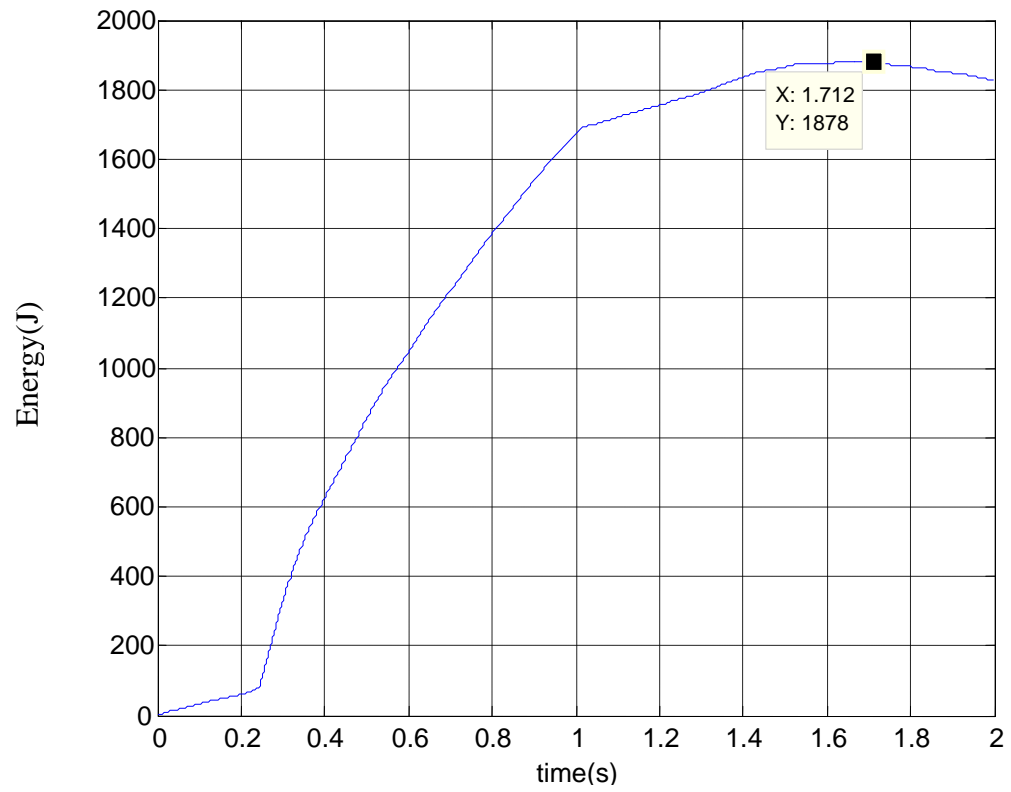
Figure 2.3 c. Energy curve during cranking for a Ford focus.

Saturn Vue V4 2004
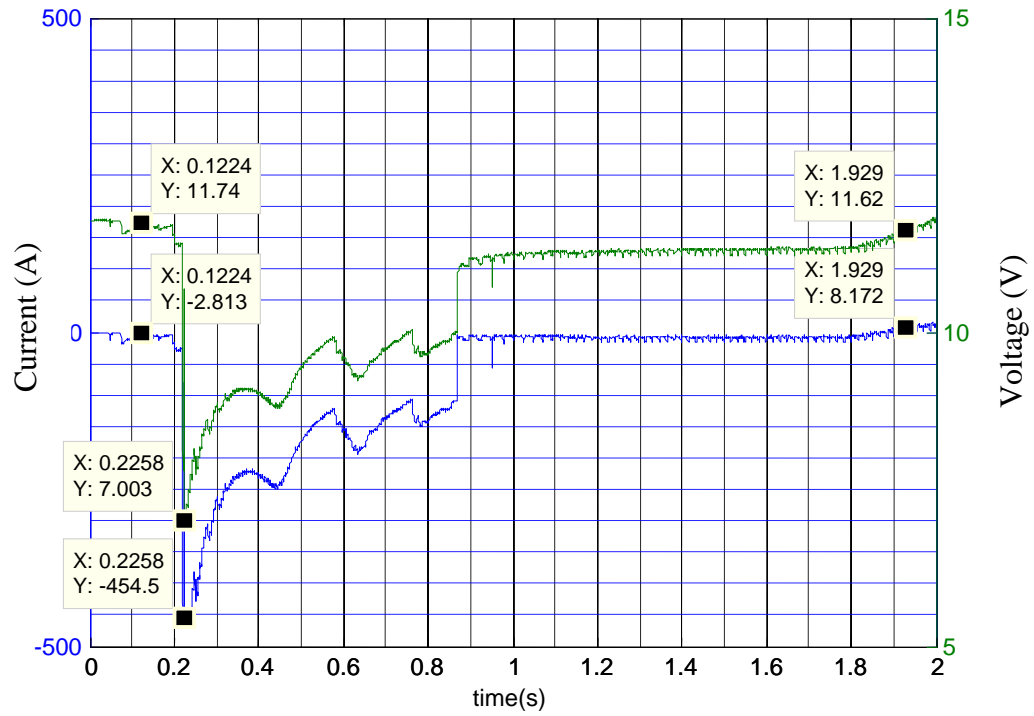
Figure 2.4 a. Voltage and current waveforms during cranking for a Saturn Vue V4 2004.
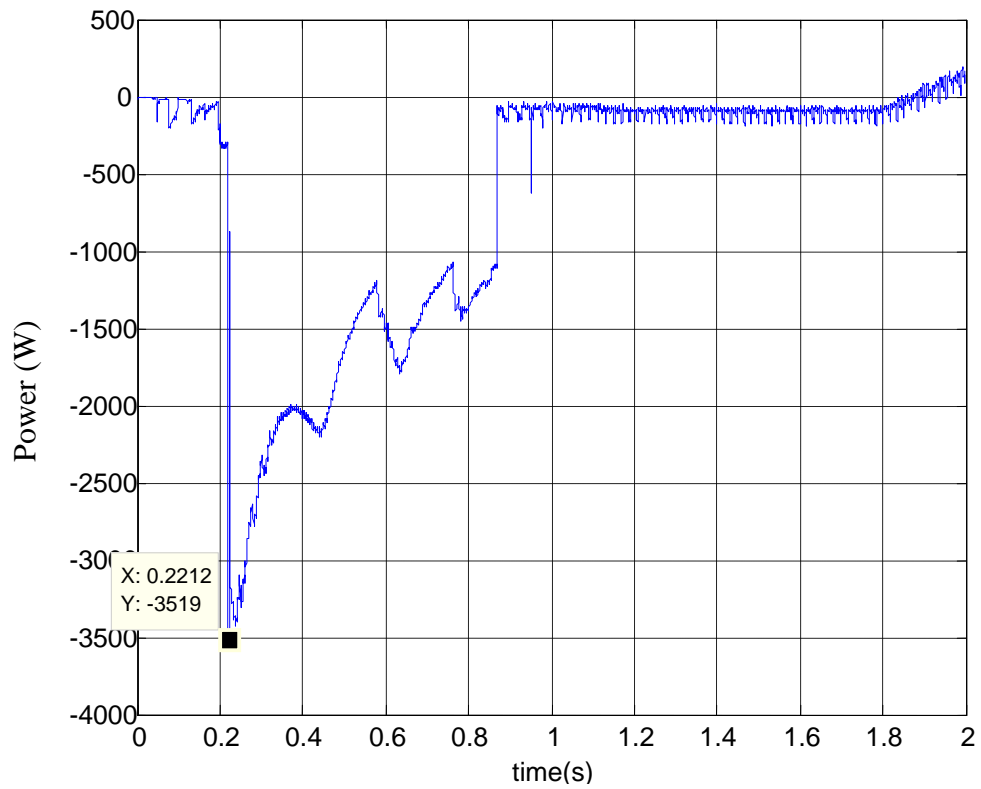
Figure 2.4 b. Instantaneous power curve during cranking for a Saturn Vue V4 2004.
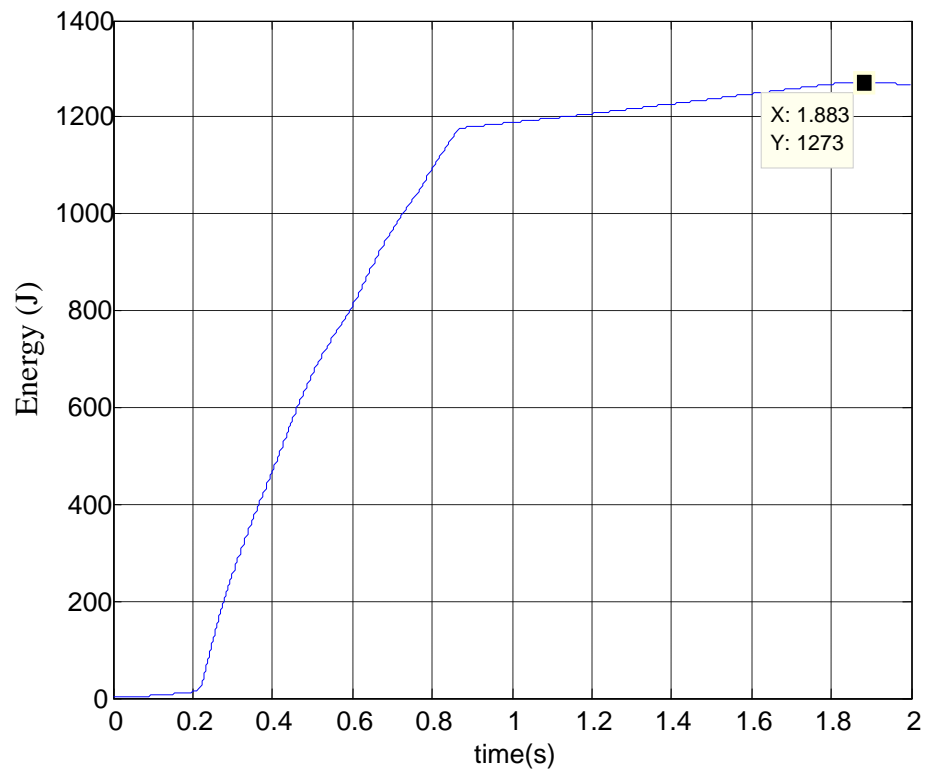
Figure 2.4 c. Energy curve during cranking for a Saturn Vue V4 2004.

Honda Civic 2011
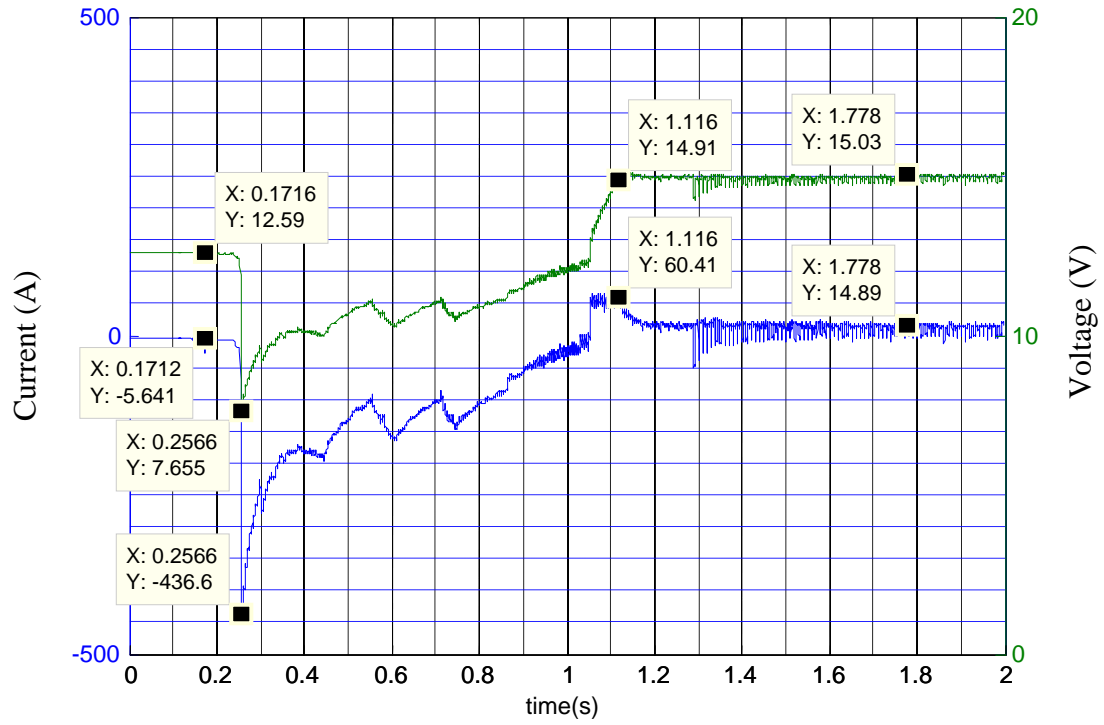
Figure 2.5 a. Voltage and current waveforms during cranking for a Honda Civic 2011.
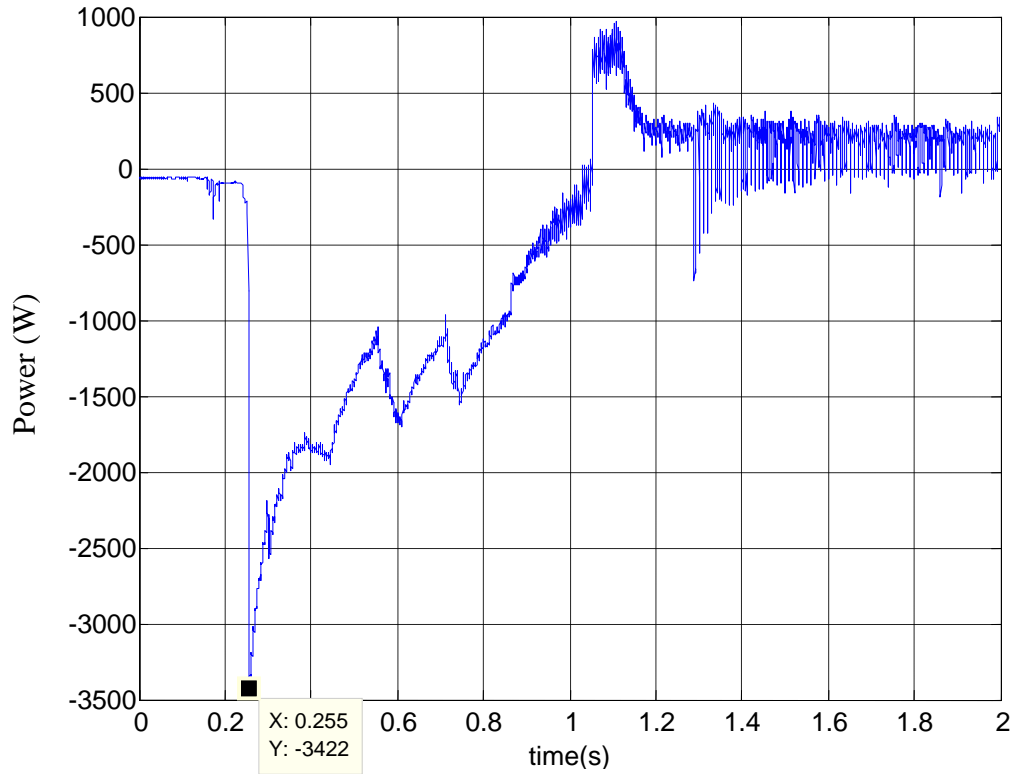
Figure 2.5 b. Instantaneous power curve during cranking for a Honda Civic 2011.
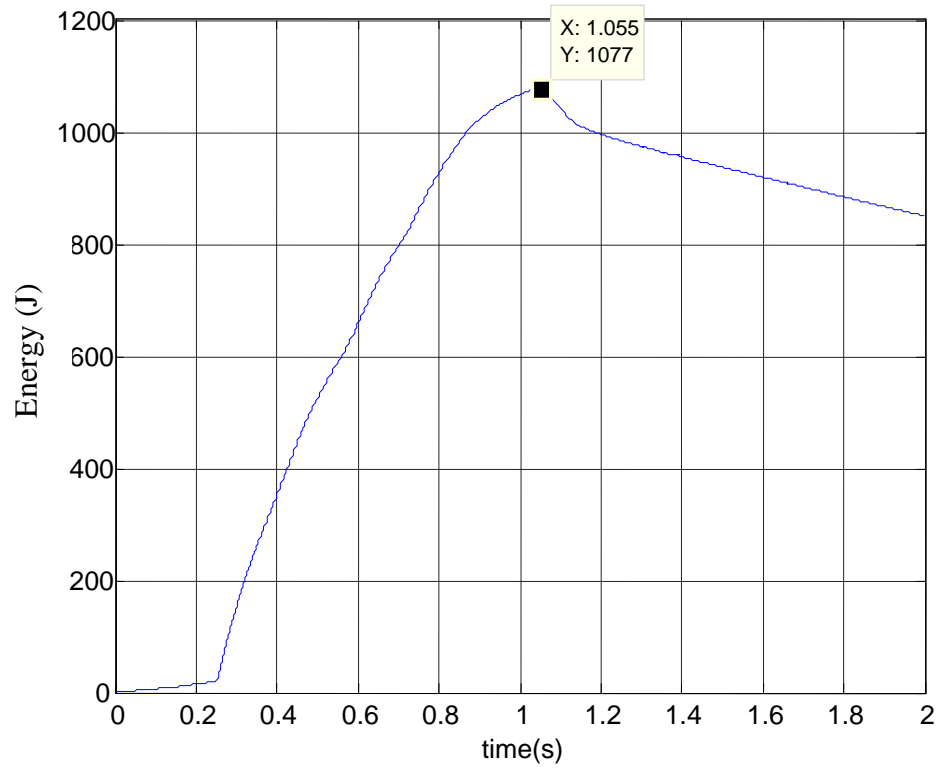
Figure 2.5 c. Energy curve during cranking for a Honda Civic 2011.

Audi V6 1996
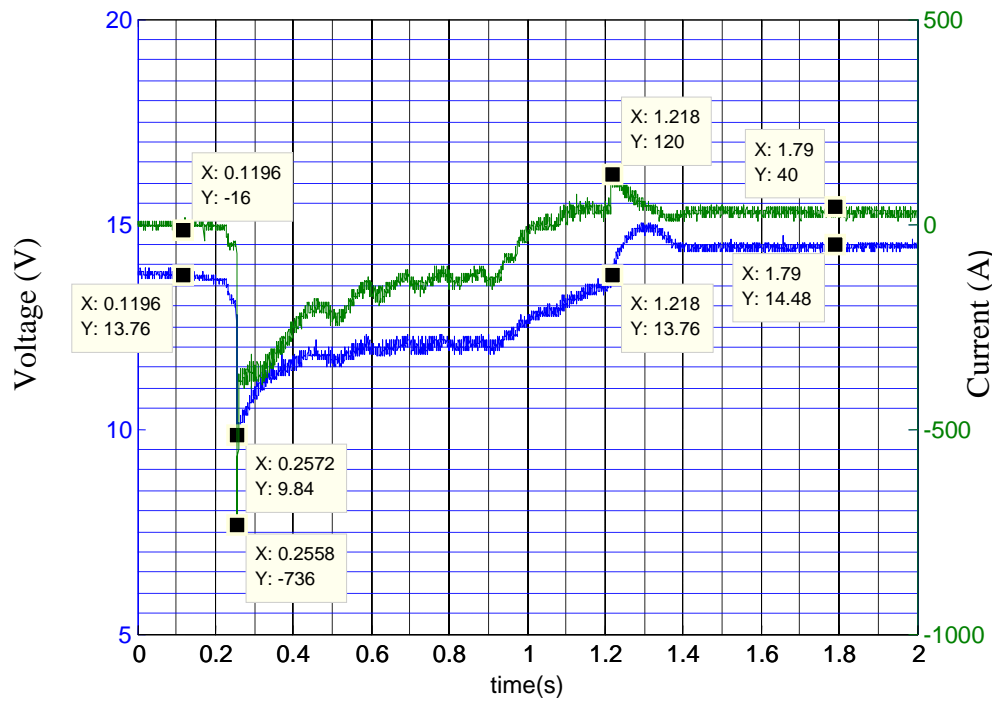
Figure 2.6 a. Voltage and current waveforms during cranking for an Audi V6 1996.
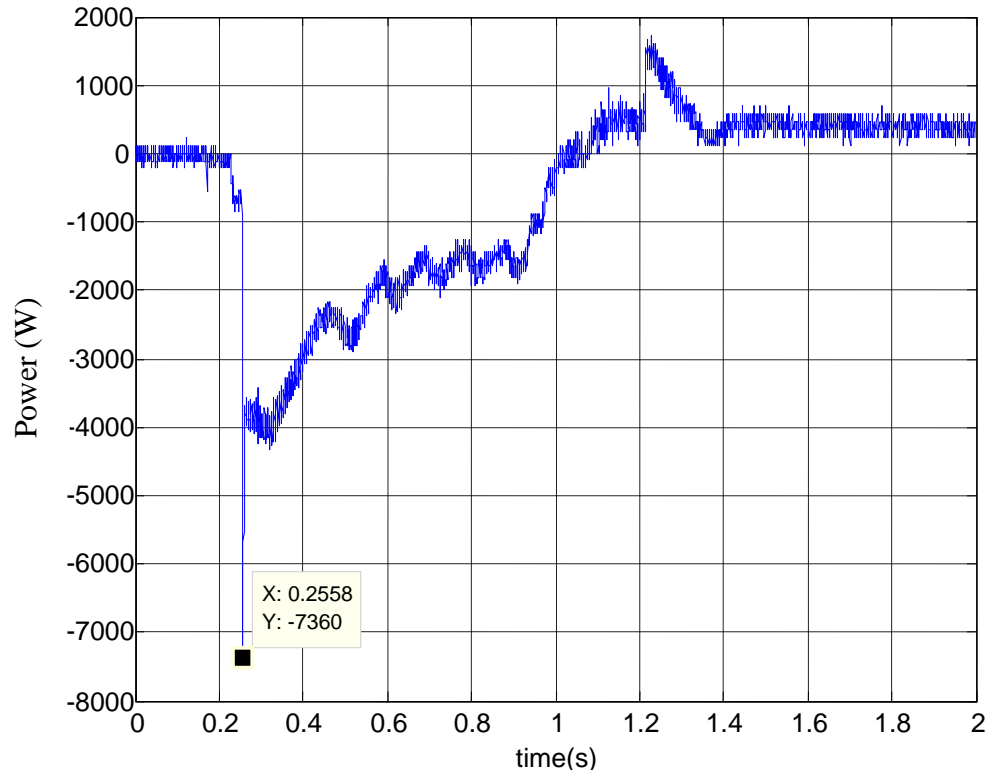
Figure 2.6 b. Instantaneous power curve during cranking for an Audi V6 1996.
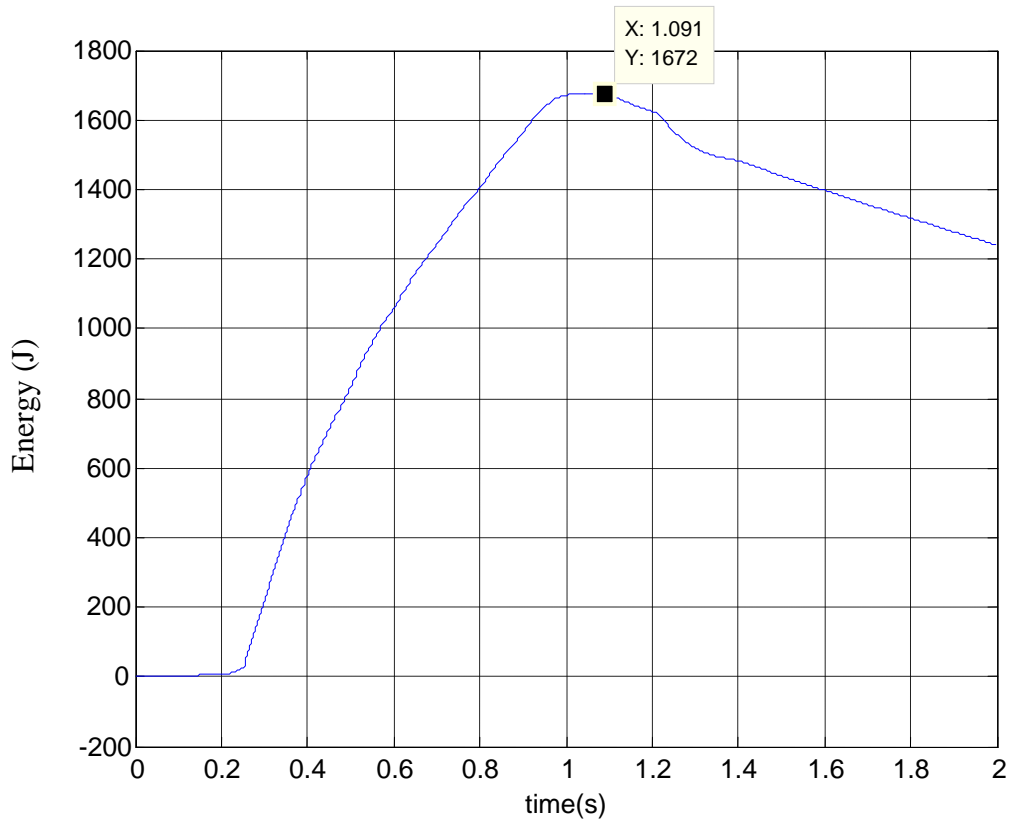
Figure 2.6 c. Energy curve during cranking for an Audi V6 1996.

The test results for the aforementioned cars are shown in three graphs labeled a, b, and c respectively. The first graph, labeled a, is the voltage/current graph versus time. The second and third graphs, b and c, are the instantaneous electrical power and energy respectively. In all of these graphs, one can see three time-based stages: stage 1 is the pre-cranking stage or the time period when the car key is in the position right before cranking, stage 2 is the cranking stage where both voltage and current waveforms experience activity associated with the engine pistons requiring different torques according to piston order and position, and stage 3 starts when cranking ends and alternator action kicks in resulting in the beginning of the charging stage. Table 2.1 shows a comparison between six car brands having different engine sizes and model years.

Table 2.1. Comparison of electrical requirements for six car brands.

Car Make	year	Engine Size	Cranking Voltage	Cranking Current	Maximum Cranking Power	Cranking Energy
Toyota Solara	2002	3.0 L	8.3 V	457 A	4.2 kW	1.7 kJ
Buick	1998	3.1 L	8.4 V	462 A	4.54 kW	1.8 kJ
Ford Focus	2013	2.0 L	9.3 V	452 A	4.74 kW	1.88 kJ
Saturn Vue	2004	2.24 L	7 V	455 A	3.52 kW	1.27 kJ
Honda Civic	2011	1.8 L	7.7 V	437 A	3.4 kW	1.08 kJ
Audi V6	1996	2.8 L	9.84 V	736 A	7.36 kW	1.67 kJ

Chapter 3. Li-ion ultracapacitor modeling

3.1 Ultracapacitor types and structure

Ultracapacitors, also known in literature as super capacitors are high capacitance elements that can store large amounts of energy. Unlike batteries where energy storing or release is accompanied with chemical reactions, no chemical reaction happens during normal operation of an ultracapacitor. This allows for a very large number of charging/discharging cycles for ultracapacitors as well as larger power density, compared with batteries. The dominant ultracapacitor technology is Electrochemical Double Layer Capacitor (EDLC). Unlike ordinary capacitors, EDLCs do not contain a dielectric between their conductive plates. Instead of a dielectric, electrolytic substance fills the space between two electrodes. Electrodes are covered with highly porous activated carbon. The high porosity of activated carbon results in a very large equivalent surface area of the electrodes. By applying voltage, positive ions are attracted to the negative electrode, while negative ions move towards the positive electrode. The ion transfer inside the electrolyte is rapid leading to very quick charging and discharging capability leading to high power density. This process is known as non-Faradaic where the moving ions do not react with the electrodes at which they accumulate [41]. As a result, a double layer of particles with opposite-sign charges is formed. Since the electric charges are separated by an infinitesimal distance, on the nanometer scale, and due to the large surface area of the electrodes, the resulting capacitance is very high, typically on the level of several hundreds of farads.

One main disadvantage of EDLC ultracapacitors is their relatively small terminal voltage, which is less than 2.7V, and it should not be exceeded in order to prevent electrolyte oxidation. One way to increase the amount of energy that can be stored within an ultracapacitor is to find a way to increase the maximum terminal voltage. The main difference in construction of a lithium-ion ultracapacitor, compared with the EDLC, is that only the positive electrode (cathode) is made from activated carbon. The negative electrode (anode) is made from lithium-doped structure-controlled carbon, which enables lower negative potential of that electrode. This results in a larger net voltage that prevents electrolyte oxidation. Figure 3.1 summarizes the structural differences between the three technologies of Li-ion batteries, ELDC, and Li-ion ultracapacitors. In Li-ion batteries, where a Faradaic process exclusively takes place, the energy is stored within the chemical reactants, which when reacting with the electrodes immersed in the electrolyte, release a large amount of charge leading to high energy density. However, the kinetics of the reactions at the electrodes and the mass transfer of Lithium cations from the negative electrode through the electrolyte to the positive electrode slow down the release rate of charge leading to lower power capability [41]. In Li-ion ultra-capacitors, which have a hybrid structure, both Faradaic and non-Faradaic processes take place. The ion movement through the electrolyte, which contains a dissolved lithium salt, in the non-Faradaic process is partly responsible for the conduction of electricity when the two electrodes are connected through a load. The other portion of conduction happens when the Lithium cations react with the negative electrode in the Faradaic reaction.

The maximum voltage of a lithium-ion ultracapacitor is 3.8V. Since the energy stored in capacitor is proportional to the square of its terminal voltage, this voltage

increase results in quadratic increase in the amount of energy that can be stored in the lithium-ion ultracapacitor. In addition, the Li-doped electrode creates very large capacitance at negative electrode, which practically doubles the total capacitance of the cell. However, lithium-ion ultracapacitors cannot be operated under a minimum voltage, which prevents a full discharge. This voltage is 2.2V resulting in the allowed operating voltage in the range between 2.2V-3.8V. Despite this limitation, lithium-ion ultracapacitors offer about four times as much energy density as ELDC.
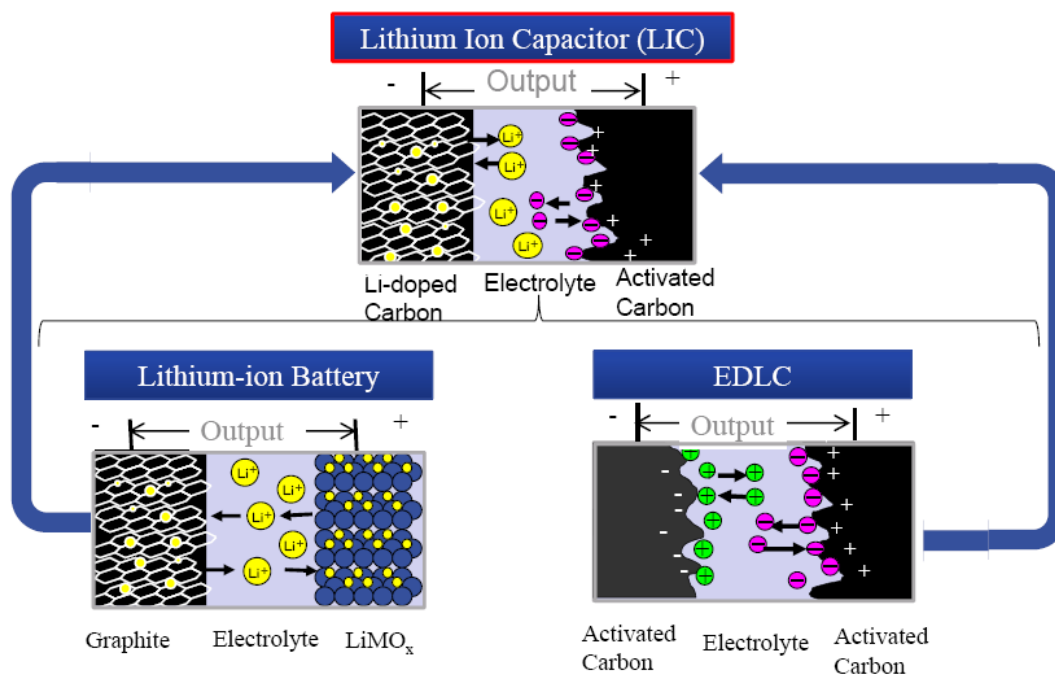
Figure 3.1. Structural comparison of Li-ion batteries, EDLC capacitors and Li-ion ultracapacitors.

In order to use ultracapacitor in renewable energy systems, or electric vehicles, appropriate dynamic model is needed. Dynamics models are necessary for modeling and simulation of systems that contain ultracapacitors. There are several approaches to the ultracapacitor modeling, and they can be divided into the three main groups. The first group of models consists of equivalent circuit models [19]-[24], [46]. These models are usually built from series and parallel RC circuits, whose combination results in accurate

voltage-current behavior on the terminals of an ultracapacitor. Parameters of the model are resistances and capacitances, and they are determined based on measurements of current and voltages during charging and discharging processes.

The Second class of ultracapacitor models is physical-based models [25]-[26]. These models are based on electrochemical and physical properties and they can be very accurate. Beside voltage and current characteristics, such models accurately describe internal behavior of ultracapacitor and they are suitable for studies where electrochemical phenomena are of interest. However, it is very hard to develop this type of model. There are many parameters unknown and hard to obtain. Also, physical and chemical laws that govern ultracapacitor behavior are very complex. A special class of models combines equivalent circuit with physical modeling approaches [27]-[28].

Finally, ultracapacitors can also be modeled using neural networks trained by a training set that contains voltages, currents, and temperatures obtained during the measurement phase on a real ultracapacitor [29]. A fully trained neural network then produces accurate output for a given input. The disadvantage of this approach is higher computational cost, compared to equivalent circuit models.

In this dissertation, a simplified equivalent circuit model of a lithium-ion ultracapacitor is proposed. This model consists of only five elements. The simple model allows for easier integration into system level modeling. In order to accurately represent voltage-current behavior of an ultracapacitor, nonlinear voltage dependent capacitance is used. This model is intended for use in complex power electronic systems where a larger, more detailed model, would considerably extend simulation time.

Table 3.1 shows a comparison between the energy capacities of a Lithium-ion ultracapacitor with some other types of energy storage devices. Table 3.2 below presents the electrical properties of a Li-ion ultracapacitor cell.

Table 3.1. Comparison of Li-ion ultracapacitor properties with other energy storage devices.

ESS	Energy Density (Wh/kg)	Power Density (W/kg)	Cycle Life
Lithium-Ion U-cap	10-20	900-9000	>100000
EDLC	2-8	500-5000	>100000
Lead-Acid battery	30-50	100-200	200-300
NiMH battery	60-120	250-1000	300-500
ZBB	85-90	300-600	2000

Table 3.2. Properties of an ultracapacitor cell under study.

Property	Nominal	limit
Voltage (V)	3	3.8
Current (A)	10-70	200
Low Voltage Cutoff (V)	2.4	2.2

3.2 Ultracapacitor testing

Testing the ultracapacitors has been carried out to identify the parameters of the potential electrical model capable of estimating its electrical behavior under practical charging/discharging conditions. For this purpose, a series of DC and AC tests was performed on an 1100 F ultracapacitor. Careful attention was paid to the ultracapacitor terminal voltage, and these tests were designed to keep the terminal voltage within the range specified earlier. Real time voltage and current were measured at a rate of 100 samples per second to assure enough precision.

It is important to note that the tests have been conducted at various temperatures. This is an important detail as cell and ambient temperatures play a major role in energy storage system management and design. Therefore, the impact of temperature has been taken into account in the electrical equivalent model of the ultracapacitor. The operating temperature range is from -20° C to 70° C. The ultracapacitor was tested under temperatures from -15° C to 65° C with increments of 10° C. The test data were logged using Lab View and NI Compact RIO real-time hardware module taking measurements for terminal voltage and Open-Circuit Voltage (OCV) under a sampling frequency of 100Hz. Figure 3.2 shows the test setup and the dimensions of the ultracapacitor in millimeters. A refrigerator was used for reaching lower temperatures.
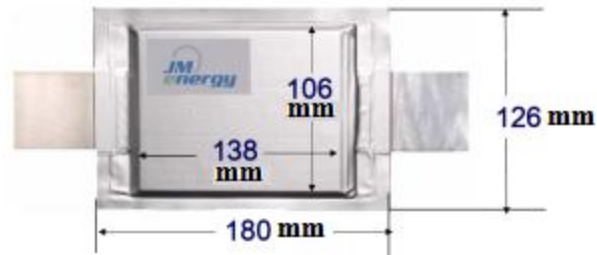
Figure 3.2. A picture of the ultracapacitor dimensions and the test setup.

A. DC tests

For these tests, the ultracapacitor was charged and discharged by a DC rectangular wave with several amplitudes ranging from 10A to 80A in increments of 10A under fixed temperature for each set of tests. The charging is done in constant current mode until the terminal voltage reaches 3.8V at which it switches to constant voltage mode to avoid exceeding the upper voltage limit. During discharging, the same algorithm is applied and the mode switches from constant current mode to constant voltage mode when the terminal voltage hits 2.2V. Evidently, constant voltage mode is reached faster

when the current rate is higher. The control scheme was deployed using Lab View. The

purpose of this test is discussed under section 3.3 of this chapter. Figure 3.3 shows one

example of charging and discharging tests conducted on the ultracapacitor.
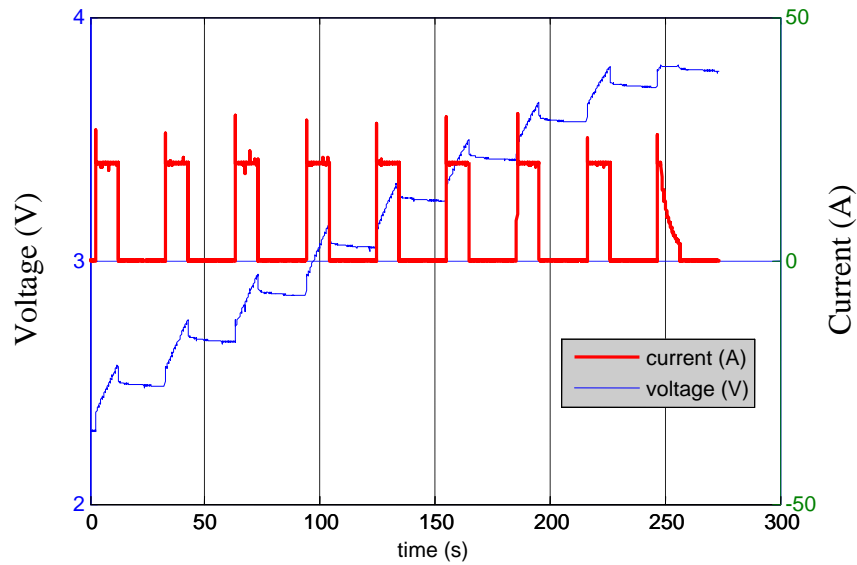
(a)
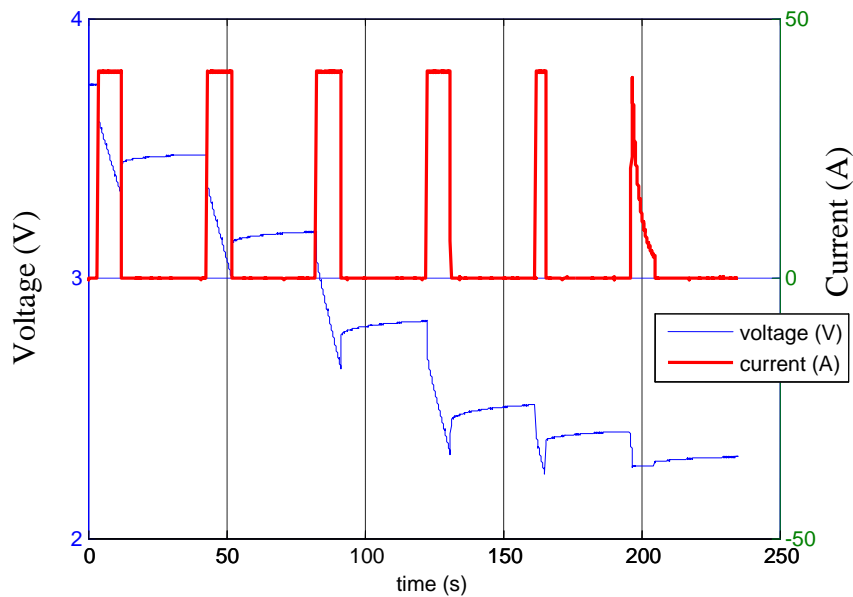
(b)

Figure 3.3. (a) DC charging test with 20A (b) DC Discharging test with 40A.

In Figure 3.3(a), the voltage increases in a nearly linear fashion until the terminal voltage reaches 3.7 V. The cell can handle 3.8 V, but it was decided to have 3.7 as the upper voltage limit during charging for safety reasons.

B. AC tests

In this test, an AC current was applied to charge the ultracapacitor while measuring voltage and current. Due to the limitations imposed by the capabilities of the power supply, the AC signal was shifted up by a DC offset. Therefore, the current provided by the power source can be decomposed into two frequency components– DC and AC. As a result, the voltage across the ultracapacitor was expected to be a sinusoid riding over a ramp, which was observed in the tests. Figure 3.4 shows both the AC current and terminal voltage of the ultracapacitor in this test. The frequencies used in this test were 0.025Hz, 0.05 Hz, and 10 Hz through 70 Hz in increments of 10 Hz. Low frequency tests showed a larger phase shift between the applied current signal and the ultracapacitor terminal voltage signal. The purpose of this test is also discussed under section III.
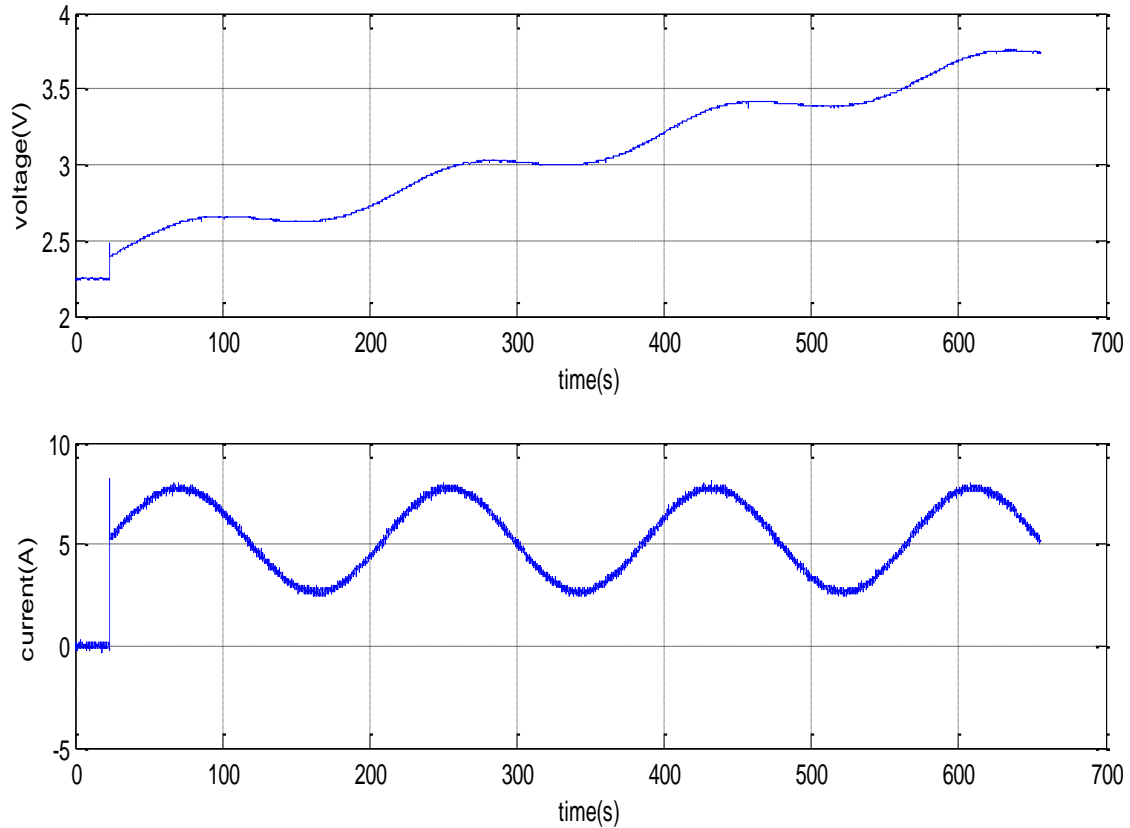
Figure 3.4. AC test results. Upper graph: terminal voltage. Lower graph: charging current.

3.3 Capacitor based modeling

To create an electrical model capable of describing the ultracapacitor behavior, the test data were used first by examining the DC and AC test results. The modeling that utilizes data from the DC tests has four main stages as follows:

A.   Internal capacitance (C_o)

The DC test was performed so that the ultracapacitor would be charged for a certain period of time and given a period of time to rest. This was repeated until the ultracapacitor reached the upper limit voltage (3.8V). The fact that the ultracapacitor open circuit voltage increases as more energy is stored in it suggests that one component

of the ultracapacitor has to be a major energy storage device, i.e. an internal capacitor. This capacitor is given the symbol C_o and is calculated by dividing the change in charge by the change in voltage. To obtain the value of charge, Columbic count was performed according to equation 3.1.

$$\Delta Q(A \cdot s) = \sum_{i=1}^{t} I(t_i) \times \Delta t_i \qquad (3.1)$$

This Columbic count is one step toward finding a direct relationship between the ultracapacitor internal capacitance, C_o, and its open circuit voltage (OCV). For this reason, a direct current was injected into the ultracapacitor during charging tests and a direct current was also drawn from it during discharging. These tests were done at different current rates to investigate if this capacitance is current independent. The current waveform is mainly a train of pulses in the constant current mode and it becomes nonlinear in the constant voltage mode. Voltage is recorded throughout the entire test. The points on the voltage waveform at which the current is zero are the OCV measurements. Capacitance is calculated at each OCV point by dividing the difference in charge, the amount of charge that the ultracapacitor received or lost, by the change in OCV. Equation 3.2 explains this operation.

$$C_o(OCV_i) = \frac{\Delta Q_i}{\Delta OCV_i} = \frac{\sum_i I_i(t)\Delta t}{\Delta OCV_i} \qquad (3.2)$$

Where $C_o(OCV_i)$ is the internal capacitance at a point i, $I_i(t)$ is the current rate at the point i, and Δt_i is the time interval during which the current rate is $I(t_i)$. Δt in this case is consistently equal to 0.01 second. Figure 3.5 below shows how the internal

capacitance is calculated. It shows the calculation of $C_o(OCV)$ for 10A charging DC test in room temperature. The shaded area under the current first pulse is the amount of charge the capacitor received during the first period of that test. Capacitance is calculated at each OCV point and the capacitance vs. OCV curve for all the DC tests under 25^oC is shown in Figure 3.6.
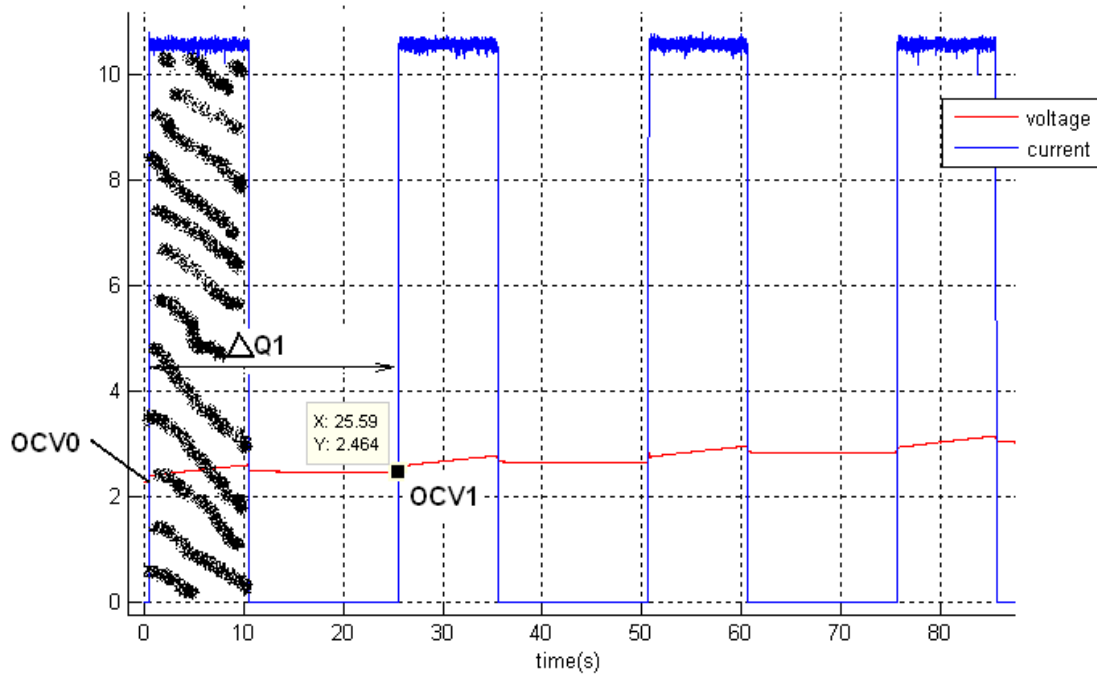
Figure 3.5. Calculation of electric charge and voltage for determining the main capacitance.
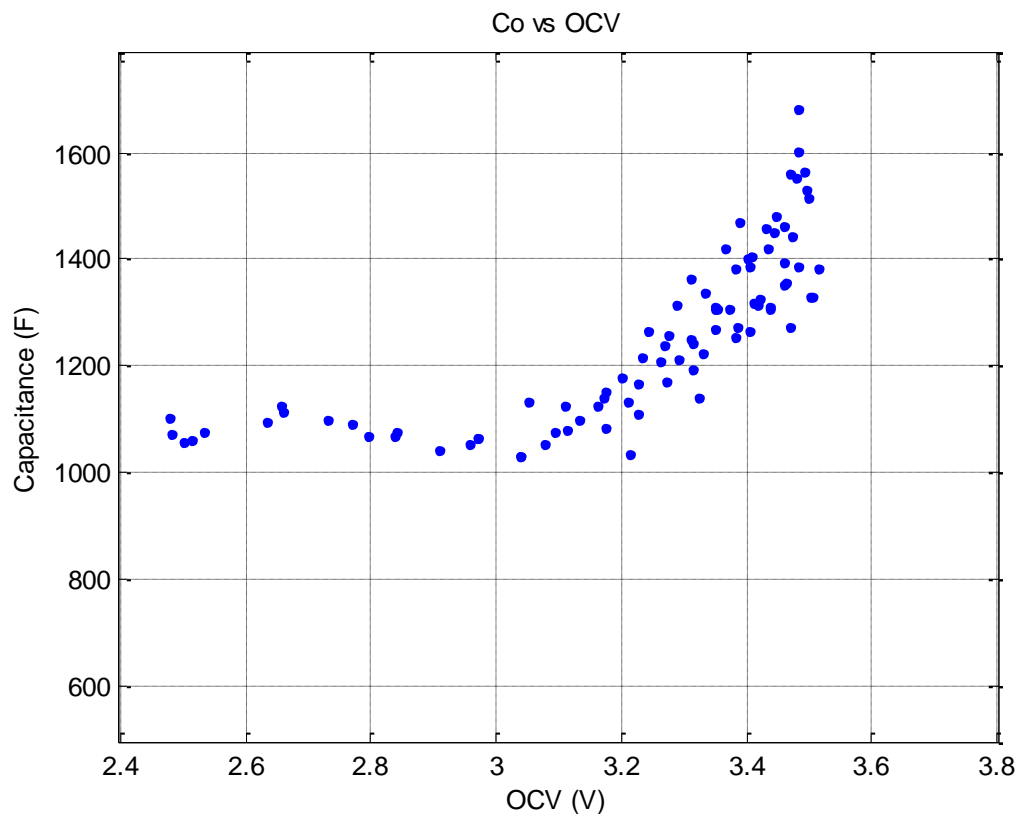
Figure 3.6. Internal capacitance for all DC tests under 25° C.

In the voltage region between 2.2V and 3V, the capacitance exhibits a somewhat

constant value of 1100F. This is the region where only the non-Faradaic process takes

place on the positive electrode (cathode) as can be seen in figure 3.6 reflecting a constant

purely capacitive behavior. The Faradaic process, on the other hand, takes place in the

voltage region between 3V and 3.8 V on the negative electrode (anode), an activity

reflected by the increasing capacitance versus voltage in this voltage region. These

processes can be explained by examining the reactions that take place between the

electrolyte and the electrodes as provided by the manufacturer of this type of LIC in [41].

"The electrolyte consists of lithium hexafluorophosphate (LiFP$_6$) in Ethylene carbonate

(EC), propylene carbonate (PC), and diethyl carbonate (DEC) [41]." Lithium

hexafluorophosphate dissolves in the electrolyte as Li$^+$ cations and PF$_6^-$ anions the

activity of which is responsible for the charging and discharging processes of the LIC. Li^+ cations in the electrolyte intercalate into the activated carbon electrode (cathode) while charging from 2.2 V until 3 V. If charging continues between 3V and 3.8V, then the Faradaic process starts to occur exhibiting PF_6^- anions moving towards the Li-doped activated carbon electrode (anode) adsorbing on it, which is an activity simultaneous with further Li^+ cations moving towards the cathode and intercalating into it. The pre-doped Lithium inside the negative electrode does not participate in the charging and discharging processes; it only pins the potential of this electrode at a highly negative value enabling the LIC to store more energy by increasing the voltage across its electrodes [41]. To find a relationship between the capacitance and OCV, a 4th degree polynomial interpolant was used to fit the data.

$$C_o(OCV) = a \cdot OCV^4 + b \cdot OCV^3 + c \cdot OCV^2 + d \cdot OCV + e \quad (3.3)$$

where the values of a, b, c, d, and e are the coefficients of the polynomial. Figure 3.7 shows the internal capacitance of all the 10A tests at different temperatures. The steps explained above for finding an interpolating polynomial were applied to each one of these sequences of capacitance values to get an expression for their corresponding internal capacitance as a function of OCV.
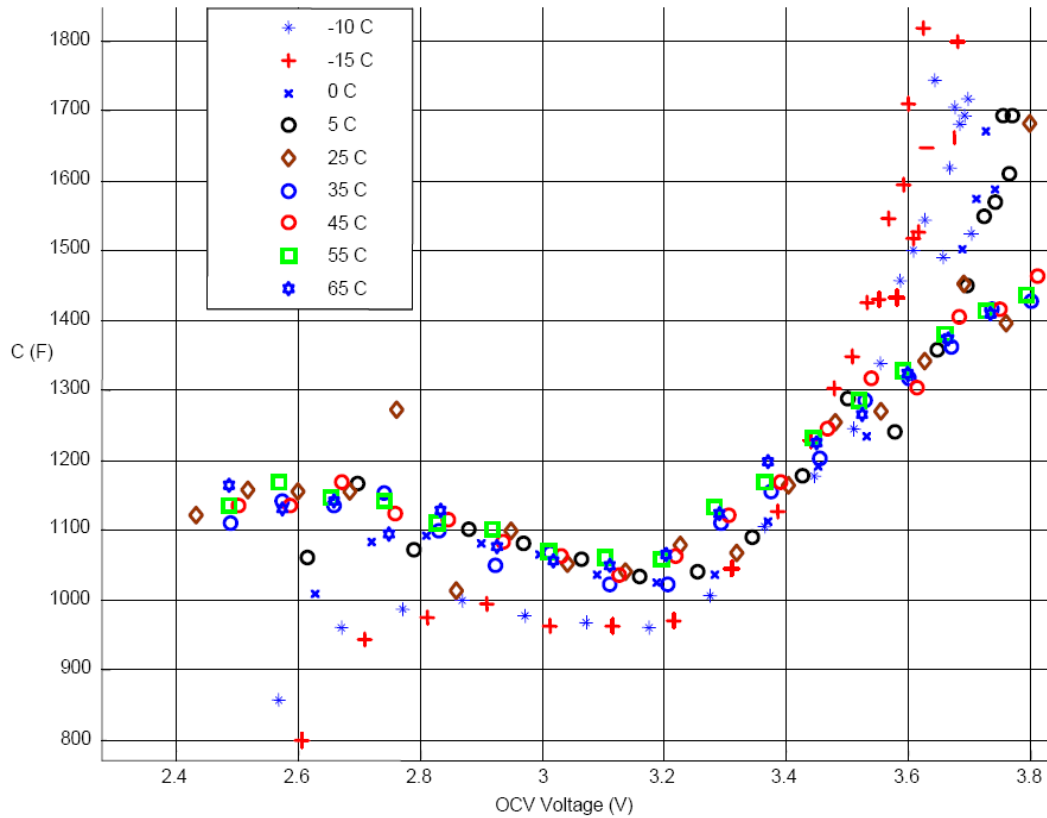
Figure 3.7. Internal capacitance for 10A at all temperatures.

Figure 3.8 shows the capacitor-based electrical circuit model proposed in this dissertation for the ultracapacitor. The self discharging resistance explains why the ultracapacitor voltage slowly declines when electrically disconnected. The series branch elements model the dynamics of the waveforms during charging and discharging. The series resistance, which is the sum of the resistance in the cell plus the junction resistance, is a common element for most storage devices. C_{sa} and R_{sa} describe further dynamics as discussed in the following section.
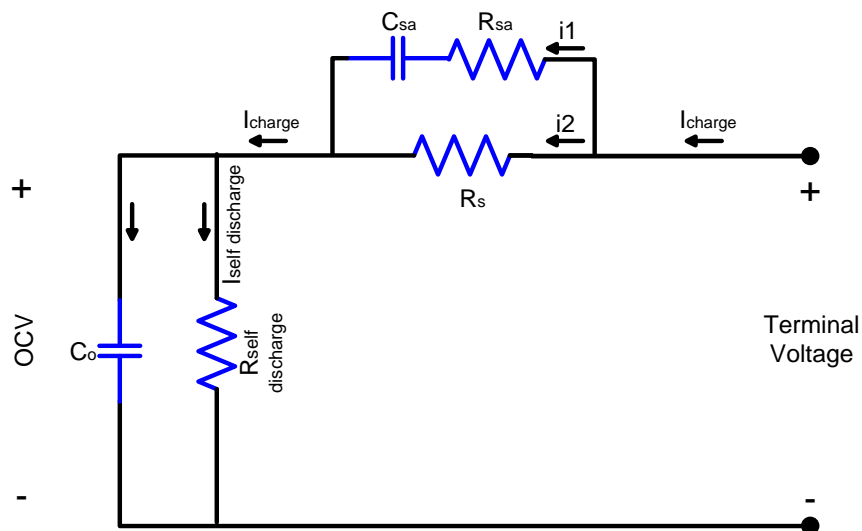
Figure 3.8. The proposed capacitor-based electrical model.

The interpolation of the internal capacitance versus OCV and temperature is provided in Figure 3.9. One notices that all capacitance curves intersect at a value of voltage equal to 3 V. This means the ultracapacitor is most stable at that value of voltage, and is recommended as the best voltage for shelf storage.
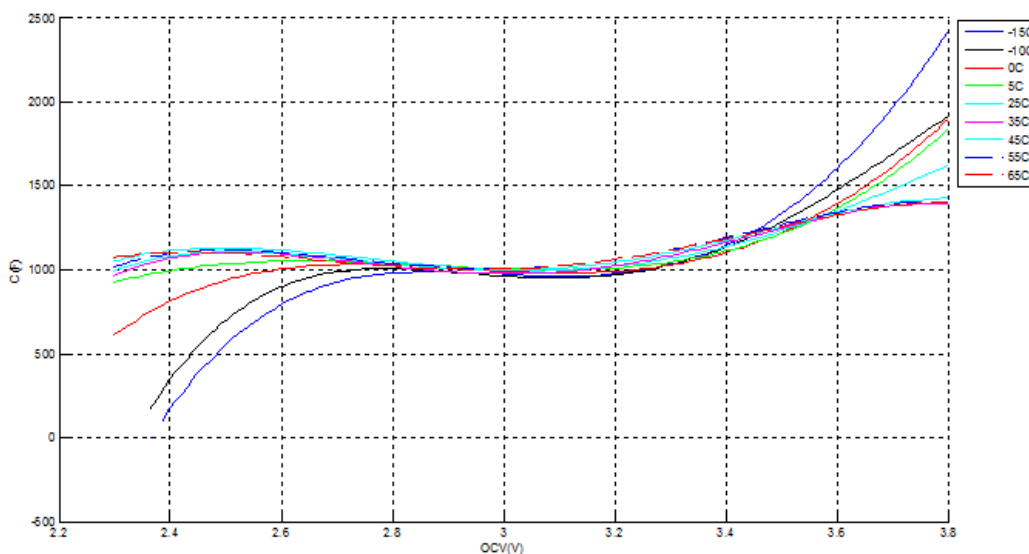
Figure 3.9. All capacitance curves projected on the C-OCV plane.

Figure 3.10 shows polynomial surface interpolation for the internal capacitance versus voltage and temperature. Since tests were conducted under discrete values of temperature, one needs to interpolate the curves in Figure 3.10 using a surface interpolant. A polynomial of the fifth degree for both OCV and temperature was used as an interpolating function. The result of this interpolation conducted by the surface fitting tool in Matlab is shown in Figure 3.10.
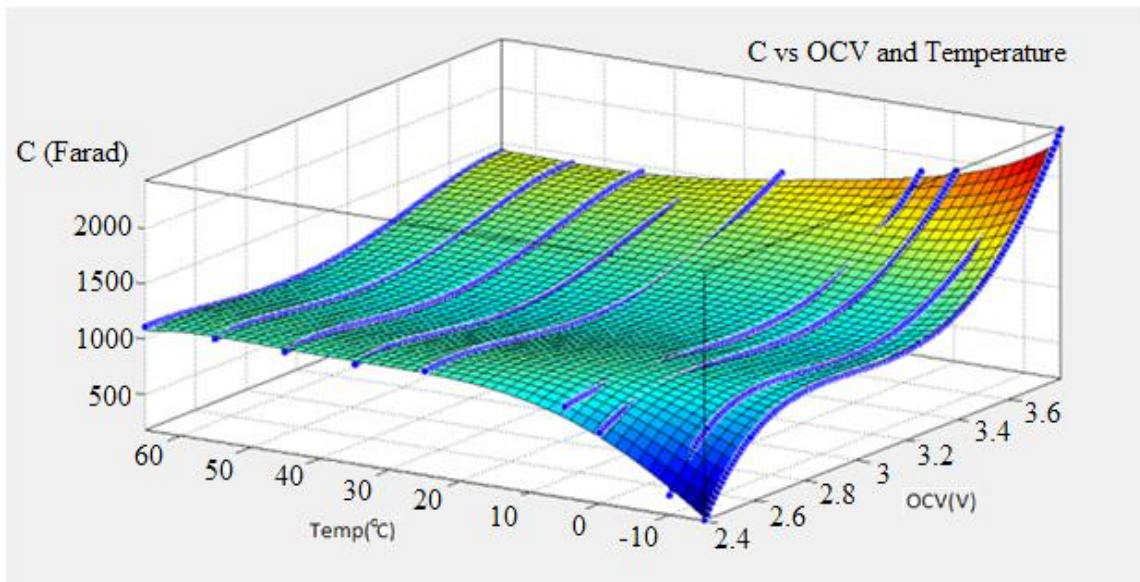
Figure 3.10. interpolation of capacitance curves.

The polynomial used has the form given in equation 3.4.

$$F(x,y) = p_{00} + p_{10}x + p_{01}y + p_{20}x^2 + p_{11}xy + p_{02}y^2 + p_{30}x^3 + p_{21}x^2y + p_{12}xy^2 + p_{03}y^3 + p_{40}x^4 + p_{31}x^3y + p_{22}x^2y^2 + p_{13}xy^3 + p_{04}y^4 + p_{50}x^5 + p_{41}x^4y + p_{32}x^3y^2 + p_{23}x^2y^3 + p_{14}xy^4 + p_{05}y^5 \quad (3.4)$$

where $F(x,y) = \text{Capacitance(OCV, Temp)}$

B.   Self discharging resistance

To find this resistance, the ultracapacitor terminal voltage needs to be monitored over a long period of time after charging it to different voltage levels. However, the value of this resistance is very large for this type of the ultracapacitor, e.g. the voltage did not change when the cell was stored on shelf for several days. According to test data conducted by manufacturer, the terminal voltage drops only by 5% after six months. This implies that the self discharging resistance can be considered to be infinite for short-term operations. For simulation purposes, a value of $1G\Omega$ was chosen for the self discharging resistance.

C.   Internal resistance (R_s)

When the ultracapacitor is being charged or discharged, one can notice a sudden decrease/increase in the measured terminal voltage. The internal resistance causes this jump in voltage. To calculate the value of the internal resistance, the difference between the terminal voltage at two samples when the charging or discharging starts or stops is calculated and divided by the current. Table 3.3 shows the internal resistance of the ultracapacitor at different temperatures.

Table 3.3. Internal resistance at various temperatures.

Temperature(^{o}C)	$R_s(\Omega)$
-15	35 m
-10	29.3 m
0	18.1 m
5	13.5 m
25	5.34 m
35	3.3 m
45	2.9 m
55	2.7 m
65	2.5 m
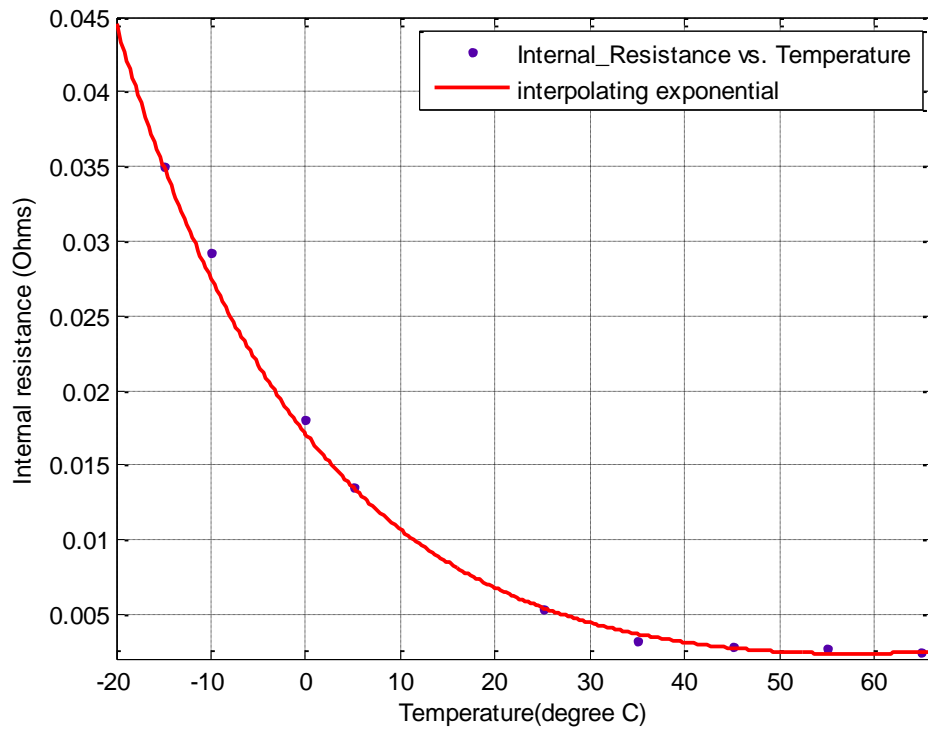
Figure 3.11. Internal resistance as a function of temperature.

This resistance does not vary with current rating or open circuit voltage. However, it significantly depends on temperature. Figure 3.11 shows this variation along with an exponential interpolant. The exponential interpolant is given by equation 3.5 to describe the internal resistance variation with temperature.

$$R_{int}(T) = a\ e^{bT} + c\ e^{dT} \qquad\qquad (3.5)$$

where

a = 0.0169468527888307

b = -0.0481885465804298

c = 0.000150364681152322

d = 0.0378531440857562

D. Series Branch Capacitance (C_{sa}) and Resistance (R_{sa})

During DC tests, one can notice changes in terminal voltage after charging/discharging stops. This process lasts for a few seconds before the terminal voltage reaches a steady state value equal to the OCV. This behavior suggests the existence of an RC component in series with the internal capacitance. This series-branch capacitor holds a charge when the ultracapacitor is operational and it loses this charge when the ultracapacitor becomes inactive. Figure 3.12 below shows the linear increase in terminal voltage during charging, the sudden drop in voltage right after charging current stops, and the relatively slow decay in voltage.
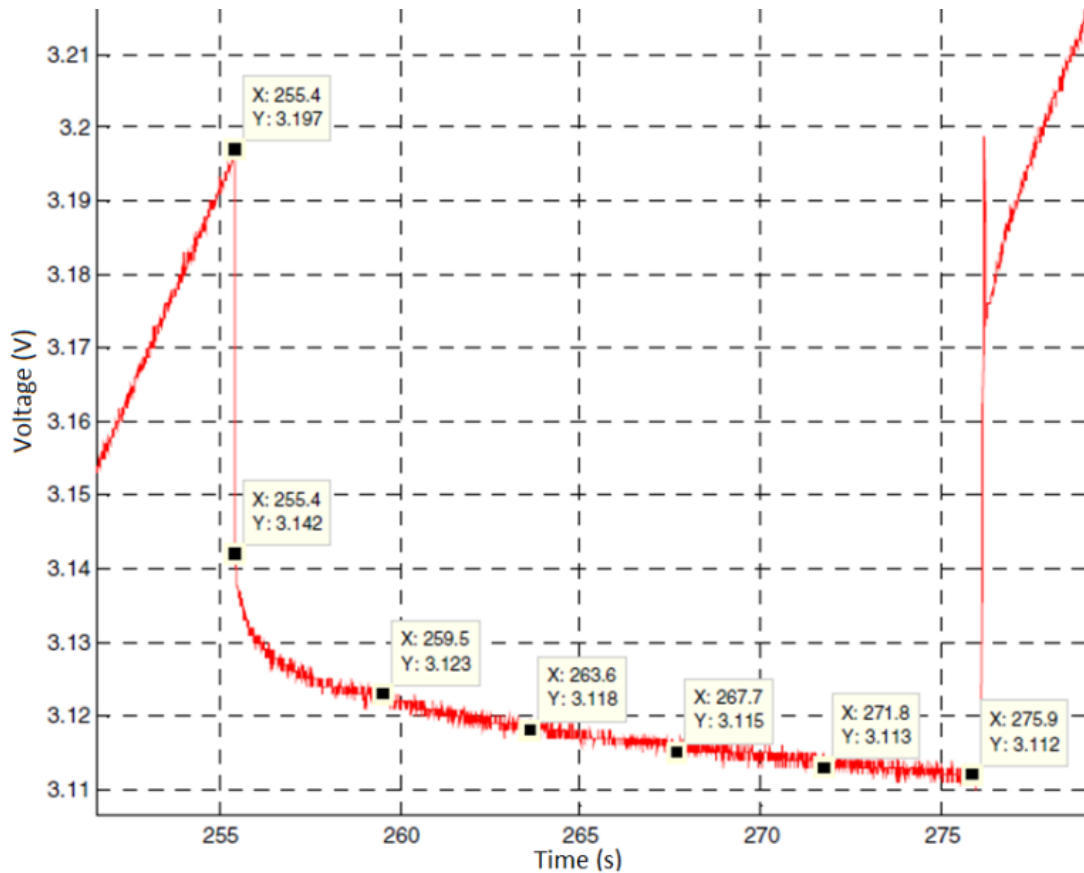
Figure 3.12. Voltage transients exhibited after charging stops in the 10A DC test under 25° C.

The time constant of the decaying voltage section has been observed to be approximately 0.6s. To calculate the value of C_{sa} and R_{sa}, the only parameters with unknown values, two equations are needed. The first one is an equation relating the time constant of an RC circuit to the values of capacitance and resistance. The idea is to charge the ultracapacitor with AC signals and record the voltage across the terminals of the ultracapacitor. AC signals are used here to point out the effect of the RC circuit in series with the internal capacitance while neglecting the effect of that internal capacitance which introduces minimal impedance as it has a huge capacitance compared to the series one. Hence, the other equation is obtained from the AC test, which relates the value of these two unknowns by the tangent of the phase shift between the current signal and the terminal voltage signal. Figure 3.13 shows one of the AC tests with frequency equal to

0.05 Hz. The current signal has been shifted down in order to make the phase shift clear to see and easy to calculate.
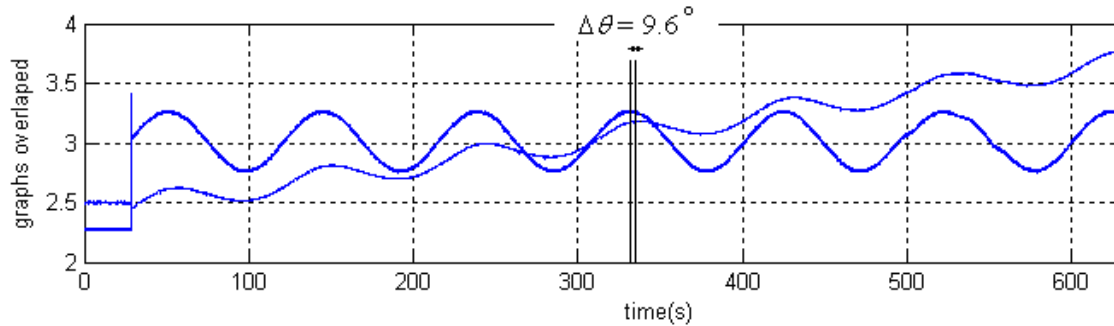
Figure 3.13. Voltage and current waveforms in AC test with f = 0.05 Hz.

The two equations, therefore, are equations 3.6 and 3.7.

$$\tau = C_{sa} \cdot (R_s + R_{sa}) \qquad (3.6)$$

$$\tan(\Delta\theta) = \frac{\omega R_s^2 C_{sa}}{R_s + \omega^2 R_s R_{sa} C_{sa}^2 (R_s + R_{sa})} \qquad (3.7)$$

Solving the above two equations simultaneously results in the values of C_{sa} and R_{sa}. These values were found to be:

$C_{sa} = 30.6\ F$

$R_{sa} = 79.9\ m\Omega$

3.4 State of Charge (SOC) based modeling

In many applications, the SOC-based model of ultracapacitors makes more sense. This type of model is needed where the ultracapacitors are used along with batteries in systems such as peak power shaving applications in utility grid [30]-[31], [43]. Other systems where ultracapacitors significantly increase system performance and efficiency

are automotives systems and pulse power applications [32]-[35], [42], [44], [45]. Generic power electronics systems involving multilevel converters [36] could also require an SOC-based model. References [37]-[40] discuss an interesting application for ultracapacitors where they can be used for power leveling when integrated with batteries to form a hybrid energy storage system. Ultracapacitors can absorb high bursts of energy in short periods of time due to their superior power density, whereas batteries can provide stable energy over longer periods of time due to their high energy density.

To create an SOC-based or rather a battery-based electrical model capable of describing the ultracapacitor behavior, similar test data were used. For this model, it is suggested that the ultracapacitor has an internal SOC-dependent voltage source. This voltage source is denoted as *OCV(SOC)* and is observed at the end of every resting period during a charging or discharging test. To obtain the value of charge, Columbic count was performed according to equation 3.1 discussed earlier.

This Columbic count is one step toward finding a direct relationship between the ultracapacitor open circuit voltage, OCV, and its state of charge, SOC. Figure 3.14 shows the accumulation of charge in the ultracapacitor versus time, while charging under 45˚C at 10A.
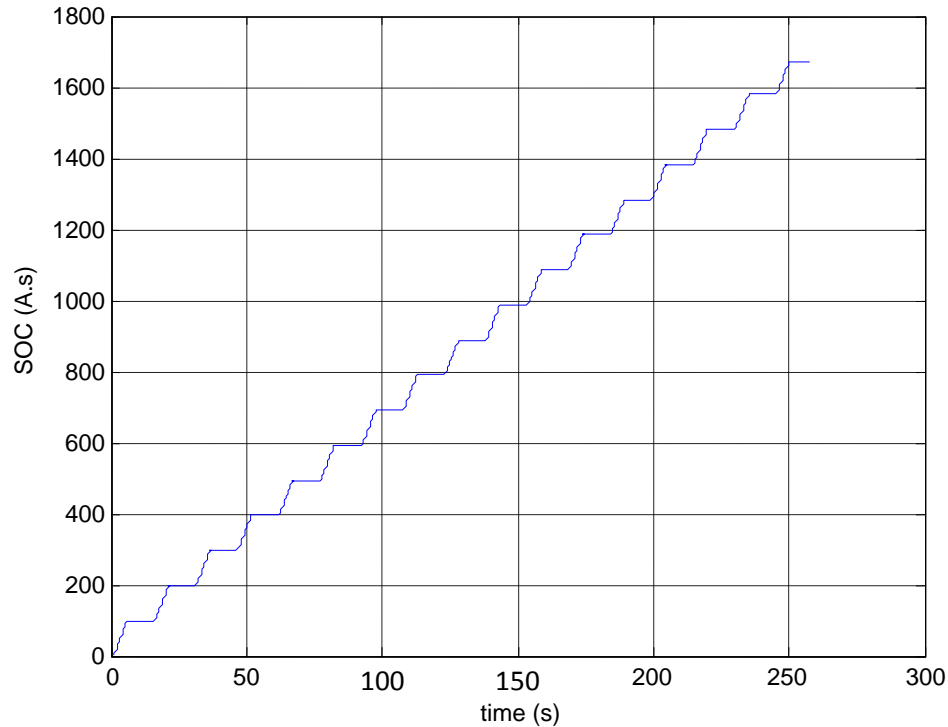
Figure 3.14. Ultracapacitor SOC versus time when charging at 10A.

Figure 3.15 shows the OCV points plotted versus SOC for three different current rates under three different temperatures. This was done to prove the linear relationship between the OCV and the SOC. It is evident that the OCV exhibits a linear relationship with SOC. A linear regression was used to find a relationship relating the two variables. Using the curve fitting tool in Matlab, a line was used to interpolate these data points and happens to have equation 3.7.

$$OCV(SOC) = 0.0156 * SOC + 2.329 \qquad (3.7)$$

Where the SOC value used here is in percentage.
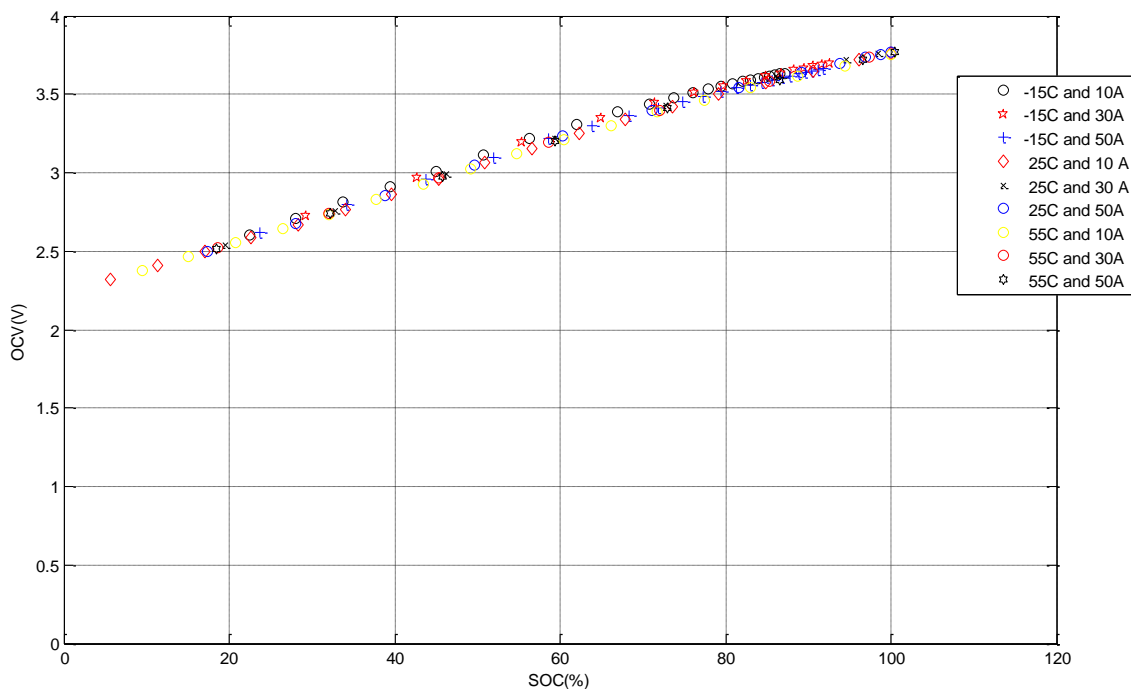
Figure 3.15. OCV vs. SOC at three temperatures and three current ratings.

The self discharging resistance, internal resistance (R_s), series branch capacitance (C_{sa}), and resistance (R_{sa}) do not change in value as these are values based on the same set of tests. The analysis suggests the electrical equivalent circuit shown in Figure 3.16 as SOC-based model for the ultracapacitor.
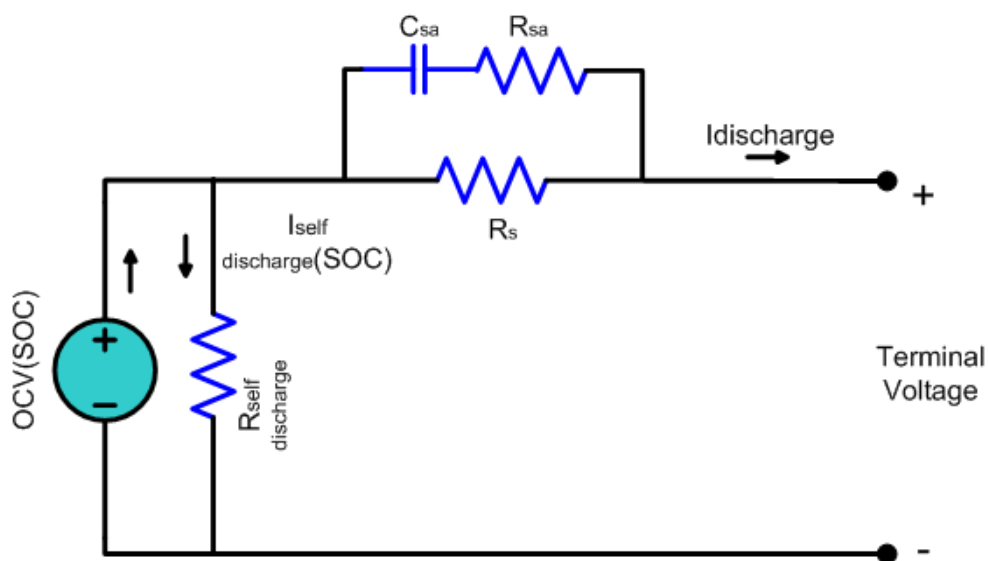
Figure 3.16. The proposed electrical model of the ultracapacitor.

3.5 Model verification and efficiencies

The model developed needs to be tested to make sure it truly represents the ultracapacitor electrical behavior. The model is simulated in Simulink and compared with the actual response of the ultracapacitor for all sets of tests under different temperatures. For model verification, a charging test with a train of current pulses is used. The current is on for ten seconds, and then the ultracapacitor rests for 20 seconds identical to the actual tests. Figure 3.17 shows an example of the actual response versus the simulated response for two tests under 25° C. The blue curve is the test result and the red curve is the results from the model.

The simulated response and the real test response for the 10A test show a nearly perfect match. For the other tests, the simulated response and the real one are very similar yet not exactly the same. However, the voltage increases when the current is on and decreases when the current is off showing the series branch capacitance reacting. There is a small mismatch during transients, but the response shows quick convergence to the real value and accurate end-point values for voltage, which is the most important parameter for control purposes.
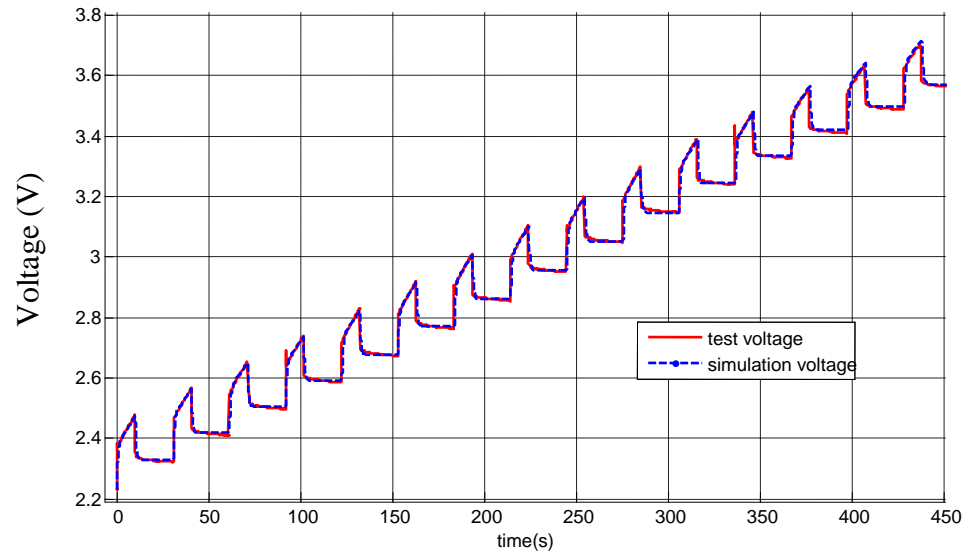
(a)
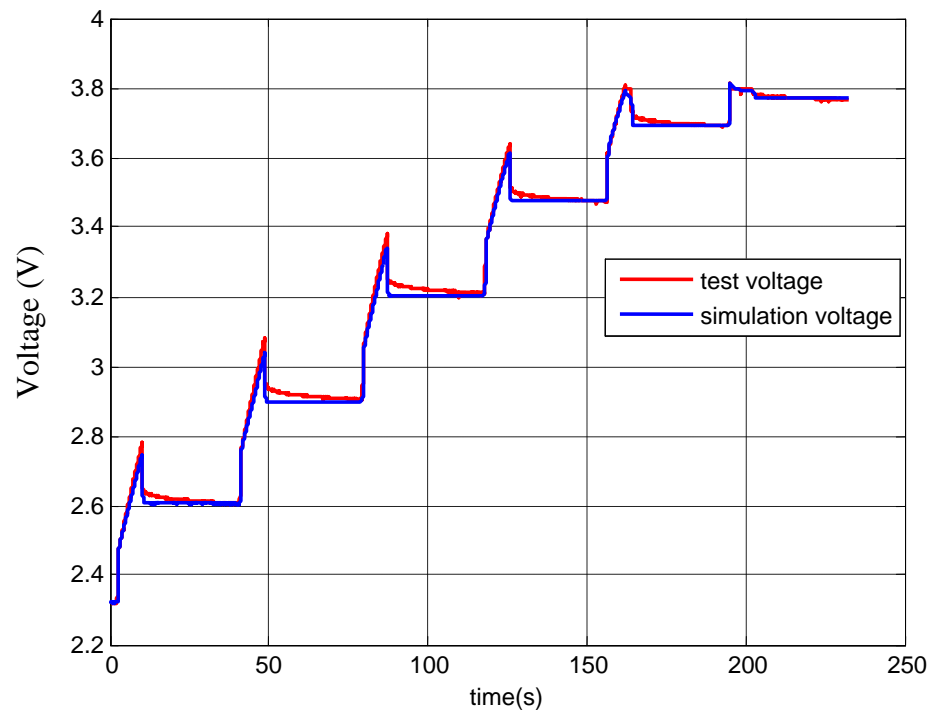
(b)

Figure 3.17. Modeling and test results; (a) 10A DC test under 25°C (b) 40A DC test under 40°C.

Coulombic and Energy efficiencies were also studied for this ultracapacitor. Charging and discharging tests had already been conducted on the ultracapacitor, and it was of interest to investigate the coulombic and energy efficiencies at different current rates and temperatures. This was a simple yet computationally extensive task done by dividing output over input. For the Coulombic efficiency, a Coulombic count was performed for each charging/discharging cycle under all temperatures. The ratio was then taken to determine the efficiency. Energy values were obtained by multiplying the instantaneous value of voltage and the instantaneous value of current and then integrating those products over time. Table 3.4 shows the Coulombic efficiencies, while Table 3.5 shows the energy efficiencies for all tests. In both tables, "I" denotes the DC current in Amps, while "T" denotes temperature in Celsius.

Table 3.4. The Coulombic efficiency for ultracapacitor at various current ratings and temperature.

I\T	-15°	-10°	0°	5°	25°	35°	45°	55°	65°
10	99%	99%	99%	98%	99%	98%	98%	99%	99%
20	99%	99%	99%	99%	98%	99%	99%	98%	99%
30	98%	99%	99%	99%	99%	99%	99%	99%	99%
40	99%	99%	99%	99%	98%	99%	99%	99%	99%
50	99%	99%	99%	99%	99%	98%	99%	99%	99%
60	99%	99%	99%	99%	99%	99%	99%	99%	99%

Table 3.5. The energy efficiency for ultracapacitor at various current ratings and temperature.

I\T	-15°	-10°	0°	5°	25°	35°	45°	55°	65°
10	85%	84%	88%	88%	93%	94%	95%	97%	98%
20	72%	76%	80%	85%	89%	92%	93%	93%	95%
30	67%	72%	77%	80%	89%	91%	92%	93%	94%
40	66%	69%	73%	78%	84%	90%	91%	92%	93%
50	63%	67%	74%	75%	83%	85%	88%	89%	92%
60	66%	67%	68%	73%	83%	85%	87%	88%	89%

One can draw the following fundamental conclusions. Coulombic efficiency, on average, is well around 99% as it is expected due to very large value for the self discharging resistor. Energy efficiency, however, is calculated by taking the product of voltage and current and those values are dramatically affected by temperature and current. It is also evident that energy efficiency has an inverse relationship with the value of current. The higher the ultracapacitor current is, the lower the efficiency is. Regarding temperature, the energy efficiency increases as the temperature increases. Therefore the highest energy efficiency is obtained at high temperatures and low values of current, while the worst performance of the ultracapacitor is obtained under low temperatures and very high currents.

Chapter 4. Lead acid battery modeling

Historically, lead acid batteries are the type of electrochemical energy storage device used in automobiles. In 2013, 99.1% of automobiles utilizing the start-stop technology use lead acid batteries [47]. In 2022, it is expected that 13% of automobiles preinstalled with this technology to have Li-Ion batteries instead as cost drops and energy capacity increases [47]. Lead acid battery modeling can be done in one of three main methods:

1.   Modeling based on equations representing the chemical reactions that take place when the battery is experiencing change of its stored energy due to charging, discharging, or self discharging under ambient conditions such as temperature.

2.   Equivalent electrical circuit that replace the battery with a number of circuit elements.

3.   Neural network.

The first method is the most accurate one; however, it is the most computationally complex and is only used by manufacturers. The third method is the easiest for modeling, but it requires a massive amount of testing to create an adequate set of training data [48]. The second method has a good balance between complexity and accuracy.

Reference 49 discusses battery modeling techniques used for converter-based battery charging and discharging. The ideas, equations, text, and steps presented in Reference 49 to demonstrate these modeling techniques will be followed closely in this chapter with added comments and supporting concepts.

The two main models utilized for battery modeling are mathematical models and electric circuit-based models; hence, the main focus of this chapter will be on these two techniques. Battery system level behavior, such as battery runtime, efficiency, or capacity can be predicted by developing mathematical battery models [50]-[54] based primarily on the Shepherd relation [56]. However, mathematical battery models are limited to specific applications and are only accurate at a percentage between 80% and 95% [55].

Circuit based battery models [55]–[64] are electrical circuit equivalent models that utilize a number of voltage sources, resistors, and capacitors to mimic battery electrical behavior. They are normally used by electrical engineering researchers for simulation purposes in order to simulate the integration of batteries with other electrical circuits and power systems [49]. The model used in simulating a lead acid battery in this study falls under this category. Circuit-based battery models have also undergone constant development from early low accuracy Thevenin-based [56]–[62] and impedance-based [63], [64] battery models to the more accurate runtime-based RC network battery models developed recently [55], [65].

Due to battery model development in the two aforementioned different directions, it becomes important to investigate the relations, differences, and computational complexities using the two modeling approaches. In the sections that follow, this chapter first briefly reviews the electrochemical characteristics that are important for battery model. Then, mathematical battery models including a modified battery model based on Matlab SimPowerSystems will be presented. Typical circuit-based battery models and their relation with the mathematical battery models will be presented next.

A rechargeable battery is comprised of one or more electrochemical cells having the ability to convert stored chemical energy into electrical energy during discharging and convert electrical energy into chemical energy during charging [49].

An electrochemical cell is a device used for electric energy generation or storage. It consists of a positive electrode and a negative electrodes separated by a separator material immersed in an electrolyte as shown in figure 4.1. The electrolyte allows the conduction of ions between the two electrodes, but is itself an insulator. The positive and negative electrodes are also immersed in the electrolyte and the reacting substances are stored within the electrodes and the electrolyte. The chemical reactions associated with the energy conversion take place at the two electrodes. During discharging, the negative electrode contains the substance that is oxidized, while the positive electrode contains the oxidizing substance that is reduced. Electrons go through the load connected across the cell terminals effectively doing useful work. When the battery is charged, the chemical reactions are reversed and an amount of energy from an external power source has to be supplied to the cell. The discharging and charging processes in an electrochemical cell are shown in figures 4.1a and 4.1b respectively [49].

(a)   (b)
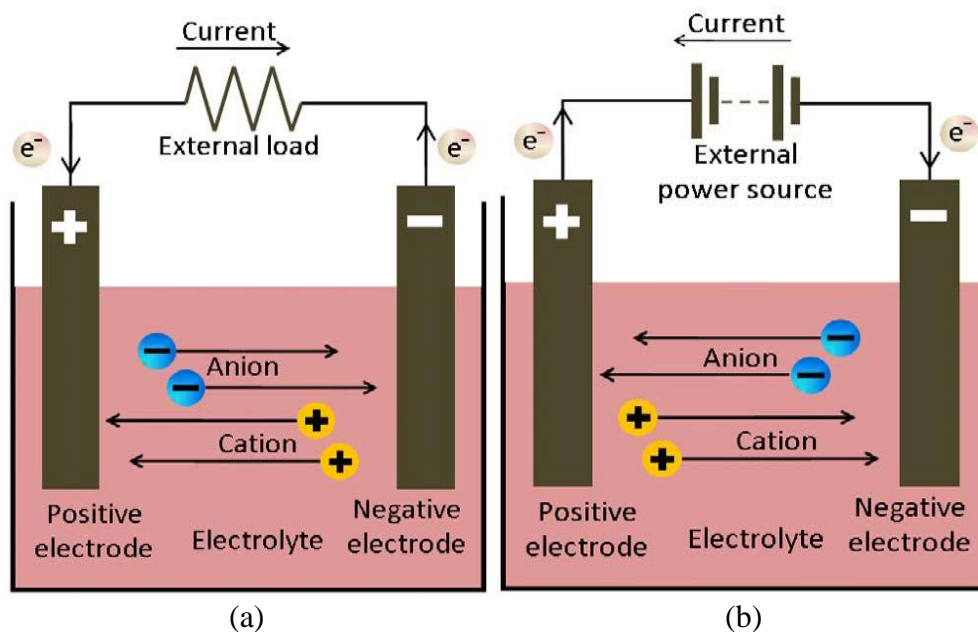
Figure 4.1. Electrochemical cell structure. a) Discharging. b) Charging [49].

Reference 49 explains what happens to cell voltage during both cell operating conditions as follows. The current in a battery is established as a result of electrons transferring from one electrode to the other. When the current flow through a cell is equal to zero, the difference between the positive and negative electrode potentials yields the cell's Open Circuit Voltage (OCV). While current in a cell is flowing, the reacting substances transport is required from one electrode surface to the other. As a result, the voltage when current is flowing differs from the OCV. The difference comes from:

1. An overvoltage at the electrodes caused by electrochemical reactions and concentration deviations resulting from the mass transport.

2. Ohmic voltage drops caused by the electrons and ions flowing in the conducting parts such as the electrolyte, electrodes, and active masses. The sum of electronic and ionic currents, called polarization, is responsible for a decreased cell voltage (V_{dis}) during discharging and an increased cell voltage (V_{ch}) during charging as shown in equations 4.1 and 4.2 [49].

$$V_{dis} = E_0 - V_{op+} - V_{op-} - iR_{pol} \qquad (4.1)$$

$$V_{ch} = E_0 + V_{op+} + V_{op-} + iR_{pol} \qquad (4.2)$$

where V_{op+} and V_{op-} are the overvoltages at the positive and negative electrodes, respectively, and R_{pol} is the polarization resistance. Due to the polarization effect, the battery voltage, when current is flowing, differs from the OCV depending on the state of charge of the battery.

Reference 49 discusses other important factors affecting battery performance and models. These include: battery capacity, state-of-charge (SOC), rate of charge and discharge, temperature, and age. The battery capacity relates to the amount of energy that can be extracted from the battery under certain conditions such as rate of discharge, and is determined by the mass of active material contained in the battery when it is fully charged. The SOC is defined as the fraction of full capacity that is available for further discharge at any operating point. The OCV of a battery is normally a function of the SOC due to the polarization impact. Charging and discharging rates as well as ambient temperature are the main factors affecting the rated battery capacity. According to Peukert's equation, if the battery is being discharged at a high rate, the amount of energy that can be extracted from the battery is reduced. Consequently, effective modeling using Peukert's relation is particularly important for design and analysis of power converter controlled battery charging and discharging. The age and history of a battery also have impacts on the capacity of a battery. Even when following manufacturers' depth of discharge (DOD) specifications, the battery capacity only stays at the rated capacity for a limited number of charge/discharge cycles. If the battery has been taken below its maximum DOD during its usage, battery capacity may be prematurely reduced. As for

temperature effect, at higher temperatures, the battery capacity is usually higher than it is at lower temperatures. But, intentionally elevating battery temperature is not an effective method to increase battery capacity as this also decreases battery lifetime [49].

4.1 Mathematical Models:

A detailed mathematical battery model normally includes several submodels of which the most vital submodel from an electrical standpoint is the voltage-current model, which describes how the terminal voltage of a battery changes with current rate. The most famous known voltage-current model for constant-current discharge is the Shepherd model [52], [54]:

$$V_{batt} = E_0 - K\left[\frac{Q}{Q-it}\right]i - R_0i \qquad (4.3)$$

where the first term E_0 represents the OCV of a battery at full capacity, K is the polarization resistance coefficient (Ω), Q is battery capacity (Ahr), i is battery current (A), R is internal resistance and $it = \int i \cdot dt$ (Ahr). In equation 4.3, the second term is associated with the polarization ohmic voltage loss, and the last term stands for the internal resistance loss. Equation 4.3 can be presented in equation 4.4 using SOC, which indicates that the polarization ohmic voltage is inversely proportional to SOC [49].

$$V_{batt} = E_0 - \frac{K}{SOC}i - R_0i \qquad (4.4)$$

Many recent voltage-current models are more complicated than the Shepherd's relation [50], [53], [54]. Those models typically start with a relation similar to that of Shepherd, and then add and modify terms to try to improve the relation fit to both measured charge and discharge curves, and relax the assumptions behind the Shepherd model [49].
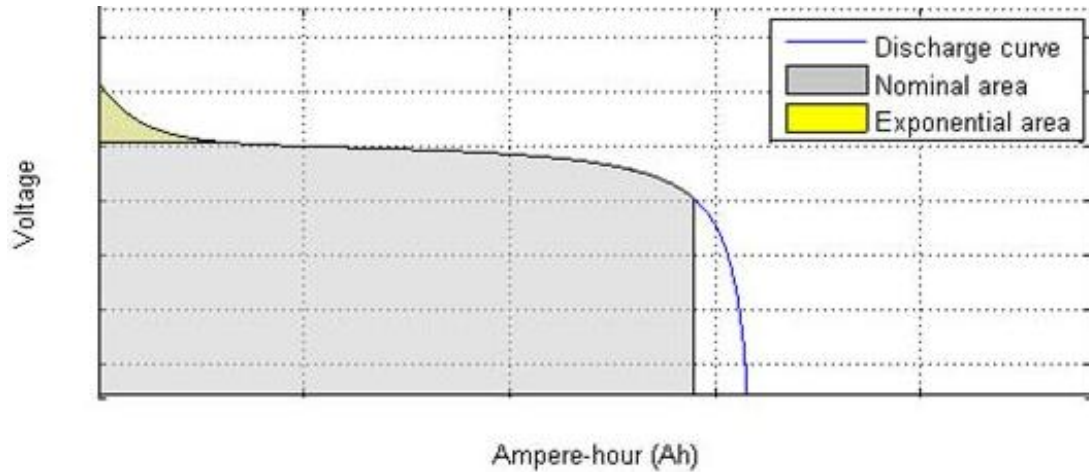
Figure 4.2. A typical electrochemical cell discharge curve [49].

Equations 4.5 and 4.6 present modified battery models for discharge and charge of lead-acid batteries, respectively, based on the Shepherd relation and SimPowerSystems battery model

$$V_{dis} = E_0 - K_{dr} \frac{Q}{Q - it} i^* - R_0 i - K_{dv} \frac{Q}{Q - it} it + Exp(t) \qquad (4.5)$$

$$V_{ch} = E_0 - K_{cr} \frac{Q}{\lambda Q + it} i^* - R_0 i - K_{cv} \frac{Q}{Q - it} it + Exp(t) \qquad (4.6)$$

where K_{dr} is the polarization resistance coefficient (Ω) and K_{dv} is the polarization overvoltage coefficient (V/Ah). As for the polarization ohmic voltage drop, the second term in equations 4.5 and 4.6 is different for charge and discharge and is modified by using a filtered battery current i^* to simulate actual slow voltage dynamic behavior for a step current response. The coefficient λ in equation 4.6 is to account for the shift of polarization resistance during battery charging. The internal resistance in the third term has different values for charge and discharge. A fourth term concerning the polarization overvoltage is added. This term together with E_0 or E_0 can better represent the nonlinear OCV relation with the SOC. The last term $Exp(t)$ represents an exponential dynamic voltage shown in figure 4.2 to reflect a non-linear hysteresis phenomenon between

discharge and charge. For lead-acid batteries, *Exp(t)* is determined by equation 4.7, where u(t) = 0 for discharge and u(t) = 1 for charge. Equations 4.5 and 4.6 can be rewritten by using SOC. For example, in terms of SOC, equation 4.5 becomes equation 4.8, which shows that as SOC decreases, the voltage drop, caused by polarization ohmic and overvoltage impacts, increases under battery discharge mode. Also, according to equation 4.8, the polarization overvoltage impact is insignificant in the vicinity of the full battery capacity but becomes a more dominant component as the SOC drops [49].

$$Exp(t) = Bi\big(Exp(t) + Au(t)\big) \qquad (4.7)$$

$$V_{dis} = E_0 - K_{dr}\frac{1}{SOC}i^* - R_0 i - K_{dv}\left(\frac{1}{SOC} - 1\right) + Exp(t) \qquad (4.8)$$

Equations 4.5 and 4.6 suffer from the following modeling limitations:

1. Battery capacity (Q) does not change with current rate

2. Temperature does not affect model behavior

3. Battery aging is not considered

4. Effect of self discharging is not considered.

Those factors can be considered in a more complete mathematical battery model as shown in the flowchart in Figure 4.3, in which battery parameters change during the lifetime of the battery to provide an aging profile and degradation of battery performance affected by many other factors. The change in parameters is calculated at every simulation time step. For example, the SOC can be calculated more accurately at each time step based on equation 4.9, which includes the impact of gassing current i_{gas} and the self discharging current i_{sd}. If battery capacity falls below the threshold capacity, the end of life of the battery is signaled [49].

$$SOC = SOC_{init} - \frac{1}{Q}\int_0^t \left(i - \max\left(i_{gas}, i_{sd}\right)\right) d\tau \qquad (4.9)$$
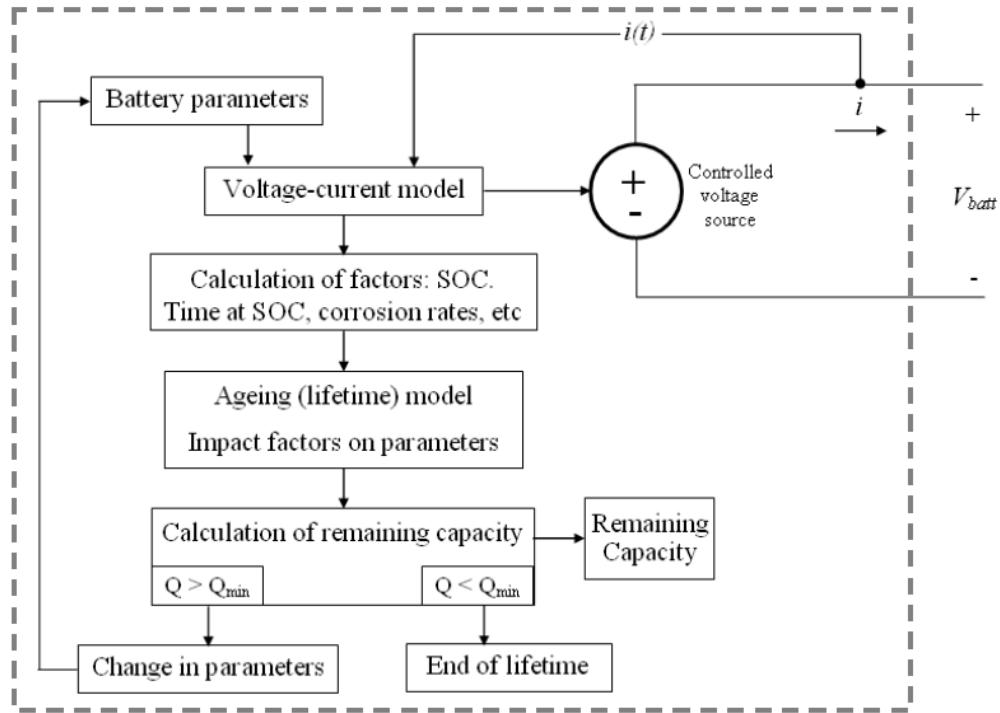
Figure 4.3. Flowchart of mathematical battery model [49].

4.2 Circuit-based battery models

Circuit-based battery models utilize a combination of voltage and current sources, resistors, and capacitors in an electric circuit to model battery behavior. Most electrical models fall under three basic categories: Thevenin-based [56]–[62], impedance-based [63], [64], and runtime-based models [55], [65]. Normally, it is more complicated to change battery parameters for different conditions and states of the battery. In addition, to account for variations between charge and discharge states, two opposing diodes have to be used for each circuit element, making circuit-based battery models more complex [49].

In its most basic form, a Thevenin-based model [56]–[62], shown in Fig. 4.4a, consists of a voltage source (V_{oc}(SOC)) in series with an internal resistor, R_0, and a

parallel combination of a capacitor and resistor to predict battery response to transient loads at a particular SOC, by assuming a constant open-circuit voltage, V_{oc}(SOC). Thus, this model is unable to properly reflect the SOC influence on the battery behavior [49].

Impedance-based models, shown in figure 4.4b, employ the method of electrochemical impedance spectroscopy to obtain an AC equivalent impedance model in the frequency domain, and then use a complicated equivalent network, Z_{ac}, to fit the impedance spectra [55], [65]. The fitting process is complex. In addition, impedance-based models only work for a fixed SOC and temperature settings [63] and therefore cannot predict DC response or battery runtime. Runtime-based models [55], [65] use a complex circuit network to simulate battery runtime and DC voltage response [49].

Figure 4.4c shows a recent runtime-based battery model [65]. On the left hand side of the model, a capacitor (C_Q) having the value of battery capacity and a current-controlled current source describe how the battery SOC, represented by V_{SOC}, varies with the battery current. On the right hand side, the RC networks, similar to that used in the Thevenin-based model, simulate the relation between the battery current and terminal voltage [49].
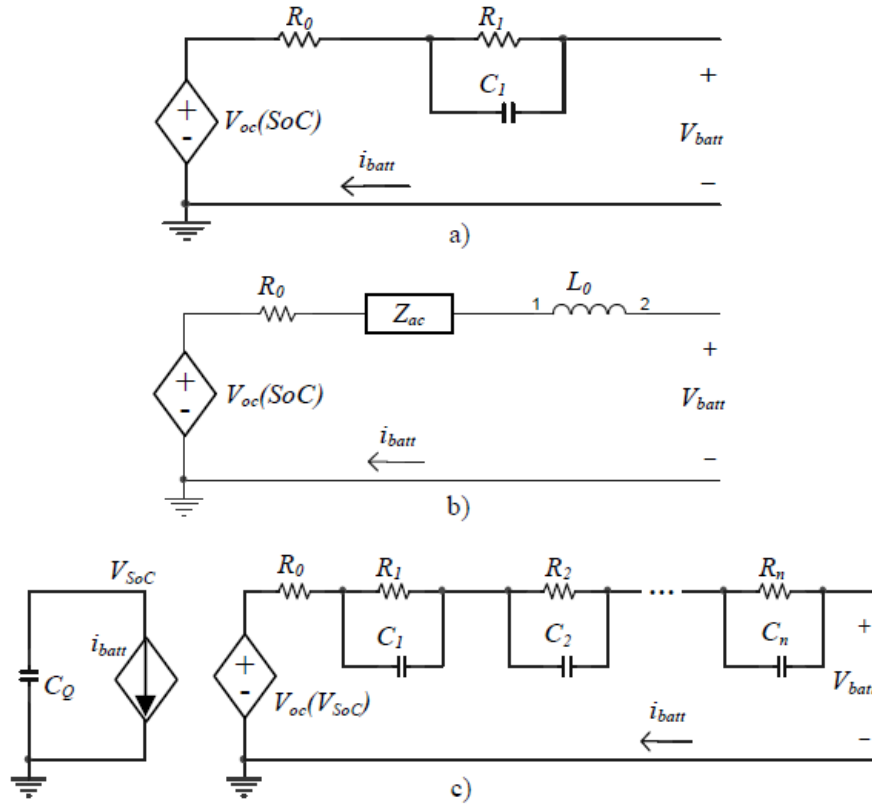
Figure 4.4. Electric circuit based battery models [49].

The relation between the mathematical and circuit-based battery models can be evaluated through a comparison study of battery discharge between figure 4.4c and equation 4.8 according to the following points taken from reference 49:

1.   The term $R_0 i_{batt}$ is equivalent to the term $R_0 i_d$ in equation 4.7, which represents the internal resistance voltage loss in circuit-based and mathematical battery models, respectively.

2.   For the RC networks of the runtime-based battery model, assuming that the voltage applied to the ith RC network is v_i, then, in the s domain after applying Laplace transform, the relation between the voltage v_i and the battery current passing through the ith RC network is given by equation 4.10 according to which the voltage v_i can be interpreted as the voltage drop of the low-pass filtered battery current over the resistor R_i

of the RC network, in which the cutoff frequency of the low-pass filter is $1/(R_iC_i)$. Thus, the combined effect of all the RC networks is actually equivalent to a resultant low-pass filter applied to a resultant RC network resistance. From this point of view, the low-pass filtered current in the circuit-based model is equivalent to i^* in equation 4.8, and the voltage drop over the RC networks together is equivalent to the term $K_{dr}i^*/SOC$ in equation 4.8 to reflect the polarization ohmic voltage drop. But, the term $K_{dr}i^*/SOC$ in the mathematical based model is a function of SOC, which implies that the values of R_i and C_i of the RC networks in the circuit-based model should also be functions of SOC, which is consistent with results shown in [55] and [65].

$$v_i(s) = R_i \frac{\frac{1}{R_iC_i}}{s + \frac{1}{R_iC_i}} i_{batt}(s) \qquad (4.10)$$

3. In the runtime based battery model, the battery OCV is modeled via a voltage-controlled voltage source, in which voltage V_{SOC} simulates the battery SOC. A comparison between the open-circuit voltage $V_{oc}(V_{SOC})$ in the circuit-based battery model and equation 4.8 indicates that $V_{oc}(V_{SOC})$ should be equivalent to $E_0 - K_{dv}(1/SOC-1)$. As a result, $V_{oc}(V_{SOC})$ in the circuit-based model should be a function of SOC.

4. It is normally more complex to model electrochemical phenomenon associated with the charging or discharging regimes, the age and past history of the battery, and temperature effect in the circuit-based battery model. However, such issues are very important for research of converter controlled management of batteries that are connected to the grid.

Chapter 5. Hybrid energy storage system design

5.1 Proposed ESS benefits and comparison to other solutions

The proposed Hybrid ESS in this dissertation offers the following benefits and advantages over the other solutions:

1.   Simple design

2.   Compact

3.   Control free

4.   Easy to control sharing of cranking current

Other solutions include:

1.   Enlarged Lead Acid battery

2.   Lead acid battery connected to a single LiC via a DC-DC converter

The enlarged lead acid battery occupies a bigger volume under the hood of automobiles where space is extremely scares. While the DC-DC converter in the second alternative saves three LiC's, it adds complications to the design, losses in the converter, and requires large output capacitor to keep the battery terminal voltage from sagging during cranking, and it requires a large inductor to be able to provide the very large cranking current.

5.2 Hybrid ESS modeling

The proposed ESS is constructed from an ultracapacitor module connected in parallel with a lead acid battery. The ultracapacitor module is comprised of four Li-ion ultracapacitors connected in series to meet the voltage requirement of a single automobile lead acid battery of 12 Volts. The use of Li-ion ultracapacitors requires that they maintain a terminal voltage having a minimum of 2.2 Volts and a maximum of 3.8 Volts each. The

nominal voltage for each ultracapacitor is 3 Volts. The voltage limits for the ultracapacitor module matches the minimum voltage requirement across the lead acid battery, its nominal voltage of 12 Volts, and the alternator average charging voltage of 14.4 Volts. This is one possibility out of four possible ways an automobile can have an Energy Storage System (ESS).
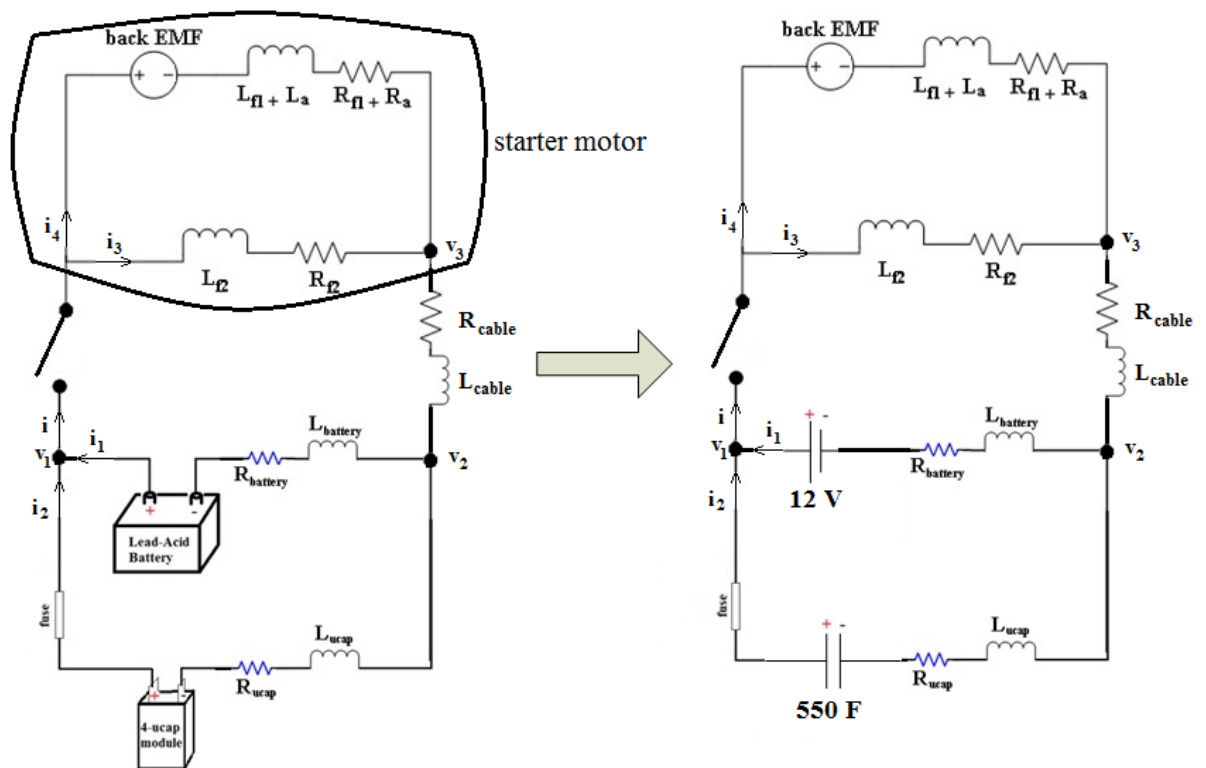
Figure 5.1. Engine cranking circuitry.

The complete vehicle cranking circuitry is shown in figure 5.1 where the starter motor is a compound DC motor and the battery is connected in parallel with the ultracapacitor module. The lead acid battery model is simplified to a DC power supply of constant voltage of 12 Volts while the ultracapacitor module model is simplified to a capacitor having a capacitance value of 550 F, which comes from the equivalent capacitance value of four 2200-F capacitors in series. This simplification is not valid for

the entire operable region of both the lead acid battery and ultracapacitor. However, for the application under study, it is an excellent assumption as the time interval during which cranking takes place is not longer than 50 ms not allowing the OCV of the battery or the ultracapacitor module to experience any considerable drop.

The instantaneous power curve is obtained by taking the instantaneous product of voltage and current during the two second period at which the cranking test was conducted. Running a Riemann sum on the power curve yields the energy curve. The maximum power required during cranking is a little over 4kW and the energy required for cranking is about 1.7 kJ. One car used for running cranking tests is a 2002 Toyota Solara with a 6-cylinder, 3.0 L engine. The power is chosen to have a negative sign when the battery is being discharged and positive sign when being charged. The objective of the mathematical modeling is to derive an expression of the battery current as a function of the cranking circuit parameters. The circuit shown in figure 5.1 represents the car circuitry. The circuit parameters are:

L_{cap} : ultracapacitor branch inductance

R_{cap} : ultracapacitor branch resistance

$L_{battery} = L_{bat}$: battery branch inductance

$R_{battery} = R_{bat}$: battery branch resistance

L_{f2} : compound DC machine field winding inductance

R_{f2} : compound DC machine field winding resistance

L_a : compound DC machine armature winding inductance

L_{f1}: compound DC machine armature winding field inductance

R_a: compound DC machine armature winding resistance

R_{f1}: compound DC machine armature winding field resistance

Using the circuit in figure 5.1, the three equations obtained after applying KVL on three loops are given by equations 5.1-5.3

$$i_3 R_{f2} + L_{f2}\frac{di_3}{dt} + iR_{cable} + L_{cable}\frac{di}{dt} = V_{bat} - i_1 R_{Bat} - L_{Bat}\frac{di_1}{dt} \quad (5.1)$$

$$V_{cap} - i_2 R_{cap} - L_{cap}\frac{di_2}{dt} = V_{bat} - i_1 R_{Bat} - L_{Bat}\frac{di_1}{dt} \quad (5.2)$$

$$i_3 R_{f2} + L_{f2}\frac{di_3}{dt} = e_a + i_4(R_{f1} + R_a) + (L_a + L_{f1})\frac{di_4}{dt} \quad (5.3)$$

Applying Laplace transform to equations 5.1-5.3, and replacing i₃ by its equivalent from equation 5.4, equations 5.5-5.7 can be written as follows:

i₃ = i₁ + i₂ − i₄   (5.4)

$$I_1(s)R_{f2} + I_2(s)R_{f2} - I_4(s)R_{f2} + sL_{f2}I_1(s) + sL_{f2}I_2(s) - sL_{f2}I_4(s) + R_{cable}I_1(s)$$
$$+ R_{cable}I_2(s) + sL_{cable}I_1(s) + sL_{cable}I_2(s) = \frac{V_{bat}}{s} - I_1(s)R_{Bat} - sI_1(s)L_{Bat} \quad (5.5)$$

$$\frac{I_2(s)}{sC} - I_2(s)R_{cap} - sI_2(s)L_{cap} = \frac{V_{bat}}{s} - I_1(s)R_{Bat} - sI_1(s)L_{Bat} \quad (5.6)$$

$$I_1(s)R_{f2} + I_2(s)R_{f2} - I_4(s)R_{f2} + sL_{f2}I_1(s) + sL_{f2}I_2(s) - sL_{f2}I_4(s)$$
$$= E_a(s) + I_4(s)R_{f1} + I_4(s)R_a + sL_a I_4(s) + sL_{f1}I_4(s) \quad (5.7)$$

Rearranging terms, the equation that relates the battery current to the rest of the circuit parameters and variables is given by equation 5.8.

$$I_1(s) = [\frac{B}{A}][E_a(s) - \frac{sL_2 V_{bat} + R_2 V_{bat}}{+ sR_{f2}}] \quad (5.8)$$

where:

$$A = s^5[L_{f2}^2 L_{cap} + L_{f2}^2 L_{bat} V_{bat} - L_2 L_1 L_{cap} - L_2 L_{f2} L_{bat} - L_2 L_{bat} L_{cable}]$$

$$+ s^4[2L_{f2} L_{cap} R_{f2} + L_{f2}^2 R_{cap} + L_{f2}^2 R_{bat} V_{bat} + 2L_{f2} R_{f2} V_{bat} L_{bat}$$

$$- L_2 L_1 R_{cap} - L_2 L_{cap} R_1 - R_2 L_1 L_{cap} - L_2 L_{f2} R_{bat} - R_2 L_{cable} L_{bat}$$

$$- R_2 L_{f2} L_{bat} - L_2 R_{cable} L_{bat} - L_2 L_{cable} R_{bat} - L_2 R_2 L_{bat}]$$

$$+ s^3[-\frac{L_{f2}^2}{C} - L_{f2}^2 V_{bat} + 2L_{f2} R_{f2} L_{f2} V_{bat} R_{bat} + R_{f2}^2 V_{bat} L_{bat}$$

$$+ L_2 L_{f2} V_{bat} - R_2 L_2 R_{bat} + L_2 L_{cable} V_{bat} + L_{cap} R_{f2}^2 + \frac{L_2 L_1}{C}$$

$$- L_2 R_1 R_{cap} - R_2 L_1 R_{cap} - R_2 R_1 L_{cap} - L_2 R_{cable} R_{bat} - R_2 L_{f2} R_{bat}$$

$$- R_2 L_{cable} R_{bat} - R_{cable} R_2 L_{bat} - R_{cable} R_2 L_{bat}]$$

$$+ s^2[-2L_{f2} R_{f2} V_{bat} - 2\frac{L_{f2} R_{f2}}{C} + R_{f2}^2 R_{cap} + R_{f2}^2 V_{bat} R_{bat}$$

$$+ \frac{L_2 R_1}{C} + \frac{R_2 L_1}{C} - R_2 R_1 R_{cap} - R_{f2} R_2 R_{bat} - R_{cable} R_2 R_{bat}$$

$$+ L_2 R_2 V_{bat} + R_{cable} L_2 V_{bat} + R_{f2} L_{f2} V_{bat} + R_2 L_{cable} V_{bat}]$$

$$+ s[R_{f2} R_2 V_{bat} + R_{cable} R_2 V_{bat} + \frac{R_2 R_1}{C} - R_{f2}^2 V_{bat} - \frac{R_{f2}^2}{C}] \qquad (5.9)$$

$$B = s^4 L_{f2} L_{cap} + s^3 (R_{f2} L_{cap} + L_{f2} R_{cap}) + s^2 (R_{f2} R_{cap} - \frac{L_{f2}}{C}) - s\frac{s R_{f2}}{C} \qquad (5.10)$$

$$L_1 = L_{f2} + L_{cable} + L_{bat} \qquad (5.11)$$

$$L_2 = L_{f2} + L_a + L_{f1} \qquad (5.12)$$

$$R_1 = R_{cable} + R_{f2} + R_{bat} \qquad (5.13)$$

$$R_2 = R_{f2} + R_{f1} + R_a \qquad (5.14)$$

Equation 5.8 is the main equation for which this mathematical analysis was performed. For the sake of making equation 5.8 look compact, terms A and B were defined in equations 5.9 and 5.10 respectively. This was also the same reason equations 5.11-5.14 were introduced defining L_1, L_2, R_1, R_2.

5.3 Cranking current sharing control

One simple yet extremely effective technique to control the cranking current shared by the Li-ion ultracapacitor module and the lead acid battery is to control the branch resistances. Mere varying the cable length for the battery or ultracapacitor module changes the current sharing drastically. This was tested experimentally and simulated to see the effect of branch resistance. In figure 5.2, the maximum cranking current is simulated for a battery branch resistance of 7 mΩ while the ultracapacitor branch resistance is allowed to vary. The two current curves should be added together to get the total maximum cranking current.
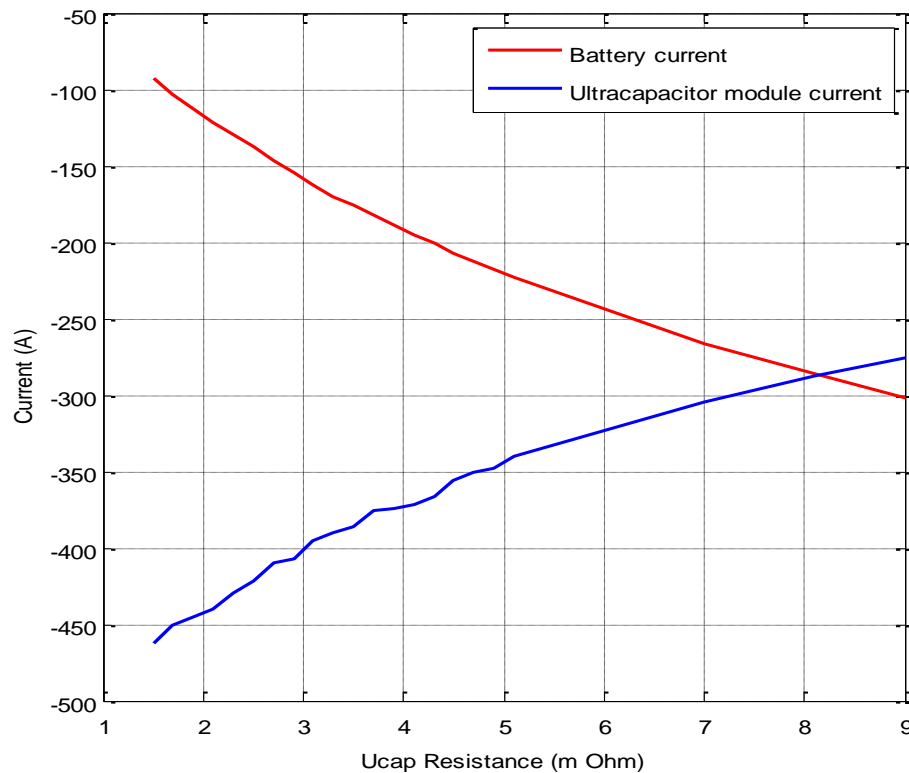
Figure 5.2. Cranking current sharing as a function of ultracapacitor branch resistance.

It is interesting to see that an increase of a few mΩ of ultracapacitor branch resistance can result in a massive increase of battery branch cranking current contribution

and a massive decrease of the battery branch contribution. Figure 5.3 shows the opposite case where the ultracapacitor branch resistance is kept constant at 9 mΩ while the battery branch resistance is allowed to vary. In figure 5.3, the red curve is represents the battery current while the blue curve represents the ultracapacitor module current Similar observations can be made especially the fact the maximum cranking current is super sensitive to the branch resistance value.
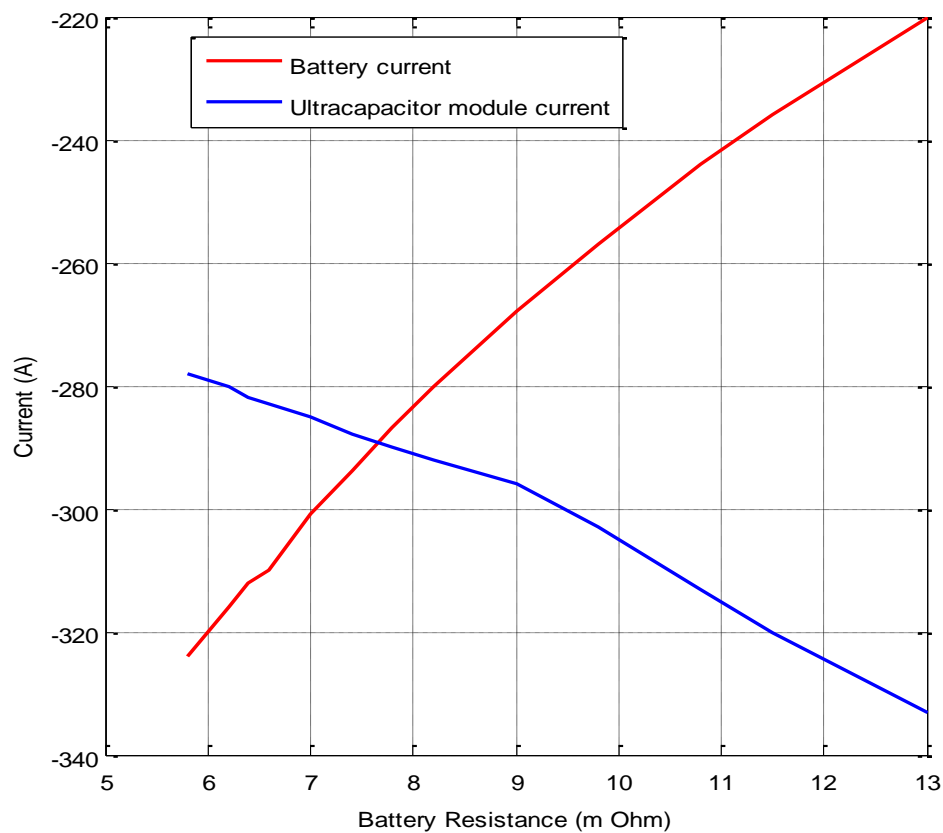
Figure 5.3. Cranking current sharing as a function of battery branch resistance.

Chapter 6. Lead acid aging analysis

The cranking profile presented in reference 66 is a perfect example of a pulsed power profile. Any energy storage system having to provide such power for a short period of time experiences stress leading to its gradual aging. In this chapter, a number of parameters designed to quantify the stress a battery goes through during engine cranking as well as quantify the benefits gained from combining a battery with an ultracapacitor module in a hybrid ESS will be presented. In a study done by JSR Micro, five parameters were introduced to assess the overall performance of such a hybrid ESS considering system cost and performance [66]. The pulsed power profile on which the parameters are derived is shown in figure 6.1.
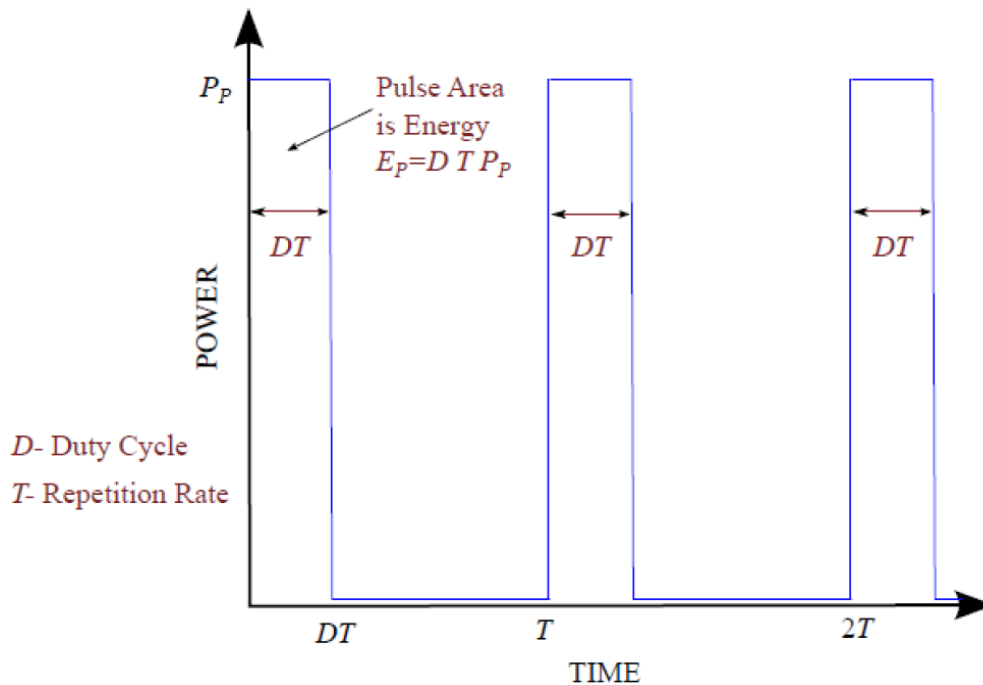
Figure 6.1. Pulsed power profile defined in the JSR Micro study [66].

In this study, a basic energy storage system model is used. In particular, a lead acid battery equivalent circuit model is used to derive the equations that define the energy, capacity, and power required during the pulse period. Also, all aging parameters

are also defined based on this equivalent circuit model and simplified pulsed power profile mentioned earlier. The lead acid equivalent circuit used in this study is provided in figure 6.2.
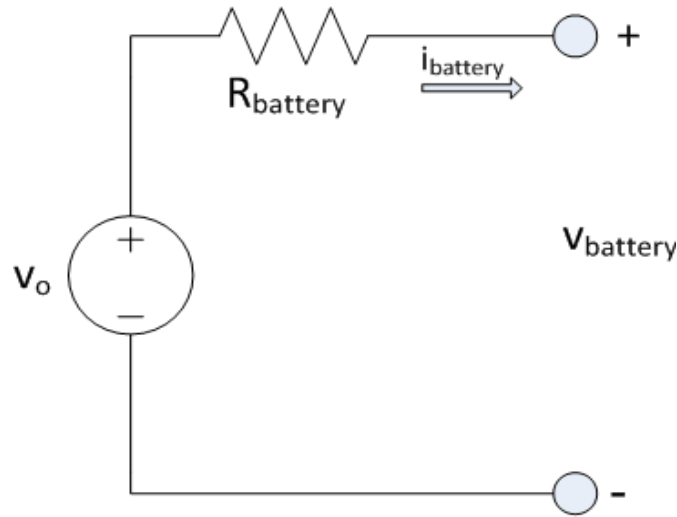
Figure 6.2. Lead acid battery electrical circuit equivalent model.

The amount of charge provided by the battery during a single pulsed power interval is given by equation 6.1:

$$\Delta Q_C^{pulsed}[n] = \int_{(n-1)T}^{(n-1+D)T} i_{battery}^{pulsed}(\tau)d\tau = \int_{(n-1)T}^{(n-1+D)T} \frac{P_P}{v_{battery}^{pulsed}[n]}d\tau = \frac{D \cdot T \cdot P_P}{v_{battery}^{pulsed}[n]}$$

$$= i_{battery}^{pulsed}[n] \cdot D \cdot T = \frac{2 \cdot D \cdot T \cdot P_P}{v_o[n](1+\sqrt{1-\frac{4P_P R_{battery}[n]}{(v_o[n])^2}})} \qquad (6.1)$$

The five parameters will be defined next. These parameters are characteristic; i.e. they characterize the battery on different levels, they are generalized for pulsed power profiles so that they apply to a wide range of pulsed power applications not exclusive to the profile on which the aging study is based, and they are normalized parameters having a value that ranges between zero and one.

A. Battery Loading Factor (BLF)

This parameter provides a measure of the battery loading. Since loading is directly affected by the amount of current going through the battery especially during discharging, one possible equation that can be used to construct this parameter would be given by equation 6.2

$$x(t) = \frac{2R_{battery}(t)i_{battery}(t)}{v_o(t)} \qquad (6.2)$$

x(t) shows direct proportionality with the battery current; however, it does not show the peak power of the pulsed power profile. This equation can be used towards defining the BLF by defining the parameter expressed by equation 6.3 and 6.4

$$\lambda(t) = 2x(t) - x(t)^2$$

$$= \frac{4R_{battery}(t)i_{battery}(t)}{v_o(t)} - \left(\frac{2R_{battery}(t)i_{battery}(t)}{v_o(t)}\right)^2 \qquad (6.3)$$

$$\rho[n] = \frac{4R_{battery}[n]i_{battery}[n]}{v_o[n]^2}\left(v_o[n] - R_{battery}[n]i_{battery}[n]\right)$$

$$= \frac{4R_{battery}[n]i_{battery}[n]}{v_o[n]^2} v_{battery}[n] = \frac{4R_{battery}[n]P_P}{v_o[n]^2} \qquad (6.4)$$

ρ satisfies all of the properties that the aging parameters are to have; it is unitless, normalized, monotonically increasing function of the peak power demand. ρ is therefore elected to be the BLF.

B.   Battery Stress Factor (BSF)

Batteries experience stress when being charged or discharged at a much higher rate than the rated current. The current passing through the battery causes thermal stress. A parameter showing the stress undergone by the battery is defined as the ratio of energy loss as heat versus energy deliverable to the load; this parameter is given in equation 6.5

$$\alpha(t) = \frac{\int_0^t R_{battery}(\tau) \left(i_{battery}(\tau)\right)^2 d\tau}{\int_0^t v_{battery}(\tau)|i_L(\tau)|d\tau}$$

$$= \frac{R_{battery}[n]P_P}{\left(v_{battery}^{pulsed}[n]\right)^2} = \frac{\rho[n]}{\left(1+\sqrt{1-\rho[n]}\right)^2} \tag{6.5}$$

Equation 6.5 shows the relationship between BSF and BLF, which is shown in figure
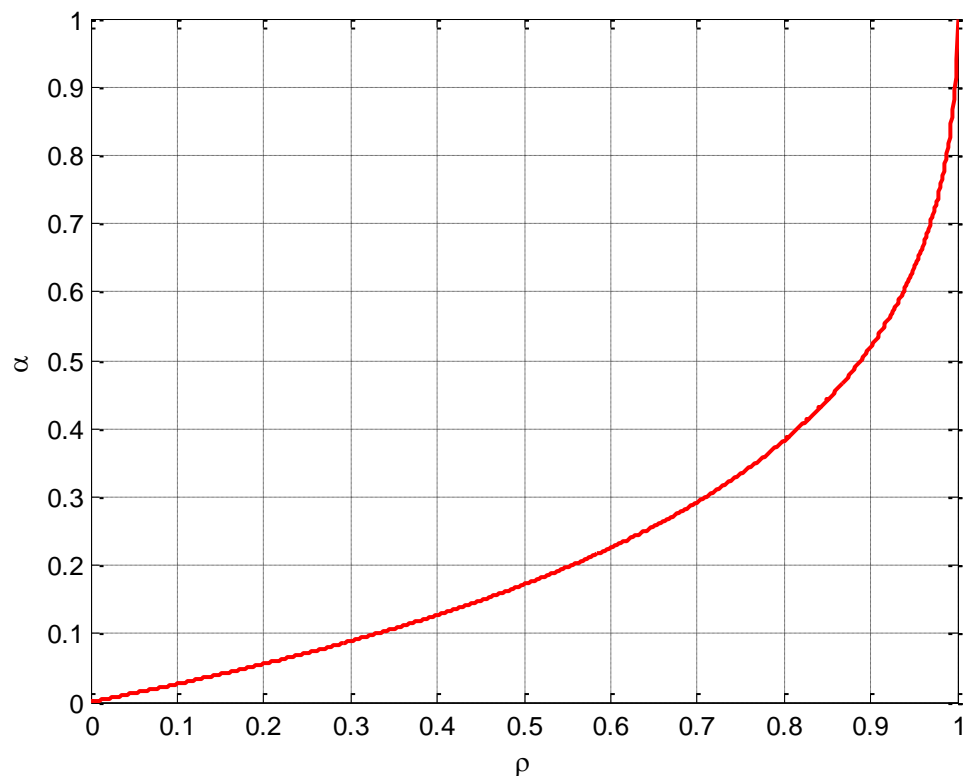
Figure 6.3. BSF as a function of BLF.

C.   Hybrid Improvement Factor (HIF)

This parameter provides a unitless measure of improvement introduced by the hybrid ESS versus battery alone. It is defined as the ratio of the battery BSF when used alone versus the battery BSF when used in a hybrid ESS. The definition is shown in equation 6.6 where μ is the efficiency of DC-DC conversion if present.

$$\beta(t) = \frac{\alpha_{battery}}{\alpha_{hybrid}} \qquad HIF: \beta[n] = \frac{\left(1+\sqrt{1-\mu \cdot D \cdot \rho[n]}\right)^2}{\mu^2 \cdot D \cdot \left(1+\sqrt{1-\rho[n]}\right)^2} \qquad (6.6)$$

HIF is a parameter that is highly sensitive to the duty cycle. Figure 6.4 shows HIF curves for different cases of BSF plotted versus duty cycle. HIF shows higher HIF for smaller duty cycle values. During cranking, the duty cycle is extremely small, which renders the hybrid design very useful from an HIF perspective.
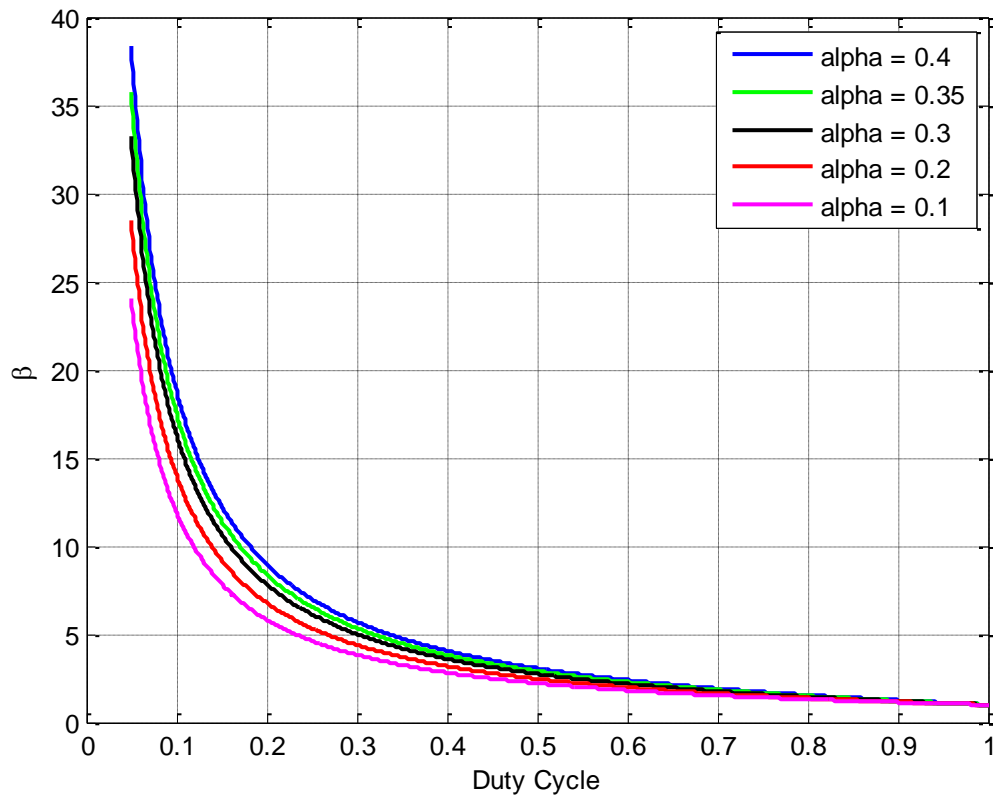
Figure 6.4. HIF curves for a number of BSF values.

D.   Charge Capacity Factor (CCF)

This parameter is an instantaneous unitless measure of the charge capacity used from battery alone versus charge capacity used from battery in the hybrid ESS as shown in equation 6.7.

$$\gamma(t) = \frac{Q_B(t)}{Q_H(t)} = \frac{\int_0^t i_L(\tau)d\tau}{\int_0^t i_{battery}(\tau)d\tau}$$

$$CCF: \gamma[n] = \frac{1+\sqrt{1-\mu \cdot D \cdot \rho[n]}}{\mu\left(1+\sqrt{1-\rho[n]}\right)} \qquad (6.7)$$

CCF can be plotted versus duty cycle as shown in figure 6.5. It is obvious that the value of CCF hovers around unity. This is due to the fact that the addition of an ultracapacitor module to the lead acid battery does not add much capacity to energy storage. The capacity in an ultracapacitor is only a small fraction of that of a battery's.
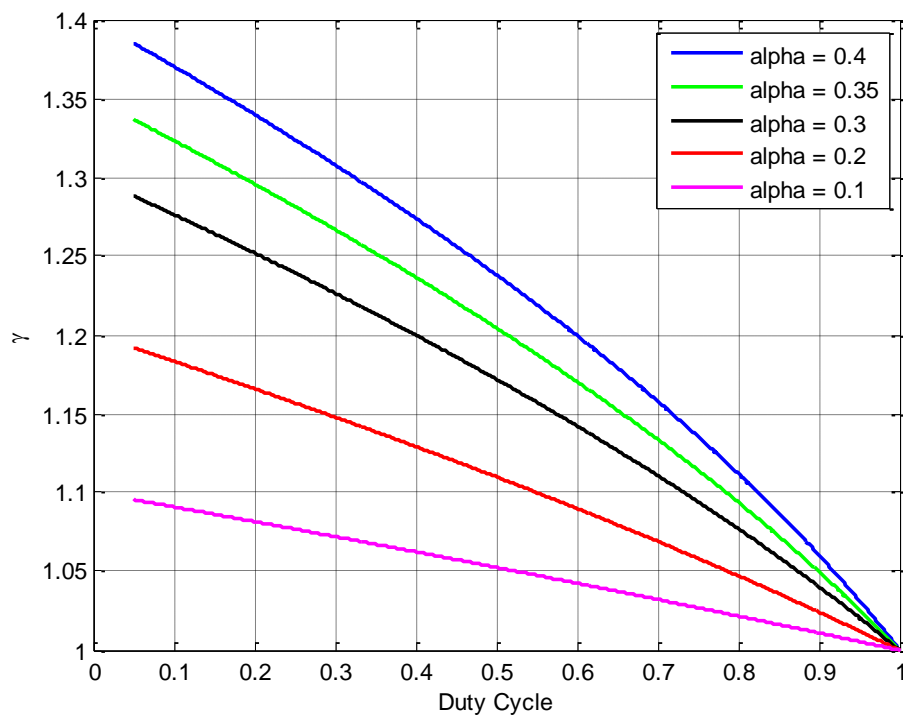
Figure 6.5. CCF versus duty cycle for different values of BSF.

E. Energy Capacity Factor (ECF)

This parameter provides an instantaneous unitless measure of the energy capacity used from battery in a hybrid system versus energy capacity used from battery alone. Equation 6.8 shows the definition of ECF.

$$\chi = \frac{E_H}{E_B} = \frac{\int_0^{\tau_1} v_{battery}(\tau) i_{battery}(\tau) d\tau}{\int_0^{\tau_2} v_{battery}(\tau) i_L(\tau) d\tau}$$

$$\chi = \frac{1+\sqrt{1-D\cdot\rho(\tau_1)}-\frac{D\rho(\tau_1)v_o}{4\Delta v}}{1+\sqrt{1-D\cdot\rho(\tau_2)}-\frac{D\rho(\tau_2)v_o}{4\Delta v}} = \frac{1+\sqrt{1-D\cdot\rho(\tau_1)}-\frac{D\rho(\tau_1)\sigma}{4}}{1+\sqrt{1-D\cdot\rho(\tau_2)}-\frac{D\rho(\tau_2)\sigma}{4}} \qquad (6.8)$$

where τ_1 and τ_2 are the times the pulse is applied to the battery in the hybrid module and the battery alone respectively, Δv is the difference between fully-charged battery voltage and fully-discharged battery voltage, and σ is the ratio of v_o to Δv. Figure 6.6 shows the ECF curves for a number of BSF values.
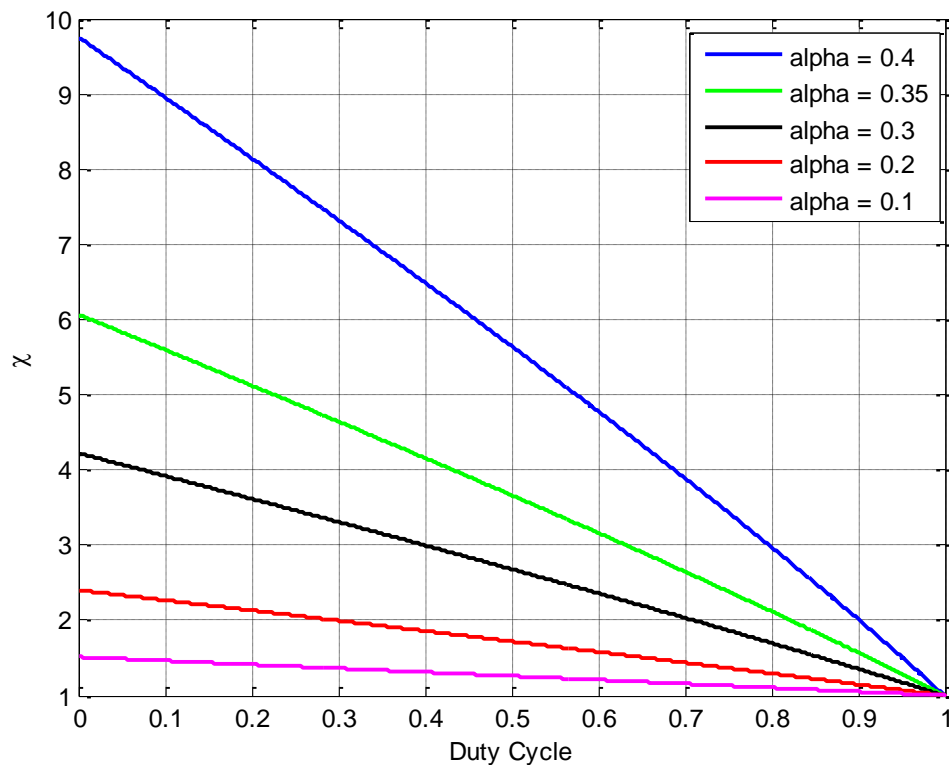
Figure 6.6. ECF versus duty cycle at different values of BFS.

Chapter 7. Experimental test setups and simulation results

This chapter presents the test and simulation results of the major milestones of this dissertation. Some test and simulation results of other experiments were presented in chapters due to the close connection with the text written.

7.1 Hybrid ESS testing

This section presents the designed hybrid ESS test setup and simulation results.

7.1.1 Hybrid ESS test setup

The hybrid ESS was tested on a Saturn Vue 2004 with a 4-cylinder 2.24 Liter Engine. Battery current, Ultracapacitor current, hybrid ESS voltage, and engine speed were measured. The engine speed was measured using a contactless laser sensor. The tests were conducted in a way that also took into consideration possibilities to shape the cranking current. Figure 7.1 shows the complete test setup on this car. The hybrid ESS is placed on a plastic cart and connected to the car circuitry terminals that were detached from the original car battery. An advanced Tektronix oscilloscope was used to collect data for two seconds.

Figure 7.1 Design Hybrid ESS test setup.

The designed hybrid ESS is made up of a lead acid battery connected to the ultracapacitor module directly in parallel. Two LEM current sensors are used to measure the battery and ultracapacitor module currents as shown in figure 7.2. In this configuration, the cable gauge wire and lengths between the battery and the hybrid ESS nodes are the exact same gauge wire and lengths as the cables connecting the ultracapacitor module to the Hybrid ESS nodes making this connection a balanced connection introducing no bias towards one of the two power sources versus the other.

Figure 7.2. Balanced parallel connection Hybrid ESS.

The starter motor that cranks this car is not a compound DC motor but rather a permanent DC motor. This simplifies the mathematical analysis needed to derive the

battery current versus the other parameters in the cranking circuit. Figure 7.3 illustrates the Saturn Vue cranking circuit that includes the designed hybrid ESS.
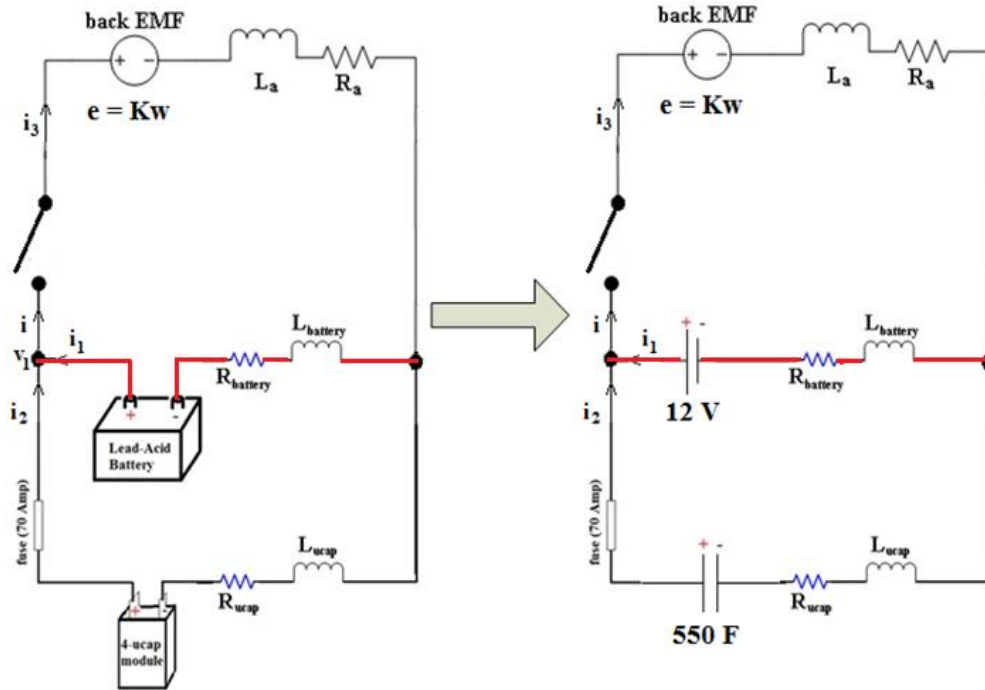
Figure 7.3. Saturn Vue cranking circuit with the hybrid ESS installed.

The equations modeling the cranking circuit follow the same analysis presented in chapter 5 with the more general compound DC motor. In this case, the presence of the permanent magnet DC motor reduces the analysis complexity and yields the battery current expression given by equation 7.2, which is a simplified version of equation 7.1.

$$i_1 = \cfrac{V_{bat} - E_a s + \cfrac{V_{bat}(L_a s^2 + R_a s)}{L_{cap} s^2 + R_{cap} s - \frac{1}{C}}}{R_{bat} s + L_{bat} s^2 + \cfrac{(L_a s^2 + R_a s)\left((L_{bat} + L_{cap})s^2 + (R_{bat} + R_{cap})s - \frac{1}{C}\right)}{L_{cap} s^2 + R_{cap} s - \frac{1}{C}}}$$

(7.1)

$$= \frac{-E_a L_{cap} s^3 + (V_{bat} L_{cap} - E_a R_{cap} + V_{bat} L_a)s^2 + (V_{bat} R_{cap} + V_{bat} R_a + \frac{E_a}{C})s - \frac{V_{bat}}{C}}{(L_{bat} R_{cap} + L_a(L_{bat} + L_{cap}))s^4 + (R_{bat} L_{cap} + L_{bat} R_{cap} + R_a(L_{bat} + L_{cap}) + L_a(R_{bat} + R_{cap}))s^3 + (R_{bat} R_{cap} + R_a(R_{bat} + R_{cap}) - \frac{L_{bat} + L_a}{C})s^2 - \frac{R_{bat} + R_a}{C}s}$$

(7.2)

7.1.2 Hybrid ESS simulation results

It was observed that the small resistance introduced by having an extension cable drastically changes the current response. This idea was discussed and simulated in chapter 5 under section 5.3. This section shows test and simulation results of three types of parallel connections. When the direct connection to the car circuitry is applied across the battery, the battery provides most of the cranking current. When the direct connection is applied across the ultracapacitor module, the module shows superiority during cranking. When the balanced connection is used, the ultracapacitor module still provides most of the cranking current. This gives the possibility of shaping the cranking current simply by designing a hybrid ESS with predetermined cable resistances that yield the desired cranking current sharing. Figure 7.4 shows a circuit diagram illustrating the battery biased parallel connection, a cranking test results, and simulation results obtained from simulating this particular circuit in Matlab Simulink of the system in figures 7.4 a, b, and c respectively.

(a)

(b)

(c)
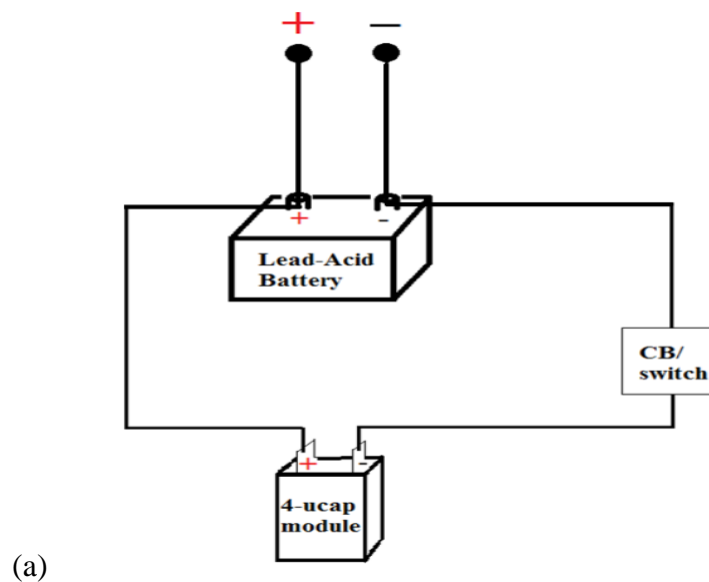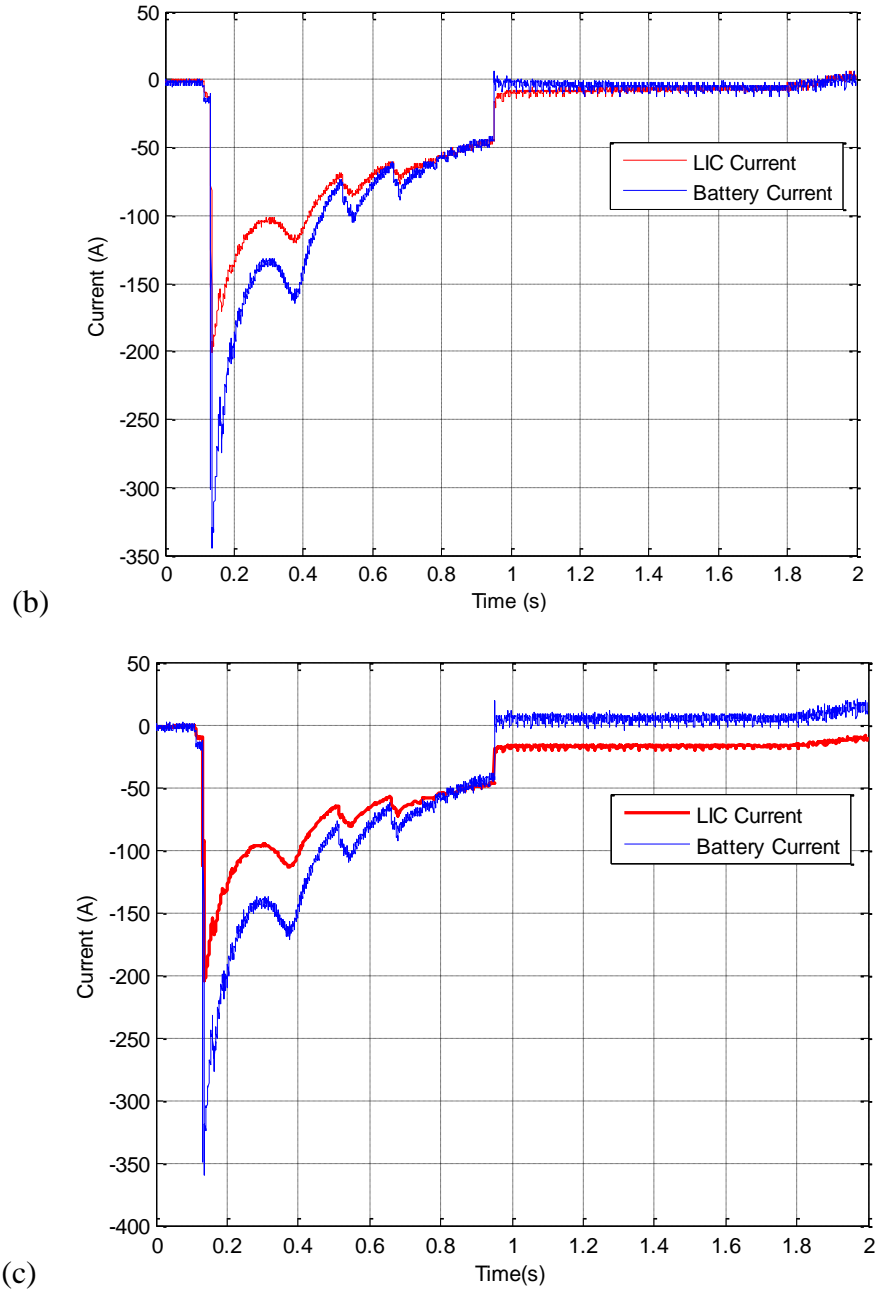
Figure 7.4. Battery biased parallel connection. (a) Connection diagram. (b) Test results. (c) Simulation results.

Figure 7.5 shows a circuit diagram illustrating the ultracapacitor module biased parallel connection, a cranking test results, and simulation results obtained from simulating this particular circuit in Matlab Simulink of the system in figures 7.4 a, b, and c respectively.
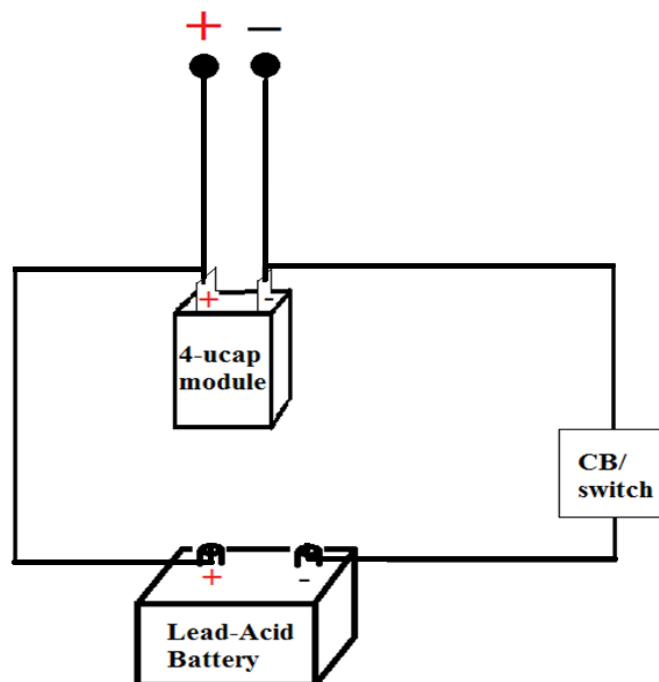
(a)
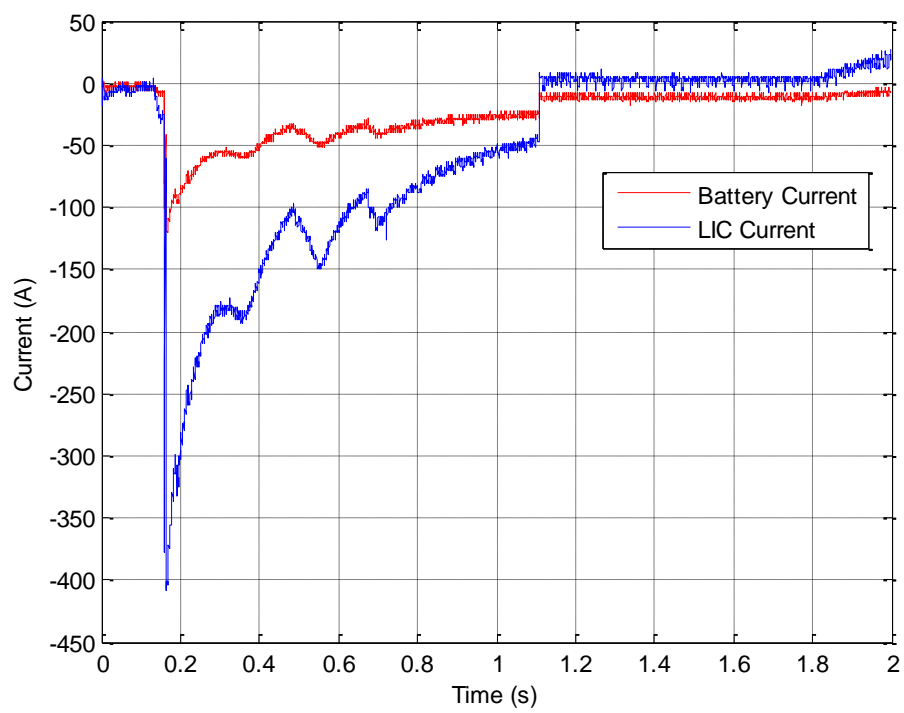
(b)
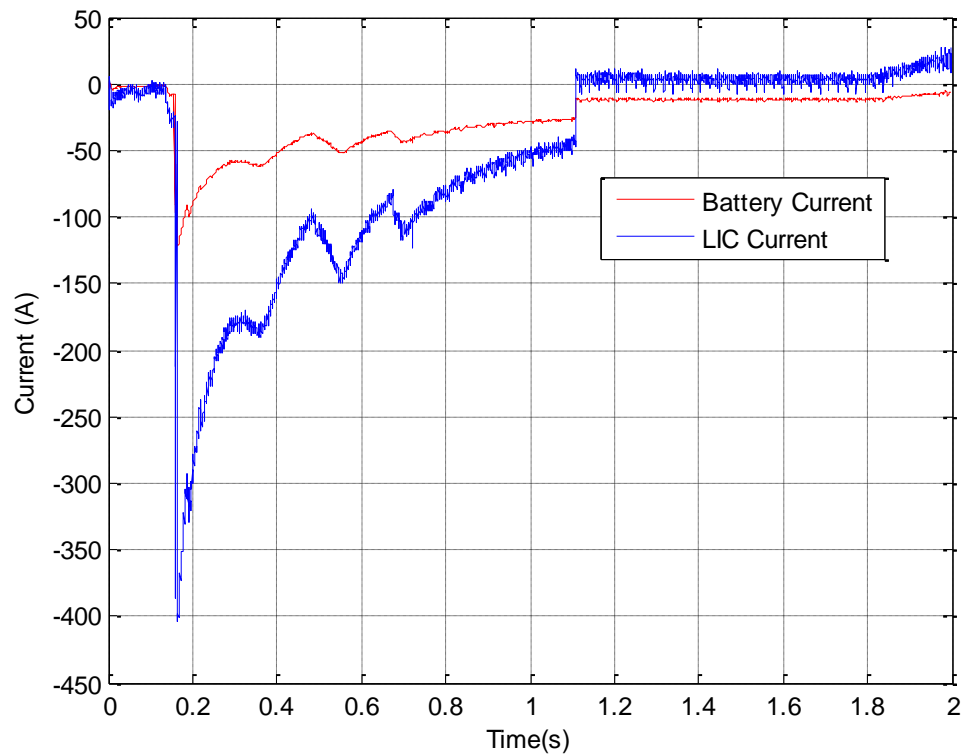
(c)

Figure 7.5. Ultracapacitor biased connection.(a) Connection diagram(b) Test results (c) Simulation results.

The balanced hybrid ESS connection test and simulation results are shown in figure 7.6 In the balanced connection, the ultracapacitor module provides most of the cranking current while the battery provides the smaller portion. The system voltage decreases to a minimum of 11 Volts only compared with the much lower voltage of 8.3 Volts of the lead acid battery when used alone for engine cranking. Figures 7.6 a, b, and c show the balanced connection circuit diagram, the test cranking currents of the hybrid ESS, and the simulation results of the cranking currents in the balanced connection respectively.
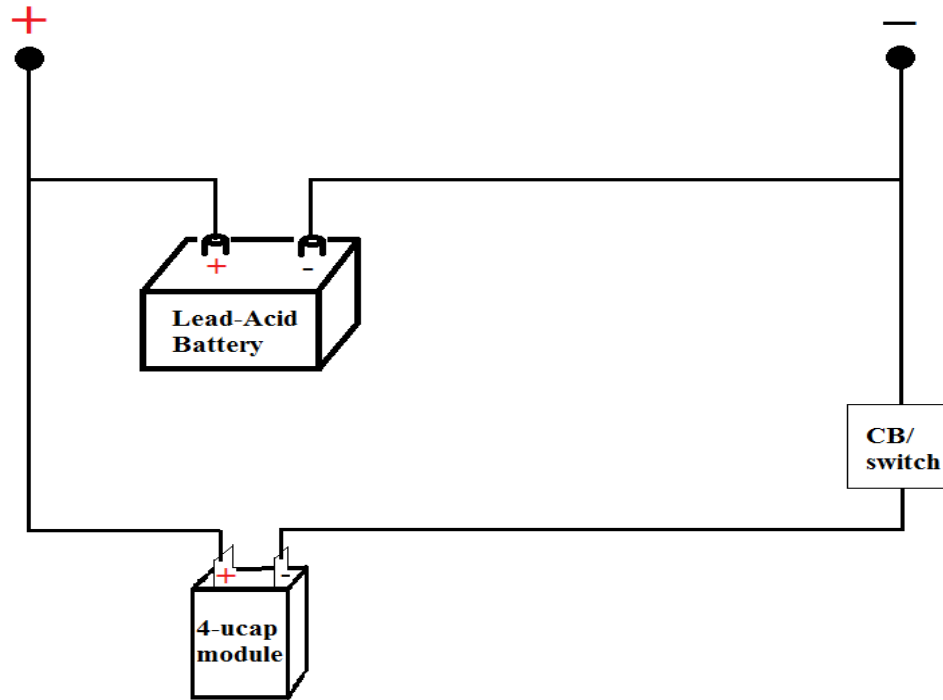
(a)
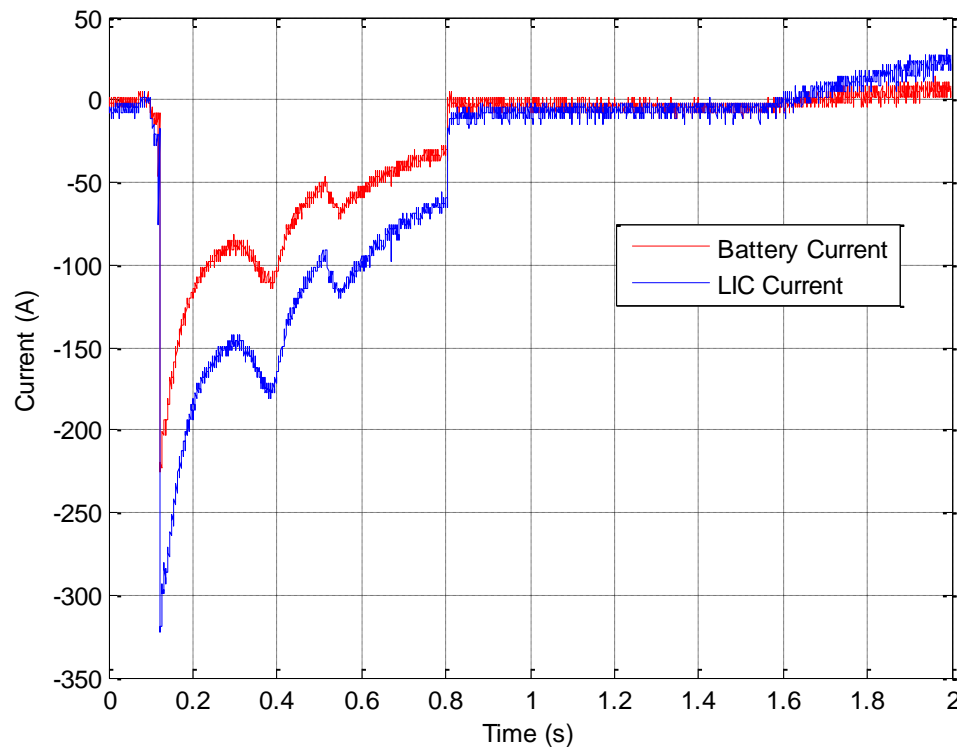
(b)
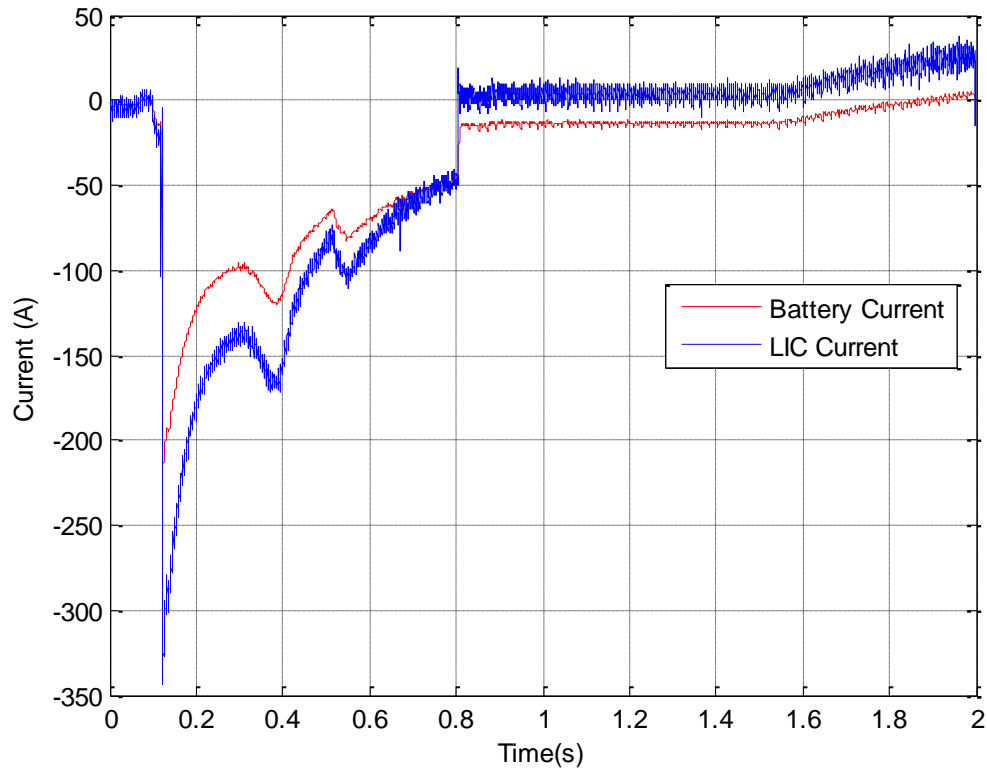
(c)

Figure 7.6. Balanced parallel connection. (a) Connection diagram. (b) Test results. (c) Simulation results.

7.2 Starter motor

The Saturn Vue starter motor was purchased and tested to extract its parameters for simulation purposes. This section discusses the testing and parameter extraction of this starter motor.

7.2.1 Starter Motor test setup

Figure 7.7 shows the test setup used for testing the starter motor. A DC power supply that can run constant voltage or constant current mode is used for testing. The applied voltage across the starter motor was 12 volts, which is the rated voltage. The current and speed waveforms were recorded so as to be used to extract the resistance and inductance of the armature winding of the starter motor. A LEM sensor is used to

measure the starter motor current and a laser contactless sensor is used to measure the speed of the cranking gear.
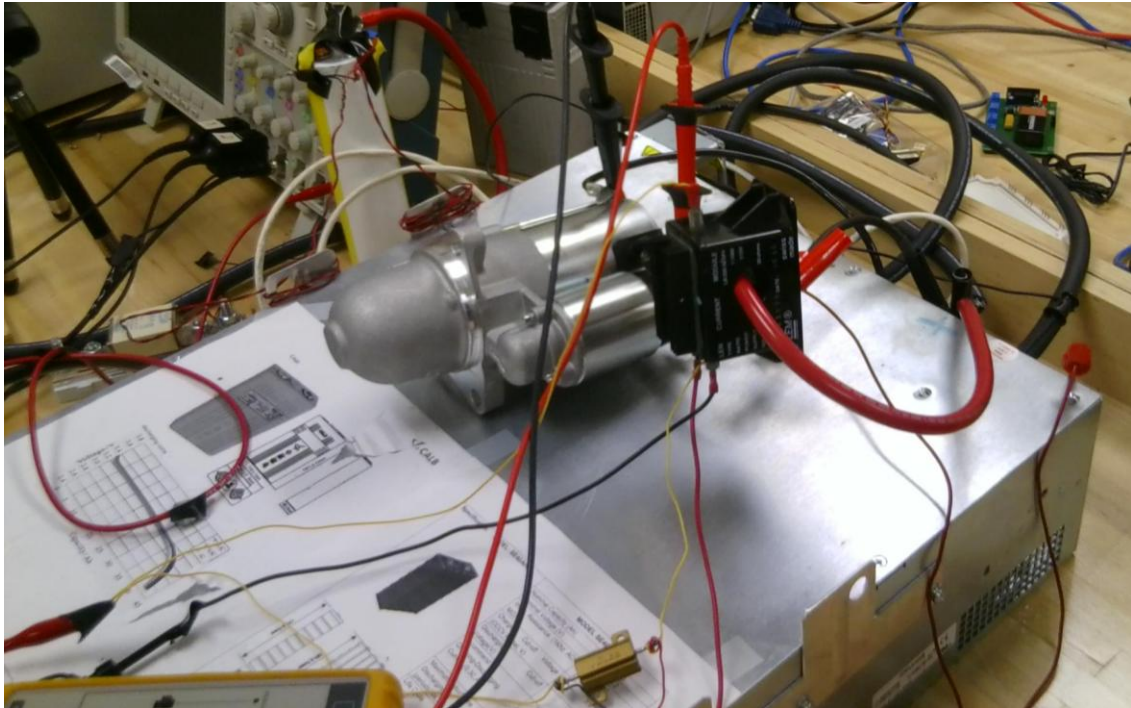
Figure 7.7. Starter motor test setup.

An image showing the structure of the starter motor is given by figure 7.8. The bigger cylinder to the left is the body of the motor while the smaller cylinder to the right is a solenoid that functions as a relay allowing current to pass through the starter motor only when the ignition key is in the switching position. the solenoid also enables a mechanism that pushes the cranking gear out so as to mesh with the shaft gear while cranking. once the key in the ignition cylinder is pulled back to the Run position, the solenoid is deactivated, which deactivates both the starter motor and the mechanism effectively pushing the cranking gear back in.

Figure 7.8. Saturn Vue starter motor.

Figure 7.9 shows a cross sectional view of the starter motor used. This figure shows the flow of current when the ignition switch is in the cranking position. The current flows first in the solenoid making it an electromagnet that pulls a bar of a ferromagnetic material, most likely a piece of steel, which is then pulled inside the solenoid shorting the path for current to pass through the armature winding of the starter motor and allowing the cranking gear to pop out.
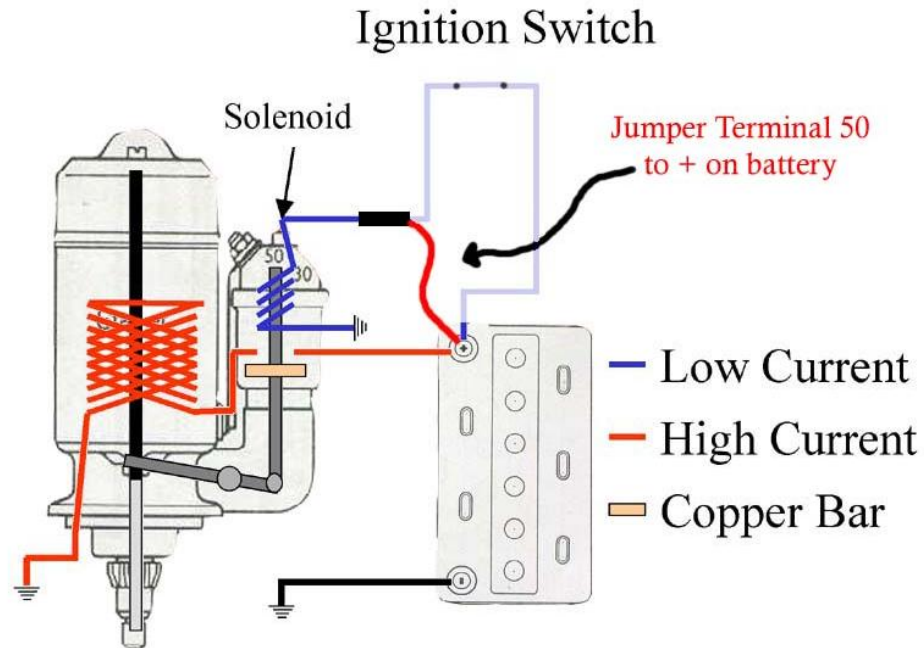
Figure 7.9. Starter motor cross sectional view.

7.2.2 Starter Motor test results

The starter motor test results are shown in figure 7.10. There are three stages in this test. The first stage is when the solenoid is activated at 0.1 seconds. The voltage across it rises according to the upper graph until it drops again when the relay is activated at 0.2 seconds. The current is the first stage is not shown because only the starter motor current was measured. Then the second stage kicks in at 0.2 seconds and that is when the starter motor armature current appears and decreases to the steady state no load value of 35 A at 12 Volts. And finally stage three is observed when the power supply current is manually cut off at 0.7 seconds, and the speed goes down linearly as the back EMF decreases linearly with respect to time. To extract the armature winding resistance and inductance, three equations with three unknowns, the armature winding constant k, the armature winding resistance, and armature winding inductance are to be calculated.
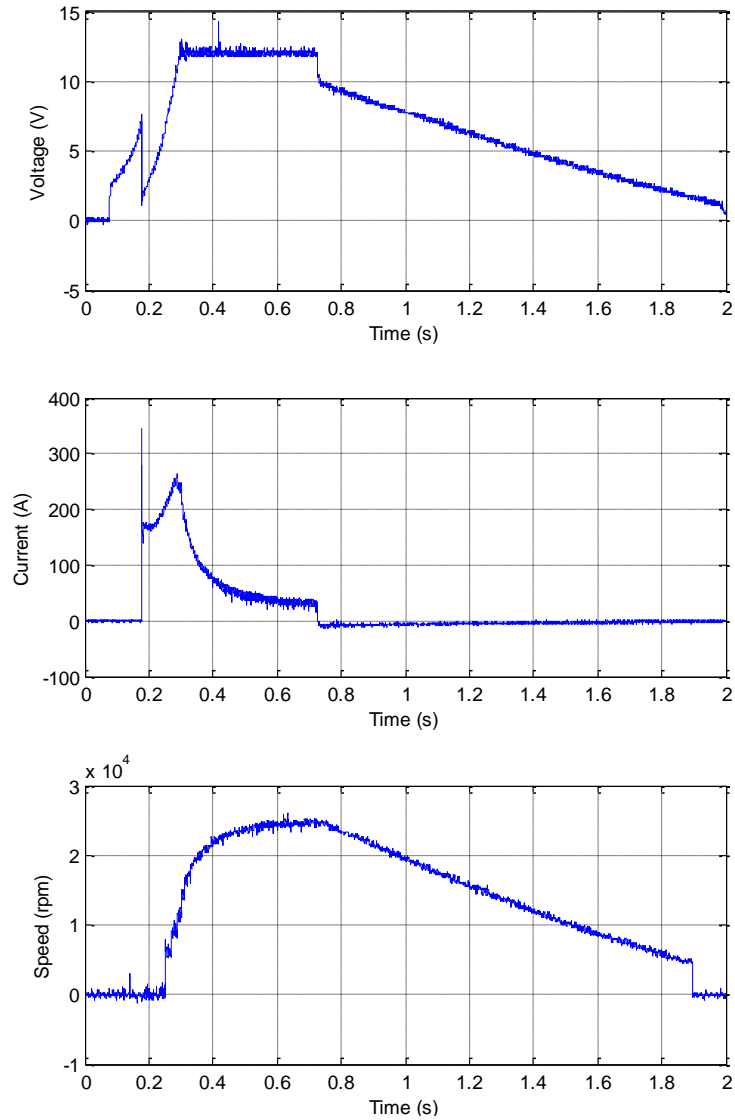
Figure 7.10. Saturn Vue starter motor test results.

The starter motor parameters were extracted and found to be as follows:

k = 0.00436 Vs/ rad

R = 22 mΩ

L = 35.6 mH

7.3 Cranking tests

A used car was purchased for the purpose of conducting a large number of

cranking tests the results of which were to be used to extract the aging parameter values.

Figure 7.11 shows the Audi 1996 2.8 L engine car. When it comes to the cranking tests, two types were conducted cold and warm cranking tests. Cold cranking happens when the engine temperature is not the optimum temperature for driving, i.e. the engine has not warmed up yet. Warm cranking happens when the engine is off with its temperature is high enough to the point where it is equal to the optimum operating temperature. 1000 battery alone tests and 1000 hybrid ESS tests were conducted.
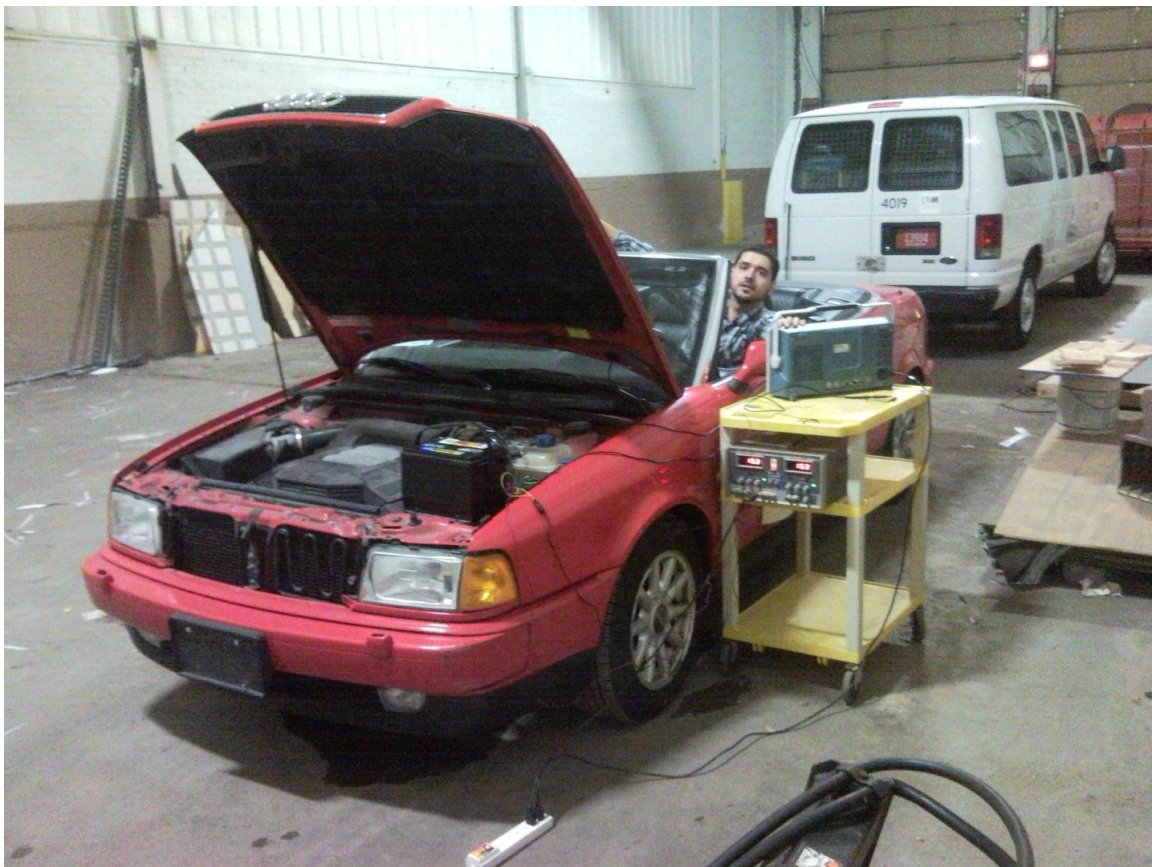
Figure 7.11. Audi 1996 used for conducting the cranking tests.

7.3.1 ICE battery alone cold cranking test results

Figure 7.12 shows the cold cranking results of a battery alone. The maximum cold cranking current is 745 A and the battery voltage drops to 9.84 Volts. The battery used was a brand new lead acid battery, which explains why the battery voltage did not drop

below 9 Volts. However, the normal cold cranking voltage is about 7 Volts. Cold cranking tests were conducted under 25 °C.
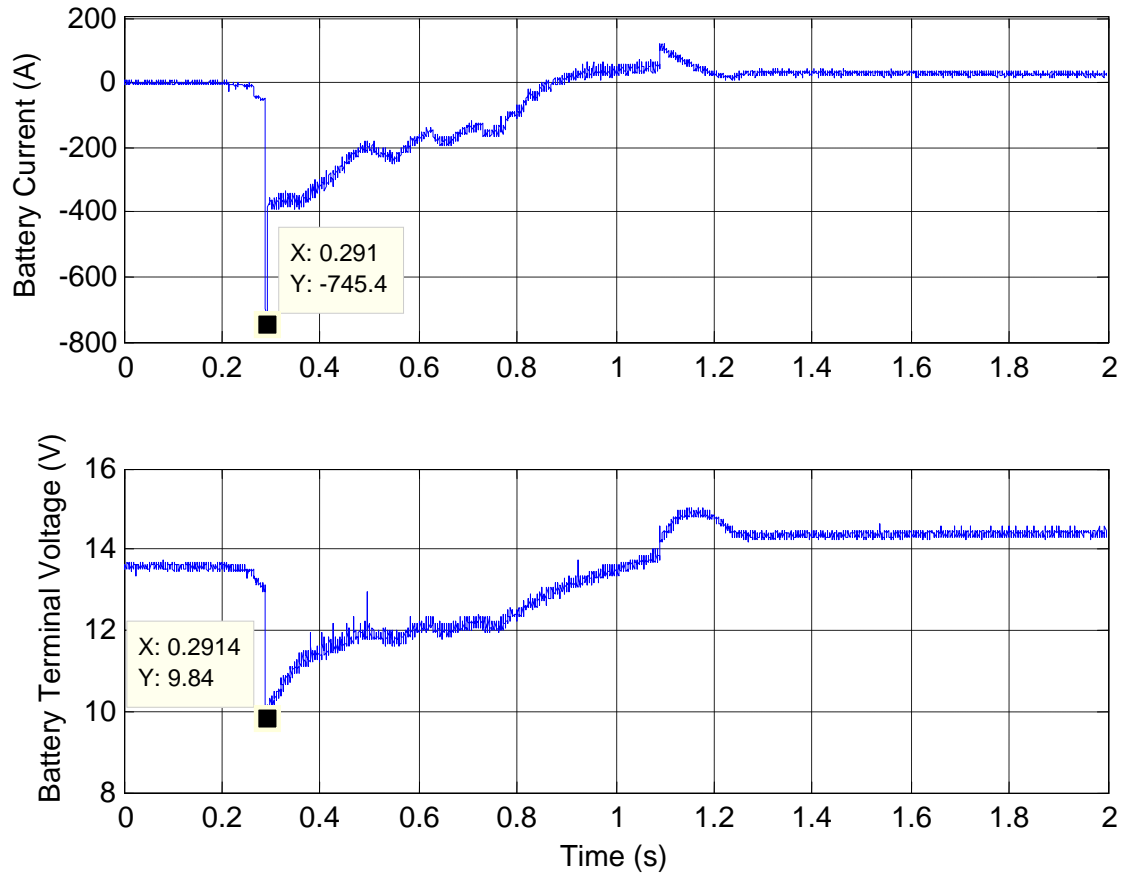
Figure 7.12. Battery alone cold cranking results.

7.3.2 ICE battery alone warm cranking results

Figure 7.13 shows the warm cranking results of the same lead acid battery alone. The maximum warm cranking current is 680 A and the battery voltage drops to 10.16 Volts. It is normal for a warmed up car to draw less cranking current and for its voltage to sag to a higher voltage value than the cold cranking case.
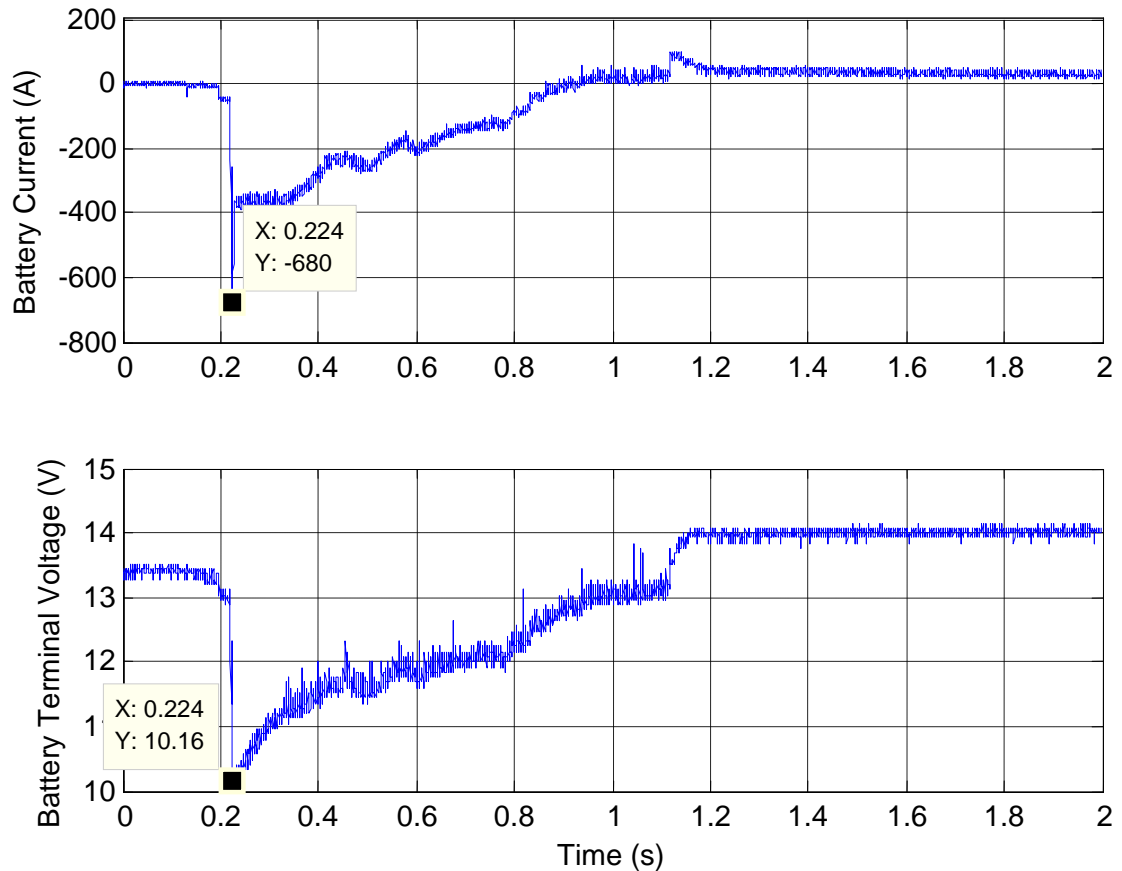
Figure 7.13. Battery alone warm cranking test results.

7.3.3 ICE hybrid ESS cold cranking test results

Figure 7.14 shows the cold cranking results of the hybrid ESS. The maximum cold cranking current of the battery inside the hybrid ESS is 283 A and the battery voltage drops to 11.84 Volts. The battery used was also a brand new lead acid battery to eliminate any aging factors related to shelf life or prior usage factors affecting the cranking test results.
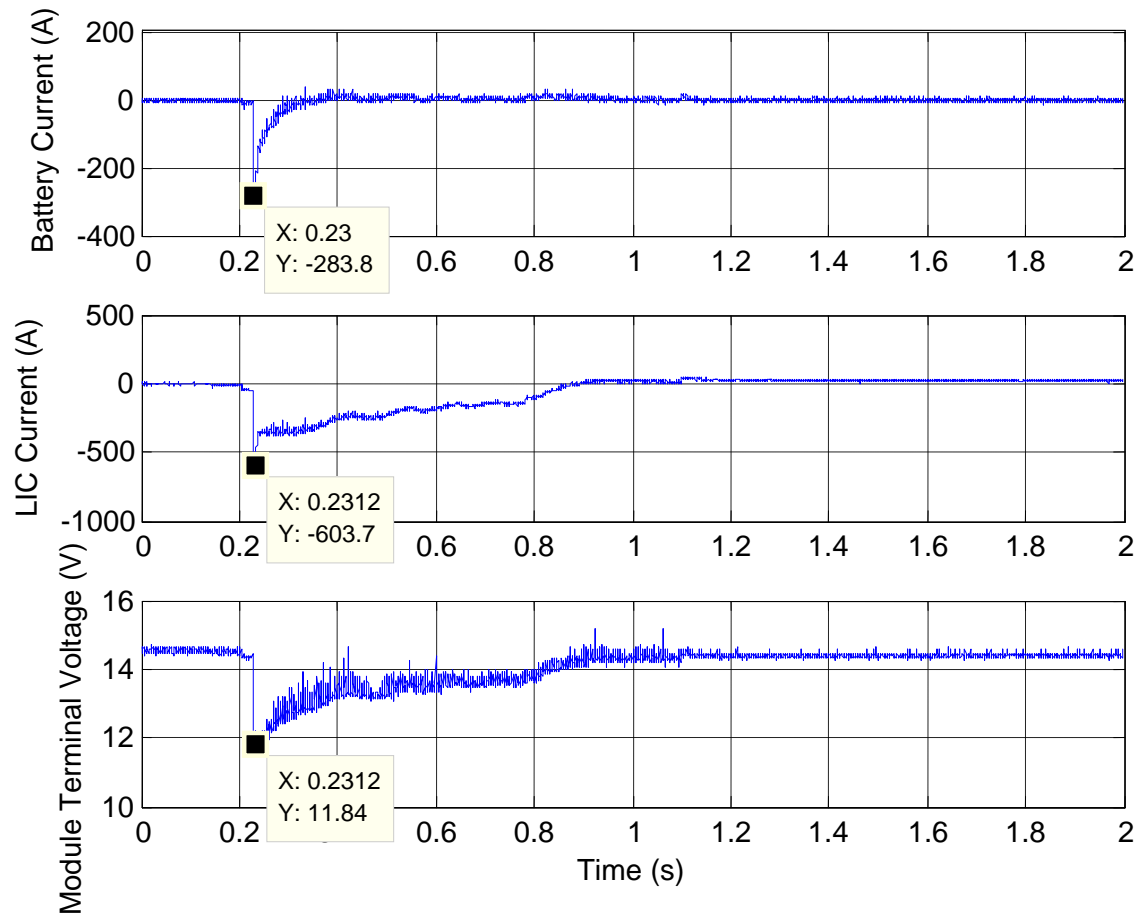
Figure 7.14. Hybrid ESS cold cranking results.

7.3.4 ICE hybrid ESS warm cranking test results

Figure 7.15 shows the warm cranking results of the same hybrid ESS used in the cold cranking case. The maximum cold cranking current of the battery inside the hybrid ESS is 212 A and the battery voltage drops to 11.92 Volts.
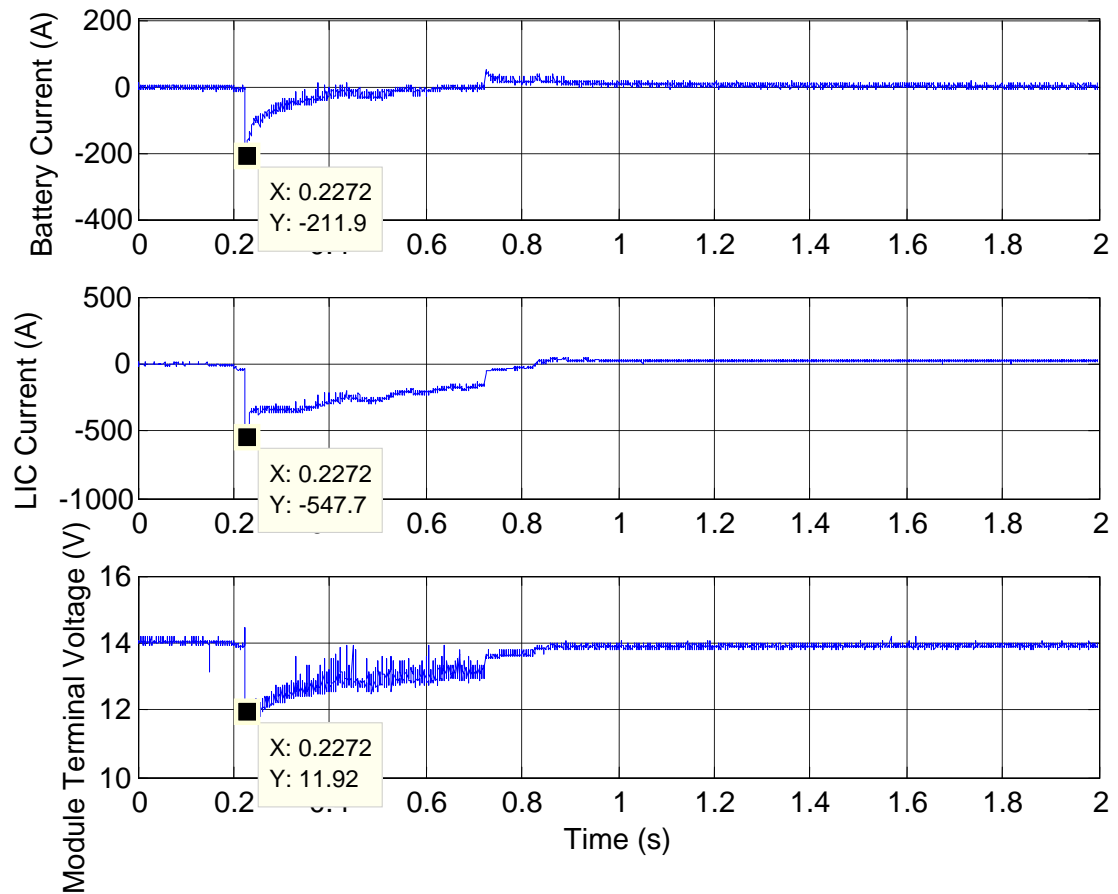
Figure 7.15. Hybrid ESS cold cranking results.

7.4 Capacity tests

The cranking tests mentioned in section 7.3 were conducted so that after every 200 tests a capacity test was conducted on the battery alone and the battery in the hybrid ESS to monitor the capacity of the lead acid battery so as to see if the cranking tests are affecting the capacity. The data were logged using Compact Rio and LabView was used to run the discharging and charging tests. Figure 7.16 shows the capacity test setup. A programmable power supply and an electronic load were used for charging and discharging the lead acid battery respectively.
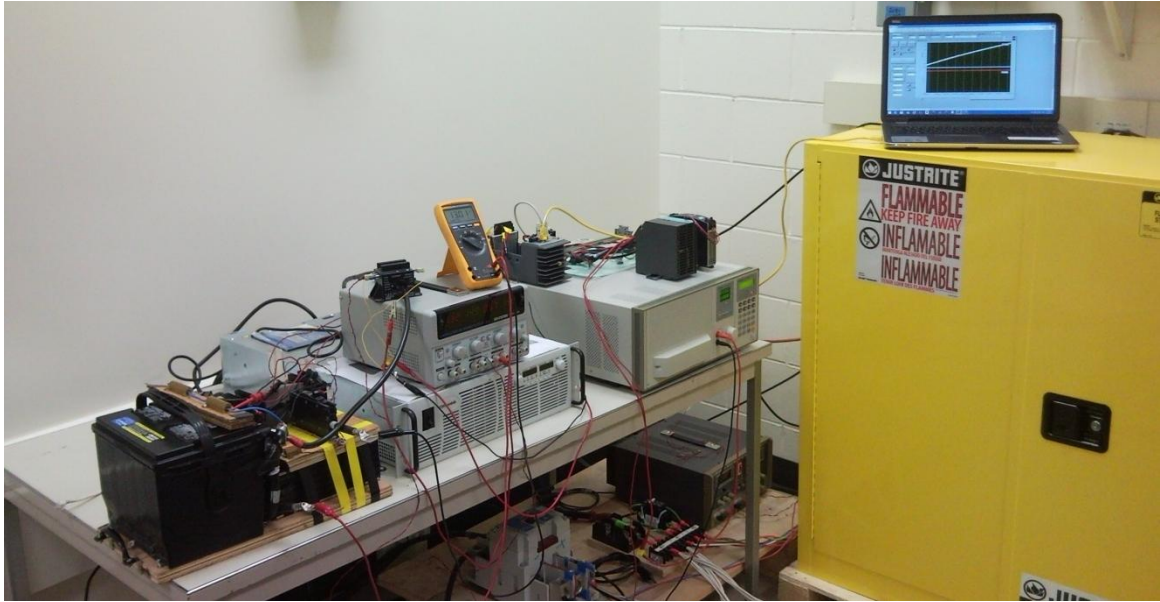
Figure 7.16. Capacity test setup.

7.4.1 Discharging Capacity check tests

The discharging test aims at calculating the capacity left in the lead acid battery via measuring the time it takes the battery to discharge under constant current until its terminal voltage reaches 10 Volts. The electronic load is used and the constant discharging current is 7.5 A as shown in the figure 7.17 showing the constant discharging current in the upper graph. The current is turned off automatically as soon as the battery terminal voltage reaches the predetermined limit of 10 Volts.
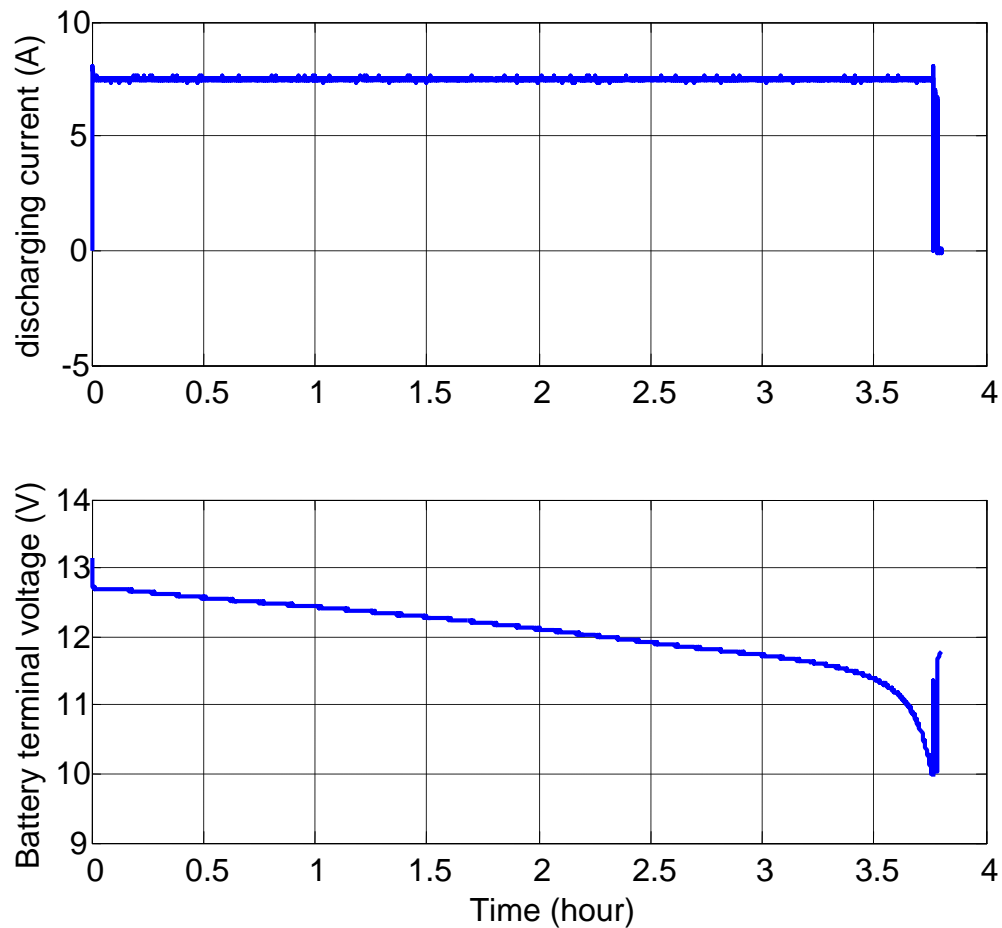
Figure 7.17. Discharging capacity check test.

7.4.2 Charging tests

The charging test aims at recharging the lead acid battery to the fully charged status. This is done under constant current of 22.5 A until its terminal voltage reaches 14 Volts. Then the power supply switches to a constant voltage mode and the current is adjusted so that the upper voltage limit is respected. The current decreases as time passes until it reaches a value lower than 1 A, and this is when the power supply is switched off and the battery is declared fully charged. Figure 7.18 shows the charging current in the upper graph. In this particular charging case, the constant voltage mode is reached after almost 36 minutes from the starting point of the test.
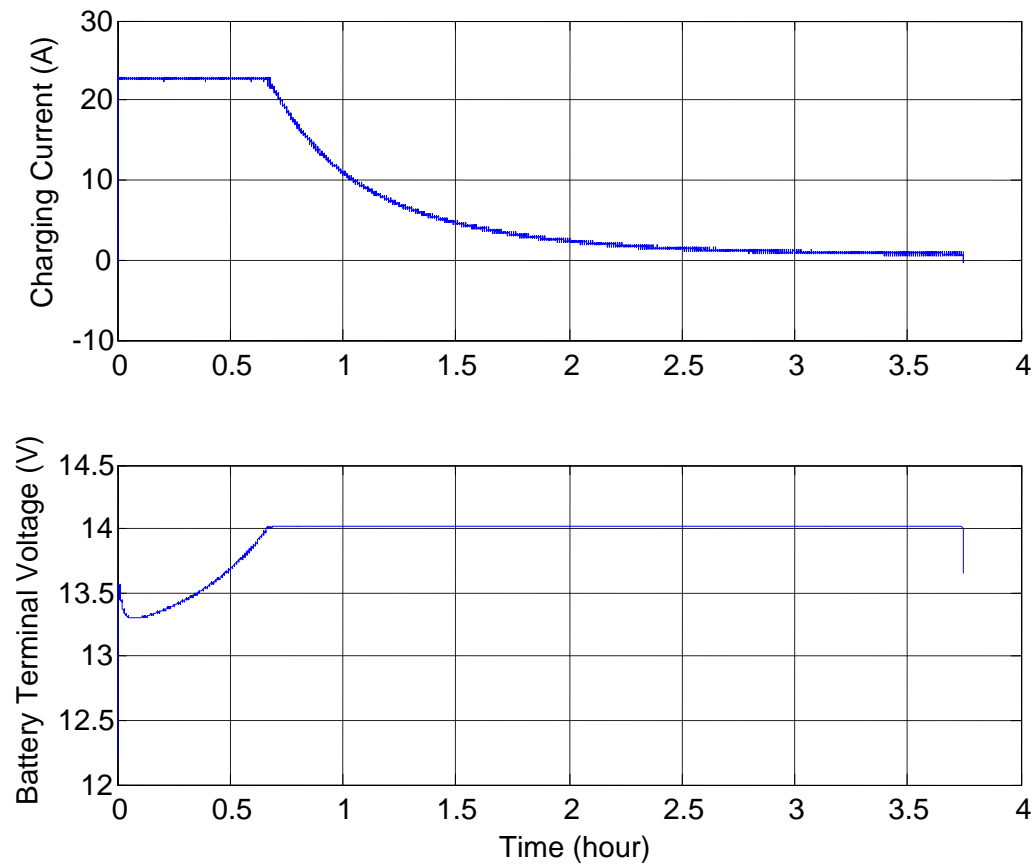
Figure 7.18. Lead acid charging test.

It is interesting to look at table 7.1 showing the capacity values for both the lead battery alone and the lead acid battery inside the hybrid ESS module after each step of 200 cranking tests. It is clear that after a 1000 cranking tests, the battery alone suffered a harsher capacity drop than the battery integrated with the ultracapacitor module.

Table 7.1. Capacity check test results for both eth battery alone and the battery in the hybrid ESS.

	Capacity of Battery Alone	**Capacity of Hybrid Battery**
Step 0	28.215 Ah	28.36 Ah
Step 1	25.56 Ah	26.8 Ah
Step 2	25.11 Ah	25.8 Ah
Step 3	24.96 Ah	25.79 Ah
Step 4	24.855 Ah	25.7 Ah
Step 5	22.7 Ah	25.245 Ah

7.5 Test results for aging parameter

The values of the aging parameters in cranking tests are found for the battery in the hybrid ESS as well as when it is used alone to crank the engine for both cold and warm cranking. The battery loading factor, battery stress factor, and hybrid improvement factor are calculated based on the maximum cranking current. The charge capacity factor and energy capacity factors are calculated based on the entire period of time during which cranking takes place. Under cold cranking, the battery loading factor decreased from 0.995 to 0.55 and the stress factor decreased from 0.866 to 0.197as a result of integrating the battery with the ultracapacitor module in the hybrid ESS. As for warm cranking, the battery loading factor decreased from 0.743 to 0.443 and the stress factor decreased from 0.743 to 0.145 as a result of hybridization. The improvement factor for cold cranking is 4.4 meaning that the battery inside the hybrid ESS is 4.4 times less stressed than the

battery alone. As for warm cranking, HIF is 5.5. The charge capacity factor is 14.99 and 8.23 for cold cranking and warm cranking respectively. That means that the battery alone provides 14.99 times the capacity that the same battery provides in the hybrid ESS. The energy capacity factor is 13.92 and 7.5 for cold cranking and warm cranking respectively. That means that the battery alone provides 13.92 times the energy the same battery provides in the hybrid ESS. These results show significant improvement to the loading conditions for the battery in the proposed hybrid ESS versus the battery alone. In summary, loading and stress are reduced while the HIF, CCF, and ECF are increased. Table 7.2 shows the aging parameter values calculated for each cranking case. The duty cycle for these numbers was not taken into consideration. The calculations were based on the maximum cranking current.

Table 7.2. Aging parameter values.

	BLF	BSF	HIF	CCF	ECF
Battery alone cold	0.995	0.866	NA	NA	NA
Hybrid ESS cold	0.55	0.197	4.4	14.99	13.92
Battery alone warm	0.978	0.743	NA	NA	NA
Hybrid ESS warm	0.443	0.145	5.12	8.23	7.5

Judging from table 2.1 in chapter 2 as well as the values calculated for aging parameters, there is a clear correlation between hybridization and the capacity sustained in the battery inside the hybrid ESS versus the battery alone that experienced significant

drop in capacity after a thousand cranking tests. While there is no clear models that predict aging of lead acid batteries and given the diagnostic nature of the aging parameters, it can be deduced that the aging parameters can be used to predict the aging process or even age of lead acid batteries. Nevertheless, more data points are needed to know when the battery reaches extremely low capacity content. This can be done experimentally on a brand new battery until it reaches a value of capacity at which the battery cannot provide enough power to crank the engine. While conducting these tests, expected to be several thousands, voltage and current will be recorded and the aging parameters can be calculated. This enables the possibility of monitoring the aging parameters progress as the battery is aging, i.e. while its capacity is periodically measured, until it reaches its end of life. The same tests can be done on a sample of lead acid batteries large enough to be used to establish a lookup table for lead acid battery age estimation. All of the aging parameters defined in chapter 6 can be used together to estimate the battery age after creating the 5-dimensional lookup table that corresponds to the five parameter values obtained from the tests. An X-labeled battery with unknown history can be tested once and then the lookup table can be used to estimate its age after fitting its aging values

7.6 Lead acid battery model verification

A Comparison between simulation of a Matlab Simulink lead-acid battery and test results from an actual battery as necessary to validate the model suggested by Simulink. Therefore a number of comparisons are presented in this section. Figure 7.19 shows the Simulink model created to generate the simulated lead acid battery voltage experienced while ranking an engine. The input to the Simulink lead acid battery symbol is the

cranking current profile that simulates the cranking current loading to the battery. one of

the outputs of the lead acid battery symbol is the battery terminal voltage with which the

actual test lead acid battery terminal voltage was to be compared.
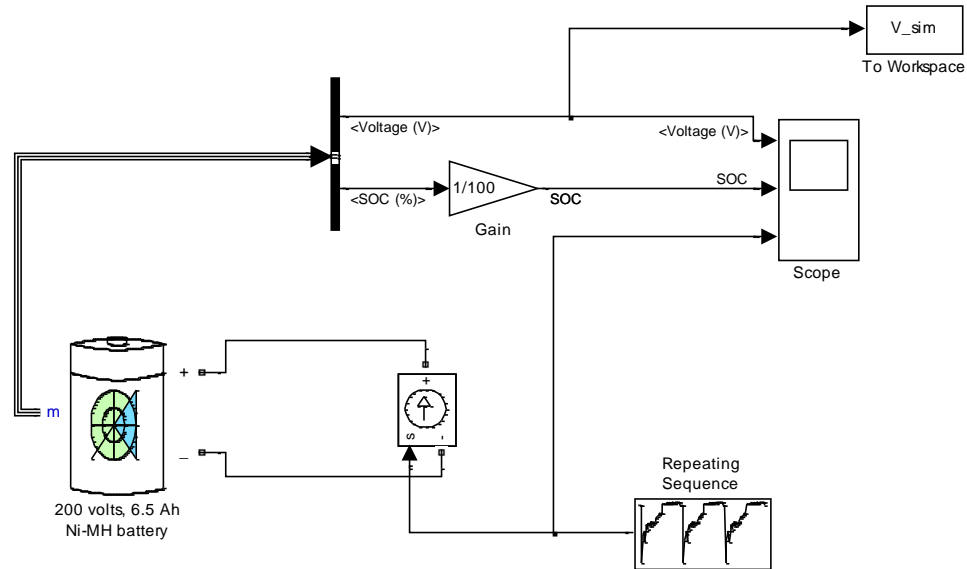
Figure 7.19. Simulink model used to generate simulated cranking battery voltage.
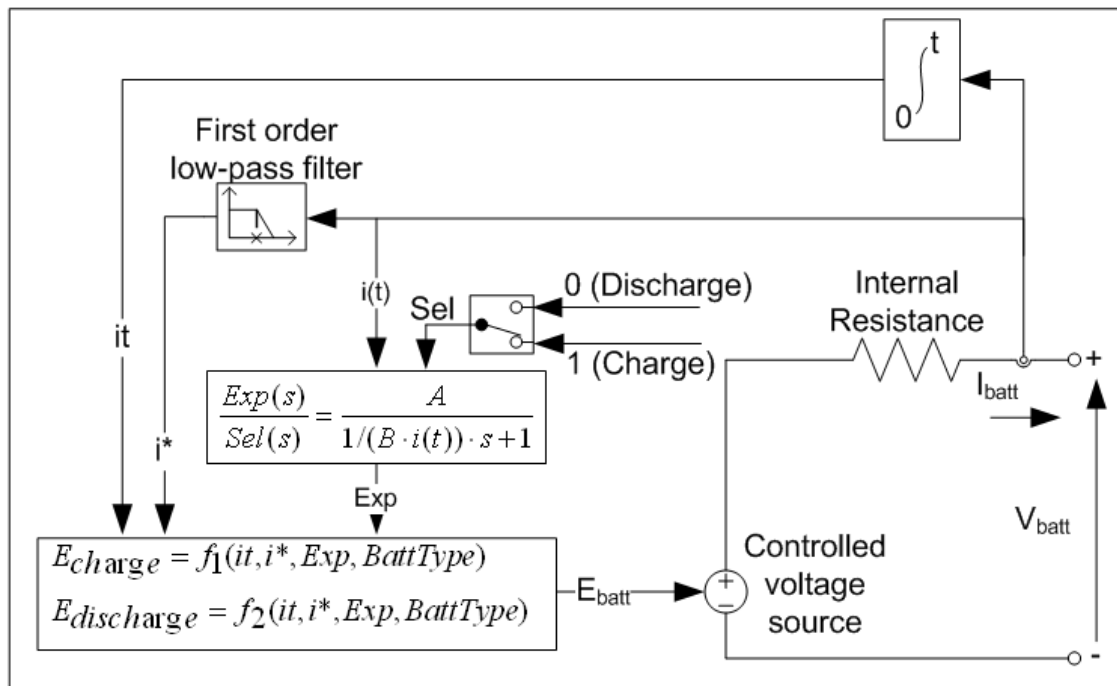
Figure 7.20. Simulink circuit based model used in the simulation.

Figure 7.20 shows the circuit based model that is used in the simulation of the lead acid battery. The model is a simple dependent voltage source in series with an internal resistance. Despite its simple design, the model works very well. Figures 7.21, 7.22, 7.23, 7.24 show comparisons between test results and simulation results for four types of cars used for cranking tests.
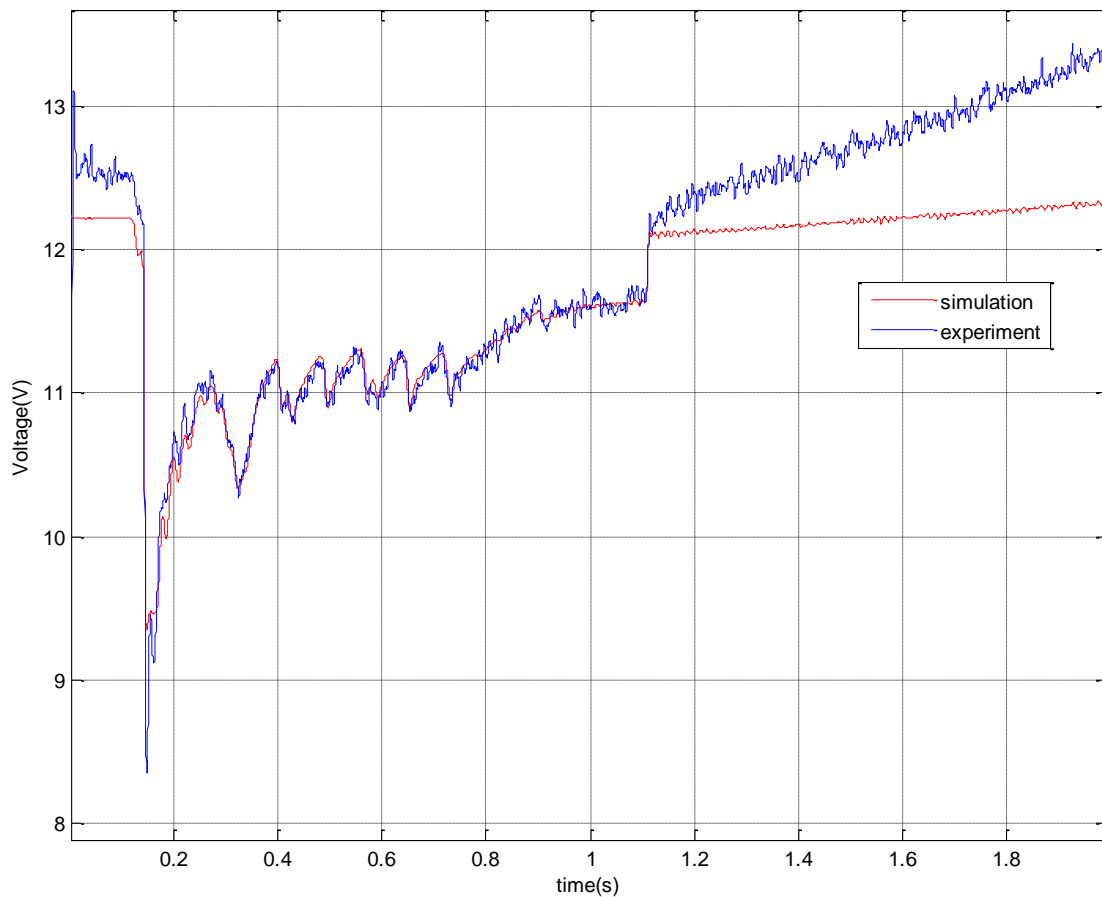
Figure 7.21. Test and simulation results on a Toyota Solara 2002.
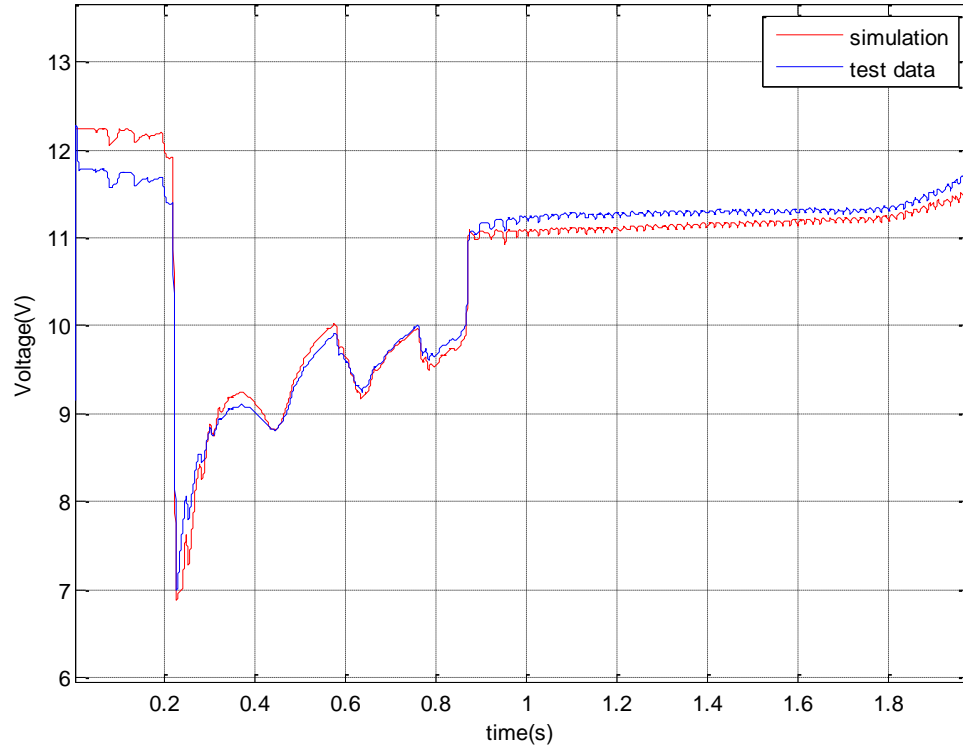
Figure 7.22. Test and simulation results on a Saturn Vue 2004.
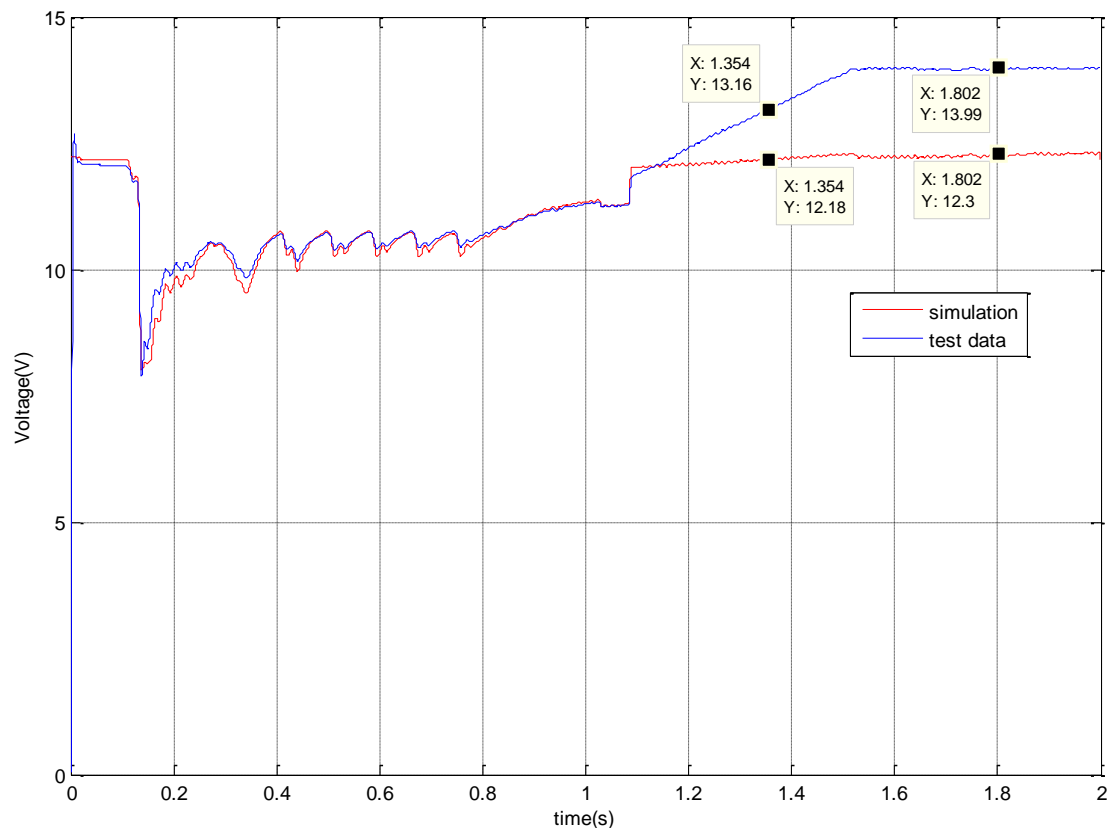
Figure 7.23. Test and simulation results on a second test on a Toyota Solara 2002.
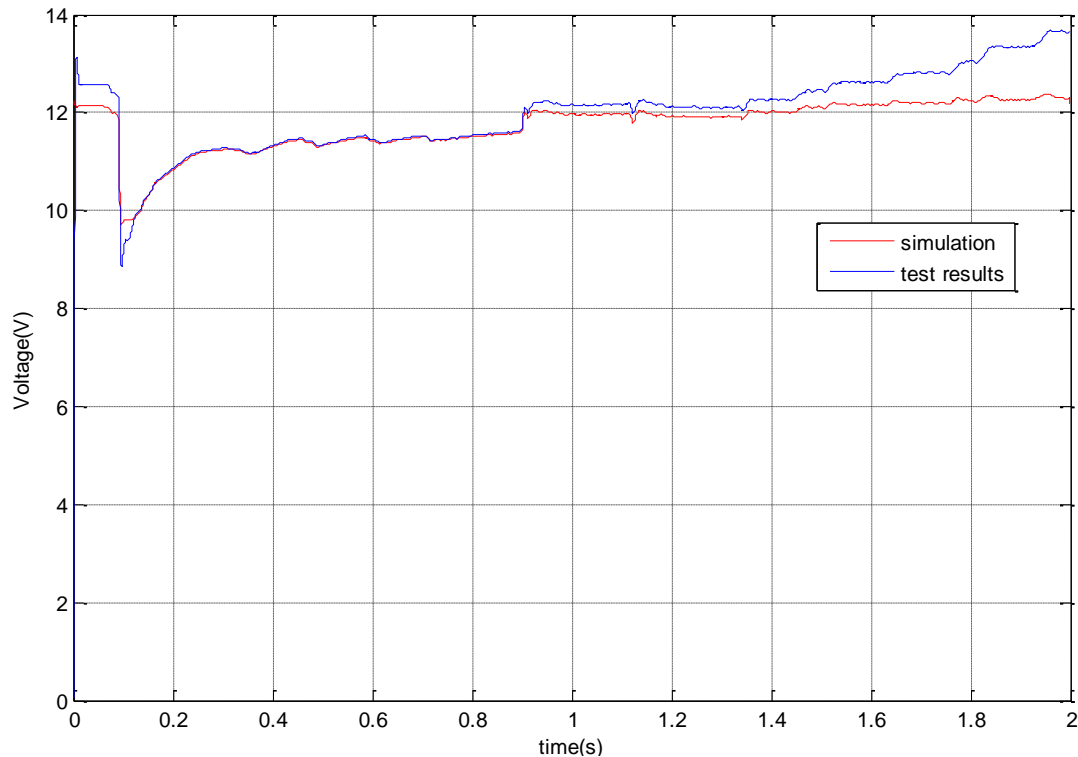
Figure 7.24. Test and simulation results on a Ford Focus 2011.

In figures 7.21, 7.22, 7.23, and 7.24, the cranking phase voltage from test and simulation match very closely. However, the charging phase voltage waveforms are quite apart. This is expected as the voltage across the battery during charging by the car alternator is imposed by the alternator/lead acid reacting together where the alternator pulls the voltage across its terminals higher than the terminal voltage of the battery in order to inject charging current into it. The simulation circuit in Simulink however takes in charging current and shows the voltage response of the lead acid battery as a result of this charging current assuming no external voltage source is imposed across its terminals, which does not match what happens in reality and hence the mismatch in the charging phase.

Chapter 8. Conclusions and future research

This dissertation presents a hybrid energy storage system (ESS) made from a lead acid battery and an ultracapacitor module connected in a parallel configuration. Before the connection was made, the Li-ion ultracapacitor was tested and an electric circuit equivalent model was developed to predict its behavior when connected in a system requiring energy storage. Battery modeling was reviewed and presented in chapter 4 as a necessary step to understand the battery behavior before the Li-ion ultracapacitor/ lead acid battery hybrid system was assembled.

The motivation behind this hybrid ESS design was to develop a system that may reduce the stress on the battery while cranking the internal combustion engine for the vehicular start-stop feature that requires automatically turning off and on the ICE repeatedly. The ICE cranking requirements were to be carefully studied, and this was achieved by conducting cranking tests on cars from different manufacturers and year models. Cranking data were acquired and used to calculate cranking requirements.

Cranking current stresses the battery rendering a short life span. This hybrid ESS is modeled, simulated, and tested. The test and simulation results show that the proposed hybrid design significantly reduces the cranking loading and stress on the battery. The ultracapacitor module can take the majority of the cranking current, effectively reducing the stress on the battery. The amount of cranking current provided by the ultracapacitor can be easily controlled via controlling the length, hence resistance, of the cable connected directly between the ultracapacitor module and the car circuitry.

A study is then presented to define a number of parameters that can be used to measure an ESS loading, stress, improvement gained by introducing a hybrid ESS, capacity improvement, and finally energy improvement. This study is based on a pulsed power profile having a short pulse power over a period of time. The aforementioned parameters are diagnostic but not predictive. That is, they can diagnose a hybrid energy storage system on five levels, but they cannot predict the life span after hybridization. In order to gain the capability to predict the life span of an energy storage system in a hybrid system versus the energy storage system alone, further research and experimentation should be conducted.

From an experimental point of view, life span estimation can be achieved by resuming cranking tests the same way they were conducted until the capacity of the battery alone reduces to a level where it is no longer capable of cranking the engine. Then, a curve showing the degradation of capacity versus counts of loading and/or stress can be made showing how long the battery alone can live to provide cranking power and energy versus how long the same battery can live in a hybrid ESS providing the same requirements to crank the engine.

Having established the fact that the hybrid ESS offers significant reduction on the loading and stress the lead acid battery experiences during cranking, the designed hybrid ESS can now be road tested, and data can be collected in order to establish statistical results showing the gas savings that can be achieved with an implemented start-stop feature without inflicting damage to the lead acid battery.

References

[1] "20% Wind Energy by 2030: Increasing Wind Energy's Contribution to US Electricity Supply". U.S. Department of Energy.

[2] B. Dunham. "Automatic on/off switch gives 10-percent gas saving". *Popular Science*, pp. 170, 1974.

[3] http://www.caranddriver.com/features/engine-stop-start-systems-explained-tech-dept Retrieved June 6, 2013.

[4] D. Haifeng. C. Xueyu. "A Study on Lead Acid Battery and Ultracapacitor Hybrid Energy Storage System for Hybrid City Bus" International Conference on Optoelectronics and Image Processing. pp. 154-159, 2010.

[5] A. F. Burke, E. J. Dowgiallo, and J. E.Hardin. "Application of ultracapacitors in Electric vehicle Propulsion Systems." Proceedings of the 34th International Power Sources Symposium, pp. 328-333, 1990

[6] S. Pay and Y. baghzouz. "Effectiveness of Battery-Supercapacitor Combination in Electric Vehicles." PowerTech Conference Proceedings. Bologna 2003.

[7] Z. Chen. "High Pulse Power System Through Engineering Battery-Capacitor Combination." Energy Conversion Engineering Conference and Exhibit, 2000. (IECEC) 35th Intersociety, pp. 752-755.

[8] R. Douglas, S. Liu, and R. E. White. "Power and Life Extension of Battery-Ultracapacitor Hybrids." IEEE transactions on components and packaging technologies. vol. 25, no. 1, pp. 120-131

[9] F. Gagliardi and G. Maestri. "Experimental Results of on-board Battery Ultracapacitor System for Electric Vehicle Applications." Proceedings of the 2002 IEEE International Symposium on Industrial Electronics, 2002. ISIE 2002. vol. 1, pp. 93-98.

[10] L. Gao, R.A. Dougal, and S. Liu. "Active Power Sharing in Hybrid Battery/Capacitor Power Sources." Eighteenth Annual IEEE Applied Power Electronics Conference and Exposition, 2003. APEC '03. vol. 1, pp. 497-503.

[11] http://www.italiaspeed.com/2009/cars/fiat/02/regatta_es/1602.html. Retrieved June 17, 2013.

[12] http://www.autoevolution.com/news/alfa-mito-to-get-multiair-engines-start-stop-system-7713.html. Retrieved July 18, 2013.

[13] http://world.honda.com/news/1999/4990906c.html. Retrieved July 18, 2013.

[14] http://www.autocar.co.uk/car-review/first-drives/volvo-s40-1.6d-drive-start/stop. Retrieved July 18, 2013.

[15] J.R Anstrom, B. Zile, K. Smith, H. Hofmann, A. Batra, "Simulation and Field-Testing of Hybrid Ultra-Capacitor/Battery Energy Storage Systems for Electric and hybrid-electric Transit Vehicles" Applied Power Electronics Conference and Exposition. vol. 1, pp. 491-497, 2005.

[16] E. Ozatay, B. Zile, J. Anstrom, and S Brennan. "Power Distribution Control Coordinating Ultracapacitors and Batteries for Electric Vehicles". Proceedings of the 2004 American Control Conference. Boston, Massachusetts. pp. 4716-4721, 2004.

[17] G. Zorpette. "Super Charged". IEEE Spectrum. Volume 42. Issue 1. 2005. pp. 32-37.

[18] L. Gao, R. A. Dougal, and S. Liu. "Power Enhancement of an Actively Controlled Battery/Ultracapacitor Hybrid." IEEE Transactions on Power Electronics. Vol. 20, no. 1, 2005.

[19] L. Zubieta and R. Bonert, "Characterization of double-layer capacitor (DLCs) for power electronics application," *IEEE Trans. Ind. Appl.*, vol. 36, no. 1, pp. 199–205, Jan./Feb. 2000.

[20] L. Shi, M. L. Crow, "Comparison of Ultracapacitor Electric Circuit Models," in *Proc. IEEE PES General Meeting*, Jul. 20-24., 2008, pp. 1-6.

[21] T. Wei, X. Qi, and Z. Qi, "An Improved Ultracapacitor Equivalent Circuit Model for the Design of Energy Storage Power Systems," in *Proc.6th ICEMS*, Oct. 8-11, 2007, pp. 69-73.

[22] S. Buller, E. Karden, D. Kok and R.W. De Doncker, "Modeling the Dynamic Behavior of Supercapacitors Using Impedance Spectroscopy," *IEEE Trans. on Industry Applications*, vol. 38, no. 6, pp. 1622-1626, Nov/Dec 2002.

[23] W. Yang, J. E. Carletta, T. T. Hartley, and R. J. Veillette, "An ultracapacitor model derived using time-dependent current profiles," in *Proc. 51st MWSCAS*, Aug. 10–13, 2008, pp. 726–729.

[24] A.Grama, L. Grama, D. Petreus, and C. Rusu, "Supercapacitor Modeling Using Experimental Measurements," in *Proc. ISSCS*, Jul. 9-10, 2009, pp. 1-4.

[25] F. Belhachemi, S. Rael, B.Davat, "A physical based model of power electric double-layer supercapacitors," Proceeding of the IEEE Industry Applications Conference, Vol. 5, pp. 3069-3076, October 2000.

[26] V. Srinivasan, J.W. Weidner, "Mathematical Modeling of Electrochemical Capacitors", *Journal Electrochem Society*, Vol. 146 (1999), p.1650.

[27] N. Bertrand, O. Briat, J.-M. Vinassa, J. Sabatier, and H. El Brouji, "Porous electrode theory for ultracapacitor modeling and experimental validation," in *Proc. IEEE VPPC*, Sep. 3–5, 2008, pp. 1–6.

[28] N. Bertrand, J. Sabatier, O. Briat, and J. M. Vinassa, "Embedded Fractional Nonlinear Supercapacitor Model and Its Parametric Estimation Method," *IEEE Trans. Ind. Electron.,* vol. 57, no. 12, pp. 3991-4000, Dec. 2010.

[29] J.-N. Marie-Francoise, H. Gualous and A. Berthon, "Supercapacitor thermal and electrical behavior modeling using ANN.", *IEE Proc. Electr. Power Appl.*, Vol. 153, No. 2, Mar. 2006. pp. 255-261.

[30] F. Baalbergen, P. Bauer, and J. Abraham, "Energy Storage and Power management for Typical 4Q-Load." IEEE Transactions on Industrial Electronics, vol. 56, no. 5, MAY 2009

[31] W. Li, G. Joós, and J. Bélanger, "Real-Time Simulation of a Wind Turbine Generator Coupled With Battery Supercapacitor Energy Storage System." IEEE Transactions on Industrial Electronics, vol. 57, no. 4, APRIL 2010

[32] M. Ortúzar, J. Moreno, and J. Dixon, "Ultracapacitor-Based Auxiliary Energy System for an Electric Vehicle: Implementation and Evaluation." IEEE Transactions on Industrial Electronics, Vol. 54, no. 4, AUGUST 2007.

[33] S. Lukic, J. Cao, R. Bansal, F. Rodriguez, and A. Emadi, "Energy Storage for Automotive Applications." Transactions on Industrial Electronics, vol. 55, no. 6, JUNE 2008.

[34] Z. Amjadi and S. Williamson, "Power-Electronics-Based Solutions for Plug-in Hybrid Electric Vehicle Energy Storage and Management Systems" IEEE Transactions on Industrial Electronics, vol. 57, no. 2, FEBRUARY 2010.

[35] J. Moreno, M. Ortúzar, and J. Dixon, "Energy-Management System for a Hybrid Electric Vehicle, Using Ultracapacitors and Neural Networks" IEEE Transactions on Industrial Electronics, vol. 53, no. 2, APRIL 2006.

[36] M. Ortúzar, R. Carmi, and J. Dixon, "Voltage-Source Active Power Filter Based on Multilevel Converter and Ultracapacitor DC Link" IEEE Transactions on Industrial Electronics, vol. 53, no. 2, APRIL 2006.

[37] A. F. Burke, E. J. Dowgiallo, and J. E.Hardin, "Application of ultra-capacitors in Electric vehicle Propulsion Systems." Proceedings of the 34th International Power Sources Symposium 1990, pp. 328-33.3

[38] D. Haifeng and C. Xueyu, "A Study on Lead Acid Battery and Ultra-capacitor Hybrid Energy Storage System for Hybrid City Bus," International Conference on Optoelectronics and Image Processing. 2010, pages 154-159.

[39] E. Ozatay, B. Zile, J. Anstrom, and S Brennan, "Power Distribution Control Coordinating Ultra-capacitors and Batteries for Electric Vehicles", Proceedings of the 2004 American Control Conference. Boston, Massachusetts 2004, pp. 4716-4721.

[40] L. Gao, R. A. Dougal, and S. Liu, "Power Enhancement of an Actively Controlled Battery/Ultracapacitor Hybrid," IEEE Transactions on Power Electronics, vol. 20, no. 1, January 2005.

[41] P. H. Smith,T. N. Tran, T. L. Jiang, and J. Chung, "Lithium-ion capacitors: Electrochemical performance and thermal behavior," Journal of power Sources, vol. 243, pp. 982–992, December 2013.

[42] A. Xu, S. Xie, and X. Liu, "Dynamic Voltage Equalization for Series-Connected Ultracapacitors in EV/HEV Applications," IEEE Transactions on Vehicular Technology, vol. 58, no. 8, October 2009.

[43] H. Zhou, T. Bhattacharya, D. Tran, T. Siew, and A. Khambadkone, "Composite Energy Storage System Involving Battery and Ultracapacitor with Dynamic Energy Management in Microgrid Applications," IEEE Transactions on Power Electronics. vol. 26, no. 3, March 2011.

[44] S. Cui, D. He, Z. Chen, and T. Habetler, "A Wide Input Voltage Range ZVS Isolated Bidirectional DC-DC Converter for Ultra-capacitor Application in Hybrid and Electric Vehicles," IEEE International Electric Vehicle Conference (IEVC), 2012

[45] H. Xiaoliang, J.M.A. Curti, H. Yoichi, " Energy Management Strategy with Optimized Power Interface for the Battery Supercapacitor Hybrid System of Electric Vehicles," 39th Annual Conference of the IEEE Industrial Electronics Society, IECON 2013.

[46] Y. Tao, Z. Li, "Study on Modeling and Application of Ultracapacitor," 2014 IEEE Workshop on Advanced Research and Technology in Industry Applications (WARTIA).

[47] "Micro Hybrid Technologies, Lead-Acid Batteries, Lithium Ion Batteries, and Ultracapacitors: Market Analysis and Forecasts." Navigant Executive Summary. 2013.

[48] G. Tina and G. Capizzi, "Improved Lead-Acid Battery Modeling for Photovoltaic Application by Recurrent Neural Networks" International Symposium on Power Electronics, Electrical Drives, Automation, and Motion, 2008.

[49] S. Li, and B. Ke, "Study of Battery Modeling Using Mathematical and Circuit Oriented Approaches." Power and Energy Society General Meeting, 2011.

[50] P. M. Gomadam, J. W. Weidner, R. A. Dougal, and R. E. White, "Mathematical modeling of lithium-ion and nickel battery systems," Journal of Power Sources, vol. 110, no. 2, pp. 267–24, Aug. 2002.

[51] O. Tremblay, L.A. Dessaint and A.I. Dekkiche, "A Generic Battery Model for the Dynamic Simulation of Hybrid Electric Vehicles," in Proceedings of 2007 IEEE Vehicle Power and Propulsion Conference, Sep. 9-12, 2007, Arlington, TX, pp. 284 – 289.

[52] C. M. Shepherd, "Design of Primary and Secondary Cells," Journal of The Electrochemical Society, vol. 112, 1965, pp. 657-664.

[53] A. Cherif and M. Jraidi and A. Dhouib, "A battery aging model used in standalone PV system," Journal of Power Sources, vol. 112 (2002) 49– 53.

[54] Ross, Michael M. D."A Simple but Comprehensive Lead-Acid Battery Model for Hybrid System Simulation". in Proceedings of PV Horizon: Workshop on Photovoltaic Hybrid Systems, Montreal, Qc, September 10, 2001.

[55] M. Chen and G.A. Rincon-Mora, "Accurate Electrical Battery Model Capable of Predicting Runtime and I–V Performance," IEEE Trans. Energy Conversion., vol. 21, no. 2, pp. 504-511, June 2006.

[56] Z. M. Salameh, M. A. Casacca, and W. A. Lynch, "A mathematical model for lead-acid batteries," IEEE Trans. Energy Conversion, vol. 7, no. 1, pp. 93–98, Mar. 1992.

[57] M. Valvo, F. E. Wicks, D. Robertson, and S. Rudin, "Development and application of an improved equivalent circuit model of a lead acid battery," in Proc. Energy Convers. Eng. Conf., vol. 2, Aug. 1996, pp. 1159–1163.

[58] M. Ceraolo, "New dynamical models of lead-acid batteries," IEEE Trans. on Power Systems, vol. 15, no. 4, pp. 1184–1190, Nov. 2000.

[59] S. Barsali and M. Ceraolo, "Dynamical models of lead-acid batteries: Implementation issues," IEEE Trans. Energy Conversion., vol. 17, no. 1, pp. 16–23, Mar. 2002.

[60] L. Benini, G. Castelli, A. Macci, E. Macci, M. Poncino, and R. Scarsi, "Discrete-time battery models for system-level low-power design," IEEE Trans. on VLSI Systems, vol. 9, no. 5, pp. 630–640, Oct. 2001.

[61] B. Schweighofer, K. M. Raab, and G. Brasseur, "Modeling of high power automotive batteries by the use of an automated test system," IEEE Trans. on Instrument Measurement, vol. 52, no. 4, pp. 1087–1091, Aug. 2003.

[62] L. Gao, S. Liu, and R. A. Dougal, "Dynamic lithium-ion battery model for system simulation," IEEE Trans. Compon. Packag. Technol., vol. 25, no. 3, pp. 495–505, Sep. 2002.

[63] S. Buller, M. Thele, R. W. D. Doncker, and E. Karden, "Impedance based simulation models of supercapacitors and Li-ion batteries for power electronic applications," IEEE Transactions on Industry Applications, Vol. 41, Issue 3, May-June 2005, pp. 742 – 747.

[64] P. Baudry, M. Neri, M. Gueguen, and G. Lonchampt, "Electro-thermal modeling of polymer lithium batteries for starting period and pulse power," J. Power Sources, vol. 54, no. 2, pp. 393–396, Apr. 1995.

[65] H. Zhang and Mo-Yuen Chow, "Comprehensive Dynamic Battery Modeling for PHEV Applications," in Proceedings of 2010 IEEE PES General Meeting, Minneapolis, MN, July 26-29, 2010.

[66] 'Design Considerations for Hybrid LiC/Battery Systems In Pulsed Power Applications'. JSR White Paper

APPENDIX. Ultracapacitor Simulink model

Equations describing the electrical model of the 1100-F ultracapacitor at room temperature are written below.

$$C_o = av_o^4 + bv_o^3 + cv_o^2 + dv_o + e \qquad\qquad (A.1)$$

where v_o is the open circuit voltage and the polynomial coefficients are

a = -1401.21545063799

b = 17406.8525977191

c = -79908.2275963045

d = 160796.712499727

e = -118704.377960371

$$i_1 = C_{sa}\frac{dv_{C_{sa}}}{dt} \qquad\qquad (A.2)$$

$$i_2 R_s = v_{sa} + C_{sa}\frac{dv_{C_{sa}}}{dt}R_{sa} \qquad\qquad (A.3)$$

$$i = i_{self\ discharge}$$

$$R_p = R_{self\ discharge}$$

$$i = i_1 + i_2 \ (4)$$

$$= i_o + i_p$$

$$= C_{sa}\frac{dv_{C_{sa}}}{dt} + \frac{v_{C_{sa}}}{R_i} + \frac{C_{sa}R_{sa}}{R_i}\frac{dv_{C_{sa}}}{dt} \qquad\qquad (A.5)$$

$$= C_{sa}\frac{dv_{C_{sa}}}{dt}\left[1 + \frac{R_{sa}}{R_i}\right] + \frac{v_{C_{sa}}}{R_i} \qquad\qquad (A.6)$$

$$= C_o \frac{dv_o}{dt} + \frac{v_o}{R_p} \tag{A.7}$$

$$\rightarrow \frac{dv_o}{dt} = \frac{i}{C_o} - \frac{v_o}{C_o R_p} \tag{A.8}$$

Also

$$(av_o^4 + bv_o^3 + cv_o^2 + dv_o + e)\frac{dv_o}{dt} = C_{sa}\frac{dv_{C_{sa}}}{dt}\left[1 + \frac{R_{sa}}{R_i}\right] + \frac{v_{C_{sa}}}{R_i} - \frac{v_o}{C_o R_p} \tag{A.9}$$

$$v_t = v_r + v_o \tag{A.10}$$

$$= v_{sa} + C_{sa}\frac{dv_{C_{sa}}}{dt}R_{sa} + \int(\frac{i}{C_o} - \frac{v_o}{C_o R_p})dt \tag{A.11}$$

$$= v_{sa} + C_{sa}\frac{dv_{C_{sa}}}{dt}R_{sa} + \int(\frac{i}{av_o^4 + bv_o^3 + cv_o^2 + dv_o + e} - \frac{v_o}{(av_o^4 + bv_o^3 + cv_o^2 + dv_o + e)R_p})dt \tag{A.12}$$

A Simulink model for the simulation of the 1100-F ultracapacitor is provided in figure
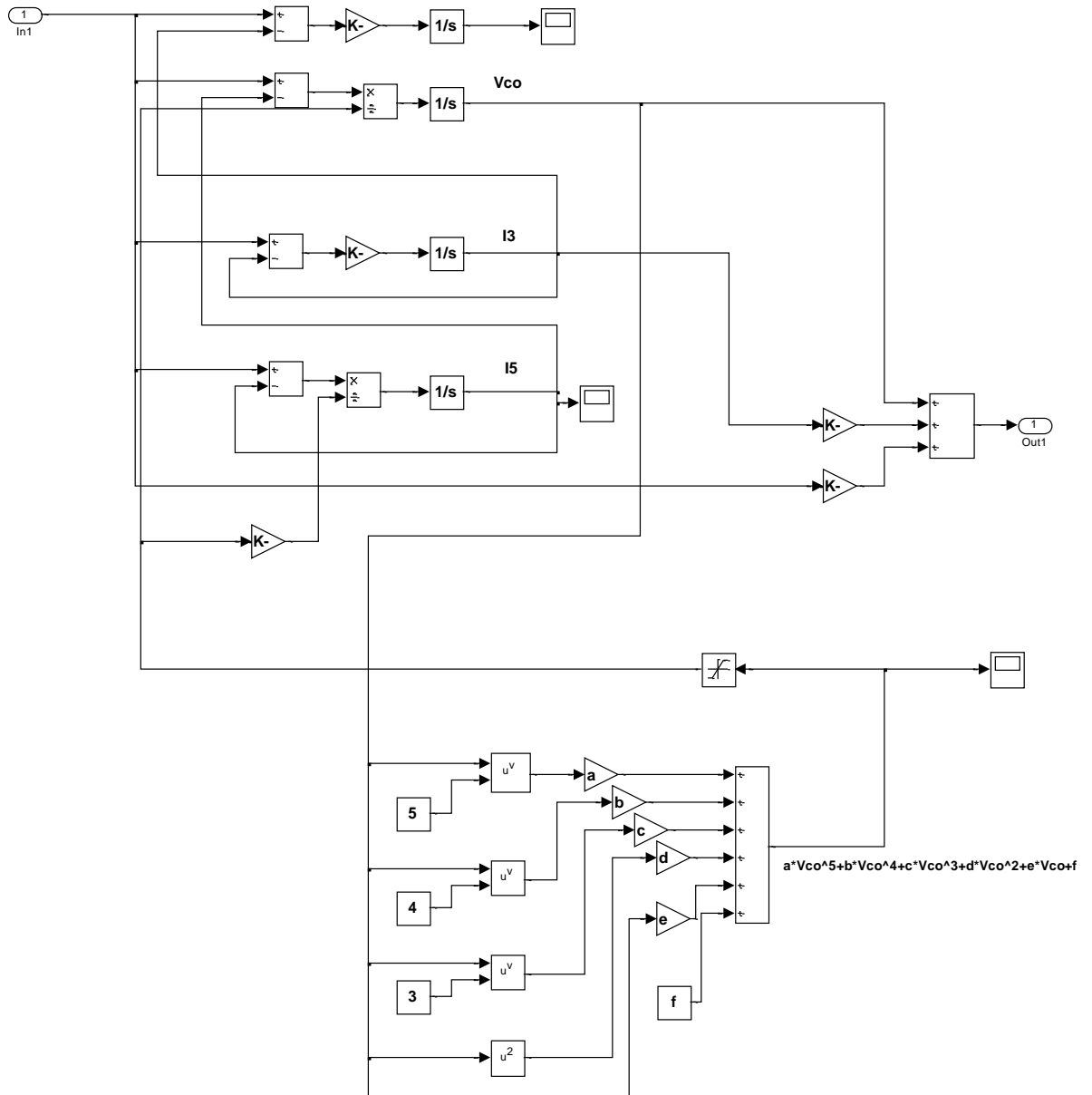
A.1

Figure A.1. Simulink model used to simulate the ultracapacitor

Curriculum Vita

Emad Manla
emanla@uwm.edu
Date of Birth: 01/01/1985

Education

2009 – 2015	**University of Wisconsin Milwaukee, Milwaukee, WI**

- Ph.D. in Electrical Engineering with a minor in Mathematics, August 2015.
- Undergraduate minor degree in French

2008 – 2009	**University of Wisconsin Milwaukee, Milwaukee, WI**

- MS in Electrical Engineering.

2007 – 2008	**Carleton University, Ottawa, Canada**

- Masters student in Systems and Computer Engineering

2002 – 2006	**American University of Sharjah, Sharjah, UAE**

- BS in Electrical Engineering.
- Minor in Applied Mathematics

University Teaching Experience

Department of Electrical Engineering, University of Wisconsin Milwaukee, Milwaukee, WI

Fall 2009 - Spring 2011	Lecturer of the Electromechanical Energy Conversion course (EE362)
Fall 2012- Spring 2013	Developed the class syllabus, wrote own lecture notes, prepared tests and supervised a number of Lab teaching assistants.
Fall 2008- Spring2009	Lab instructor for Electromechanical Energy Conversion (EE362)

Community Teaching Experience

American University of Sharjah, UAE

2004 – 2006   Tutor for a number of math courses such as Calculus I, Calculus II, Calculus III, Calculus for Business, Linear Algebra, and Differential equations.

University of Wisconsin Milwaukee, Milwaukee, WI

2010 – Present   Tutored College Algebra, Calculus I, Calculus II, Calculus III, Engineering Mathematics, Probability and Statistics, Electric Circuits I, Physics I, and Physics II. Worked mainly with international students from KSA having difficulty adapting to the Engineering curriculum at UW-Milwaukee.

Research Experience

University of Wisconsin Milwaukee, Milwaukee, WI

2009 – Present   Doctoral thesis research conducted with Professor Adel Nasiri. Developed test setup and conducted lab experiments on Li-ion ultracapacitors in order to devise an electric circuit equivalent model depicting its behavior when integrated into power systems. Built a test setup for batteries and ultracapacitors using NI CompactRIO hardware and LabView interface. Built a 360-V and a 720-V ultracapacitor module comprised of ultracapacitors connected in series and verified model on them. Research resulted in two publications, one in ECCE 2011, and another in the IEEE Journal of Emerging and selected topics in Power Electronics. Successful modeling of this ultracapacitor lead to the use of the model in a number of applications such as vehicular start-stop, which is the topic of my dissertation.

University of Wisconsin Milwaukee, Milwaukee, WI

2008 – 2009   Masters thesis research conducted with Professor Adel Nasiri involving modeling a Zinc-bromide Energy Storage System (ZESS). This 650-Ahr battery was tested using a series of charging/discharging tests in order for an equivalent circuit model to be developed. Research resulted in two Publications, a conference paper in IECON 2009, and a journal paper in the IEEE Transactions on Industrial Electronics, 2010.

American University of Sharjah, Sharjah, UAE

2006   Senior-year design project research under the supervision of Dr.
            Khaled Assaleh and Dr. Armin Eberlin. Project titled "Design of
            an integrated speed monitoring system" resulted in a conference
            paper publication in ISMA-07 2007

Work experience

June 2014-Present   **Intern at ABB, New Berlin, WI- June 2014-Present**

- Learned the functions of ASC 2000 MVD major components
- Finished ABB safety and integrity modules online
- Took the lead building Frame-4 MVD phase modules
- Modified and developed m-file code written in Matlab aimed at controlling and communicating with the ACS 2000 MVD
- Trained on troubleshooting problems with MVD
- Discussed power system design issues with senior engineers
- Monitored phase module static, pulse, and PWM tests
- Monitored crow bar electrical qualification tests
- Performed electrical component qualification tests on Electrikon capacitors and Trafotek and Scahffner inductor stacks
- Contributed to the reorganizing of the MVD R&D Lab
- Took the lead writing the gate drive tester instruction manual
- Repaired and continue to repair broken phase modules
- Helped repair the Grover MVD after EMC cap failure
- Performed electrostatic voltage threshold testing on gate drives
- Helped modify gate drive tester Board
- Attended various MVD group meetings

2008- Present   **Graduate assistant at the University of Wisconsin Milwaukee, Milwaukee, WI**

- Electromechanical Energy Conversion lab assistant (one year)
- Electromechanical Energy Conversion lecturer (three years)
- Research assistant (two years)

February 2007-   **Intern at Motorola Inc**.
July 2007

- Performed Drive Tests on GSM 2G networks.
- Studied the structure of GSM 2G networks
- Performed network parameter optimization
- Repaired broken hardware devices
- Learned AutoCAD and utilized it for micro-cell planning

June 2005-July 2005 **Intern at Emirates Iron and Steel Factory (EISF)**

- Studied the entire process of steel-bar production
- Completed a PLC control project
- Wrote technical reports to the maintenance Department

2004-2006 **Grader at AUS for the following courses**

- Calculus I, calculus III, and Calculus for Business
- Linear Algebra and Differential Equations
- Stochastic Processes
- Digital Communications

Awards and Activities

AUS Dean's list for

- Fall 2002 (Ranked seventh in the school of engineering)
- Spring 2003 (Ranked fourth in the school of engineering)
- Fall 2005
- Spring 2006
- Fall 2006 (Ranked first in the school of engineering)

Fall 2008- **UWM Chancellor's award for four years in a row**
Spring 2012

Spring 2004 **Resident student advisor**

- Provided advice to fresh students living in the dorms
- Wrote technical reports to the residential halls management about students' problems and complaints

Computer Skills

Completed projects using Matlab, Simulink, and LabView. Familiar with C++ and PSim. Learn new languages, operating systems, and general software quickly.

Languages

- English: proficient in reading, writing, speaking, and listening
- Arabic: proficient in reading, writing, speaking, and listening
- French: proficient in reading, writing, speaking, and listening

Hobbies and Interests

Foreign languages, chess, charcoal portrait drawing, swimming, bowling, table tennis, and body building

Publications

- E. Manla, A. Nasiri, C. Rentel, and M. Hughes, "Modeling of Zinc Energy Storage System for integration with Renewable Energy," *IEEE IECON, pp. 3987–3992, 2009*

- E. Manla, A. Nasiri, C. Rentel, and M. Hughes, "Modeling of Zinc Bromide Energy Storage for Vehicular Applications," *IEEE Trans. Ind. Electron., vol. 57, no. 2, pp. 624–632, 2010*

- E. Manla, G. Mandic, and A. Nasiri, "Testing and modeling of lithium-ion ultracapacitors," *IEEE ECCE, pp. 2957–2962, 2011.*

- E. Manla, G. Mandic, and A. Nasiri, "Development of an Electrical model for lithium-ion Ultracapacitors," *IEEE JESTPE, 2015*

- E. Manla, M. Sabbah, and A. Nasiri, "Hybrid Energy Storage System for Conventional Vehicle Start-Stop Application," IEEE ECCE, *2015*

- S. A. Hamidi, E. Manla, and A. Nasiri, "Li-Ion Batteries and Li-Ion Ultracapacitors: Characteristics, Modeling and their Grid Applications," *IEEE ECCE, 2015*

- E. Manla, K. Assaleh, A. Eberlein, M. Ameri, "Design of an Integrated Speed Monitoring System", *Proceedings of the fourth International Symposium on Mechatronics and its Applications (ISMA-07),*Sharjah, UAE, April 2007

References

Dr. Adel Nasiri – Professor in the department of Electrical Engineering at UWM and academic advisor

Dr. Dan Ionel – Visiting professor in the department of Electrical Engineering at UWM, chief engineer at Regal Beloit, IEEE fellow, and dissertation committee member

Dr. David Yu – Professor in the department of Electrical Engineering at UWM and dissertation committee member

Dr. Chiu Tai Law – Associated professor in the department of Electrical Engineering at UWM and dissertation committee member

Dr. Sam Helwany – Professor in the department of Civil and Environmental Engineering at UWM and dissertation committee member

Tim Obermann – Project manager for MVD at ABB, New Berlin, WI

Peter Stipan – MVD Manager at ABB, New Berlin, WI